The Design of the ZEUS Regional First-Level Trigger Box and Associated Trigger Studies

Timothy Lawrence Short

Department of Physics and Astronomy

University of Bristol

A thesis submitted for the degree of

Doctor of Philosophy

March 1992

Abstract

The design of electronics suitable for fast event selection in the first level of the ZEUS trigger has been studied using a Monte Carlo simulation technique. It was found that integrating tracking information from two detectors (the Central Tracking Detector and the Forward Tracking Detector) at this level was both possible and beneficial. It was shown that this method improved efficiency of acceptance of DIS events of interest while enhancing rejection of background.

The performance of this part of the trigger was investigated for other physics: heavy quark pair production and J/Ψ events produced via boson-gluon fusion.

A method of investigating the kinematic dependency of the Central Tracking Detector first level trigger in such a way as to reduce computer resources required to acceptable levels was devised and implemented.

“...οἰα καὶ ἡμιν Ζεὺς επι εργα τίθησι διαμπερες εξέτι πατ ρων.
οὐ γὰρ πνγμαχοι εἰμὲν αμύμονες οὐδὲ παλαισται ἀλλὰ
ποσι κραιπνως θεομεν...”

“ I want you to be able to tell your noble friends that Zeus has given us too a certain measure of success, which has held good from our forefathers’ time to the present day. Though our boxing and wrestling are not beyond criticism, we can run fast...”

Homer: The Odyssey, Book VIII.

Acknowledgements

I would like to acknowledge everyone in the Bristol Particle Physics Group: Adrian Cassidy, Dave Cussans, Tony Duell, Neil Dyce, Helen Fawcett, Robin Gilmore, Teresa Gornall, Tim Llewellyn, John Malos, Alex Martin, Jean-Pierre Melot, Carlos Morgado, Tony Sephton, Vince Smith, Bob Tapper, Simon Wilson and Kostas Xiloparkiotis.

At Oxford, Jonathan Butterworth, Doug Gingrich and especially Fergus Wilson have all helped at various times. I am indebted to Mark Lancaster for the diagram which appears on page 56 and to Alex Mass of the University of Bonn for the one on page 65. I would also like to thank Frank Chlebana of the University of Toronto.

In particular my supervisor Brian Foster and Greg Heath have played a great part in this work.

During this work, I have been funded by the Science and Engineering Research Council.

I declare that no part of this thesis has been previously presented to this or any other university as part of the requirements of a higher degree.

The design of the ZEUS trigger, of which this work forms a part, has been the responsibility of many ZEUS collaboration members. At Bristol, I have been responsible for maintaining the trigger simulation software and underlying physics generator packages. I have been solely responsible for using this code to produce the results presented here except for those in chapter eight, which were obtained in collaboration with other ZEUSUK members.

Timothy Lawrence Short

Contents

List of Figures

List of Tables

Chapter 1
Physics at HERA

1.1 The Standard Model

Physics contains four fundamental forces: gravity, electromagnetism, strong and weak forces. The current understanding of particle physics is embodied in the 'standard model', which combines three of these forces in the framework of 'gauge theories' [1]. Quantum Electrodynamics (QED) describes forces between charged particles in terms of photon exchange between them. This idea is extended to include the weak force ('electroweak unification'), mediated by heavy W^+, W^-, Z^0 bosons. Finally, in quantum chromodynamics (QCD), gluons mediate the attraction which binds quarks in hadrons.

The model is in excellent agreement with experimental results, but contains more than twenty arbitrary parameters which must be adjusted to fit the data. It is hoped that as progress is made, this number will be reduced. Additionally, further steps towards a 'grand unified theory' containing all known forces are hoped for.

At the moment, the standard model envisages three families of quarks and leptons. The quarks are arranged in doublets.

Bound states of two or three quarks form mesons or baryons respectively. For example, two up quarks and a down form a proton. Leptons are currently thought to

doublet 1	**doublet 2**	**doublet 3**	**charge**
up	charm	top	+2/3
down	strange	bottom	-1/3

Table 1.1: Quark doublets.

doublet 1	doublet 2	doublet 3	properties
e	μ	τ	large mass, charged
ν_e	ν_μ	ν_τ	no mass or charge

Table 1.2: Lepton doublets.

be elementary and are also arranged in doublets as shown in table 1.2. Here, heavy fermions are each accompanied by a neutrino.

1.1.1 QED

The Klein-Gordon (equation 1.1) and Dirac (equation 1.2) equations were devised as relativistic substitutes for the Schrödinger wave equation for fermions and bosons respectively

$$-\frac{\partial^2\phi}{\partial t^2} = \left(-\nabla^2 + m^2\right)\phi \tag{1.1}$$

$$\left(i\gamma^\mu\partial_\mu - m\right)\Psi = 0 \tag{1.2}$$

where ϕ and Ψ are the wavefunctions of their particles, m their mass, the γs are matrices constructed from Pauli spin matrices, and $\gamma^\mu\partial_\mu = \gamma^0\frac{\partial}{\partial t} + \gamma\cdot\nabla$. Quantum mechanics postulates that wavefunctions may have arbitrary phase since phases do not influence any observable quantities. The requirements that the behaviour of particles under the equations is invariant under phase transformations constitutes the powerful 'gauge principle'. In particular, there may be 'local' transformations: phase changes dependent on spacetime coordinates may be introduced. The gauge principle is equivalent to the demand that there should be invariance under the local transformation in equation 1.3.

$$\Psi(\mathbf{x},t) \rightarrow \Psi'(\mathbf{x},t) = \exp\left[\mathrm{i}\alpha(\mathbf{x},\mathrm{t})\right]\Psi(\mathbf{x},\mathrm{t}) \tag{1.3}$$

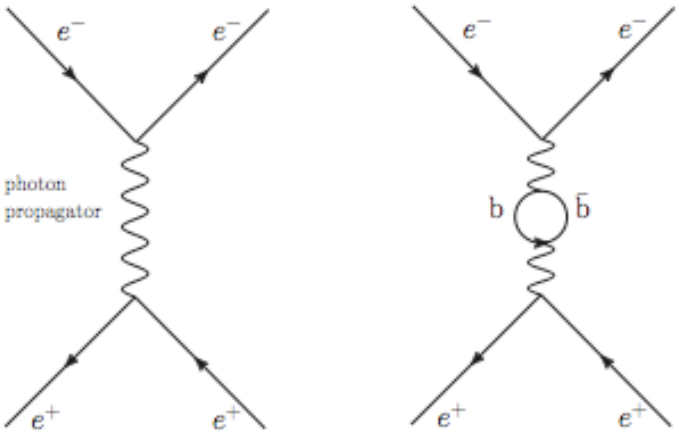

Figure 1.1: Feynman diagrams for electron-positron scattering in QED.

However, the differential operators in both of the relativistic field equations equation 1.1 and equation 1.2 will now operate on the phase factor α so the invariance is lost. It transpires that it is necessary to introduce vector potentials in which the particles described move in order to offset the changes and restore the invariance.

In QED, these potentials may then be expanded in a perturbation series whose expansion parameter at each order is α, the fine structure constant. This is small: $\alpha = \frac{e^2}{4\pi} = 1/137$. The expansion allows the computation of amplitudes at a given order of α for scattering processes via consideration of four-vectors for incoming and outgoing particles and matrix elements representing the transition probabilities between initial and final states.

The amplitudes were represented in diagrammatic form by Feynman. A scattering process such as $e^+e^- \rightarrow e^+e^-$ was thus viewed at lowest order as onvolving exchange of a virtual photon (figure 1.1(a)). Each part of a diagram for a given process is related to a corresponding term in the amplitude. There is a propagator term referring to the internal photon. Incoming and outgoing spinors are introduced for external

particle lines, and there are polarization vectors for any photons in the initial or final states.

Higher order correction terms in the expansion take the form of additional lines in the diagrams, For example, the diagram in figure 1.1(b) allows for the possibility of virtual pair creation in the propagator. These corrections proved problematical: the relevant series diverge leading to unphysical infinite cross-sections.

The solution to this difficulty was found in the idea of renormalization. The integrals corresponding to loop corrections diverge at high momentum. Renormalization involves choosing an energy scale Λ_{QED} above which no contribution to the amplitude will be considered. This is equivalent to truncating the perturbation series after a fixed number of terms. It emerges that the infinities now cancel at each order: their effects are subsumed into the properties of the particle in question. it is not possible ever to measure 'bare' charge and mass because of these vacuum polarization effects.

Renormalized QED has shown remarkable predictive power. For example, the magnetic moment μ of the electron is given by equation 1.4

$$\mu = \frac{ge}{4m_e} \tag{1.4}$$

where g is the 'gyromagnetic ratio'. The lowest order Dirac treatment predicts that $g = 2$ exactly, but in the broader picture an electron must be regarded as an entity surrounded by virtual pairs. As discussed above, these alter its apparent properties and mean that summing corrections to higher orders produces a different prediction for g. This prediction and the measurement agree to ten significant figures.

1.1.2 Weak Interactions

The weak interaction is responsible for β-decay. Fermi postulated a pointlike process involving a proton becoming a neutron together with the emission of a positron to

conserve charge and a neutrino to explain the observed energy spectrum. This picture has been modified (it is now based rather on quark transitions) but retains its validity.

In the framework of gauge theories, forces require a quantum to transmit their effects; intermediate vector bosons were postulated to fill this $r\hat{o}le$. These are now known to be charged W^{+} and W^{-} together with the neutral Z^{0}. These play an analogous part in the weak interaction to that of the photon in QED.

By the Heisenberg uncertainty principle, the range of a force is related to the inverse mass of its quanta. The masses ($\geq 80\ \mathrm{GeV/c^2}$) of the Ws and Zs show that the range of the weak force is relatively small. Further, the propagator term in the cross-section formula depends on $\mathrm{M}_{\mathrm{W,Z}}^{-2}$, so the strength of the weak interaction is also comparatively small for low energy processes.

Weak interactions violate parity conservation: no process has so far been observed which involves a right-handed ($i.e.$ positive helicity) neutrino. In the formalism, operators are formed from γ_5 which is a product of Dirac γ matrices. The 'V-A' term $(1-\gamma_5)$ projects out negative helicity states. Changing the sign of γ_5 is equivalent to introducing a 'V+A' component and would result in a projection of positive helicity states. This would then allow processes producing the unobserved right-handed neutrinos. Since these are not observed the framework describing charged current weak interactions is known as 'V-A' theory.

1.1.3 Electroweak unification

The unification of the electromagnetic and weak sectors is embodied in the theory of Glashow, Salam and Weinberg [2] [3] [4]. This required i) the devising of a mechanism to generate mass for the weak bosons and ii) the identification of an appropriate gauge group.

Mass generation involves substitutions of derivatives analogous to equation 1.5

$$\Box^2 \rightarrow \Box^2 + \mathrm{M}^2 \tag{1.5}$$

where

$$\Box^2 = \nabla^2 - \frac{\partial^2}{\partial t^2} \tag{1.6}$$

so the interacting Maxwell equation for a massless photon

$$\Box^2 A^\mu = j^\mu \tag{1.7}$$

becomes

$$(\Box^2 + \mathrm{M}^2)\mathrm{W}^\mu = 0 \tag{1.8}$$

which is the equation for a free massive vector field. Considering only spatial components, this means it is necessary for the 'screening current condition' to hold: $i.e.$ that the current has a component proportional to the vector field.

$$j = -\mathrm{M}^2\mathrm{A} \tag{1.9}$$

This can only occur if an additional field is introduced. The *Higgs field*[5] screens out the infinite range weak field which would result from having massless weak bosons.

It transpires that the correct gauge group here is SU(2) $\otimes$ U(1). SU(2) is the 'weak isospin' space in which there is a symmetry of the weak sector and U(1) represents the standard phase invariance of electromagnetism. The conserved quantity in the whole of this space is hypercharge y given by

$$Q = t_3 = y/2 \tag{1.10}$$

where Q is the electromagnetic charge and t_3 is the third component of the weak isospin quantum number.

There are two gauge fields in the resulting wave equation each of which have their own coupling strength. The linear combination of fields

$$g'\hat{W}^{3\mu} + g\hat{B}^{\mu} \tag{1.11}$$

corresponds to the SU(2) and the U(1) parts of the overall gauge group. This represents a massless photon and a large mass W boson. The W mass is given by

$$\mathrm{M_W} = \mathrm{gf}/2 \tag{1.12}$$

where f is the vacuum expectation value of the Higgs field. The Z mass is related to this in terms of an angle which is the main free parameter of the theory

$$\mathrm{M_Z} = \frac{\mathrm{M_W}}{\cos\theta_{\mathrm{W}}} \tag{1.13}$$

This angle also fixes the relative strengths of the unified parts via

$$g\sin\theta_W = e \tag{1.14}$$

The theory was vindicated with the discovery at CERN of the W and Z bosons with the correct masses. It has successfully predicted a large number of relevant cross-sections ($e.g.$ for ee,ep scattering) and the decay width for the Z.

1.1.4 QCD

Considering baryons to be made up of three quarks had been shown to be productive prior to the advent of QCD. However, the Pauli exclusion principle was to force an extension to the simple quark model. The principle requires the wavefunction of a fermion to be antisymmetric; that is, under exchange of a pair of fermions, the wavefunction must change sign. Particles made up of an odd number of fermions are themselves fermions and thus the combined wavefunction of a baryon must change sign under exchange of one of its quark components. However, the Δ^{++} resonance consists of three u quarks in identical spin states. It was therefore necessary to introduce an additional 'internal' degree of freedom to distinguish the quarks. This was termed 'colour'. It is important to remember that free colour has never been observed, so all particles must be formed from colour neutral superpositions.

QCD is the theoretical framework which describes the strong interactions between quarks in terms of this colour charge. This is mediated by gluons which are themselves coloured and so can feel the influence of other gluons. This results in the phenomenon of 'colour antiscreening'[?] in QCD. As the distance scale probed decreases, apparent electric charge increases in QED. However, gluons reduce the effective coupling at smaller distances. This is why the ideas of perturbation theory, developed for weak forces, are applicable to QCD which describes the strong force. The theory is described as 'asymptotically free', meaning that as the distance scale probed grows smaller, so does the coupling. Conversely, this has the important consequence that quarks cannot exist in the free state: as two quarks are separated the bond strength between them increases to the point where pair production of new quarks takes place.

1.2 Types of events at HERA

1.2.1 Introduction

HERA will collide $820\ \mathrm{GeV}$ protons with $30\ \mathrm{GeV}$ electrons. Physics of interest will lie in the extension of measurements to a much larger kinematic range than has

been previously available[7]. This section will outline the processes relevant to the work described later in this thesis. These fall into three main sections. Deep inelastic scattering events (DIS) are the mainstay of HERA physics. Secondly, many processes of interest take place via the mechanism of boson-gluon fusion (BGF). Finally more exotic processes are outlined.

The amount of data taken by an experiment is often quoted in units of inverse picobarns. A barn is $10^{-28}\ \mathrm{m}^2$. ZEUS is expected to accumulate $100\mathrm{pb}^{-1}$ for each year of operation. This figure of 'integrated luminosity' may be multiplied by the cross-section for a given process to deduce the number of such events to be expected in a sample.

For example, the cross-section for top-quark pair production via photon-gluon fusion (see section 1.2.3.1) is dependent on the mass of the top quark. This now means that is unlikely to be much larger than $0.01\mathrm{pb}$ and ZEUS is now thought to be unlikely to observe these events.

1.2.2 Deep Inelastic Scattering Events

1.2.2.1 Introduction

All elements of the standard model are necessary to understand DIS events. In the quark-parton model, these events are viewed as being due to the exchange of a boson between the incoming lepton and a quark. As mentioned previously, it is impossible to observe free quarks: at some separation the binding energy becomes sufficient to enable pair creation. By processes not at present fully understood, the scattered quark 'hadronizes' forming a 'current jet' of many energetic, strongly interacting particles. DIS events are classed as 'charged current' (CC) if the intermediate boson is a charged W, neutral current (NC) if it is a Z or γ. If the event is of NC type, the scattered electron may be observed in the detector; CC events contain a neutrino which will escape from the detector without interacting.

The topology of these events is generally described in terms of a particular formalism, described in the next section.

1.2.2.2 General Kinematics

Several variables are used to describe event kinematics. Q^2 is the squared four-momentum transfer between the quark and the outgoing lepton.

$$Q^2 = -q^2 = -(p_e - p_l)^2 \tag{1.15}$$

the Bjorken variable

$$x = \frac{Q^2}{2P \cdot q} = \frac{Q^2}{2m_p \nu} \tag{1.16}$$

and the variable

$$y = \frac{P \cdot q}{P \cdot p_e} = \frac{\nu}{\nu_{max}} \tag{1.17}$$

In these equations p_e, p_l and P are the four-momenta of the incoming and scattered lepton, and the incoming proton respectively, and $\nu = \frac{q \cdot p}{m_p}$ is the energy transferred by the current in the proton rest frame.

In the limit of small lepton masses the variables Q^2, x and y can be determined from the outgoing lepton energy E_l and the lepton scattering angle θ_l (measured with respect to the electron direction)

$$Q^2 = 4E_e E_l \sin^2 \frac{\theta_l}{2} \tag{1.18}$$

$$x = \frac{E_e E_l \sin^2 \frac{\theta_l}{2}}{E_p \left(E_e - E_l \cos^2 \frac{\theta_l}{2}\right)} \tag{1.19}$$

$$y = 1 - \frac{E_l}{E_e} \cos^2 \frac{\theta_l}{2} \tag{1.20}$$

In CC events the neutrino energy and scattering angle cannot be measured by the detector but Q^2, x and y can be calculated from the energy E_j and production angle θ_j of the current jet (measured with respect to the proton direction)

$$Q^2 = \frac{E_j^2 \sin^2 \theta_j}{1 - \frac{E_j}{E_e} \cos^2 \frac{\theta_j}{2}} \tag{1.21}$$

$$x = \frac{E_j \cos^2 \frac{\theta_j}{2}}{E_p \left(1 - \frac{E_j}{E_e} \sin^2 \frac{\theta_j}{2}\right)} \tag{1.22}$$

$$y = \frac{E_j}{E_e} \sin^2 \frac{\theta_j}{2} \tag{1.23}$$

Physically, x is the fraction of the proton momentum carried by the struck quark and can thus take values between 0 and 1. It is related to Q^2 by a well known relation which is shown in equation 1.24.

$$Q^2 = sxy \tag{1.24}$$

The interpretation of y at HERA is less straightforward. In fixed target experiments,

it is the fractional energy transfer in the laboratory frame and is given by dividing the energy of the exchanged boson by the incoming lepton energy. In a lepton-quark frame in which $\hat{s} = xs$ is the squared subprocess total energy, $y = \frac{Q^2}{\hat{s}}$.

The value of s at the HERA nominal beam energies is given by equation 1.25.

$$s = 4E_e E_p = 98400 \tag{1.25}$$

Clearly for Q^2 to take this maximum value is it required that $x = y = 1$ meaning that *all* of the proton momentum is carried by the struck quark; $y = 1$ corresponds to maximum Q^2 for the particular struck quark.

1.2.2.3 Jacquet-Blondel Kinematics

Jacquet-Blondel kinematics consists of a parameterization of the above variables. The standard equations[8] express Q^2 in terms of jet angle θ_{jet} and energy E_{jet} as follows:

$$Q^2 = \frac{E_{jet}^2 \sin^2 \theta_{jet}}{1 - y} \tag{1.26}$$

where

$$y = \frac{E_{jet}}{2E_e} (1 - \cos \theta_{jet}) \tag{1.27}$$

This formalism is applicable to all CC and NC processes. At low Q^2 the scattering is dominated by the pure electromagnetic term. As Q^2 increases, the γ/Z^0 interference term becomes important and finally above around $Q^2 = 10^4 (GeV/c)^2$ the pure weak term dominates.

DIS events are defined to be those which have high Q^2 and high ν in distinction

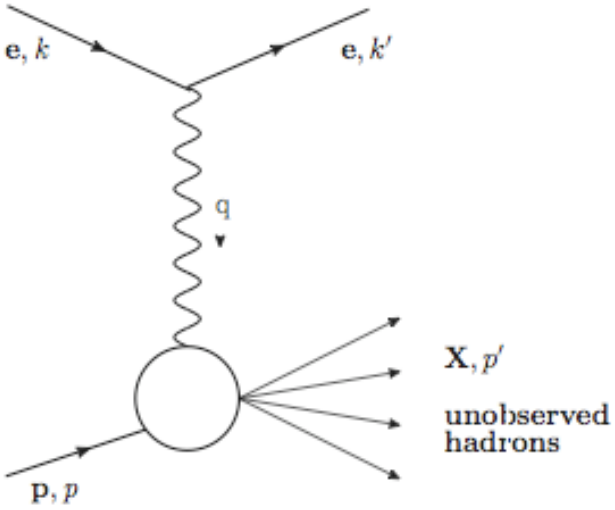

Figure 1.2: Feynman diagram for DIS.

from elastic[1] processes. The relevant Feynman diagram is shown in figure 1.2.

1.2.2.4 Structure Functions and Scaling

The kinematical dependency of the DIS cross-section factorizes into leptonic and hadronic parts, each represented by a tensor.

$$d\sigma \sim L_{\mu\nu} W^{\mu\nu}(q,p) \tag{1.28}$$

where q,p are four-vectors for the intermediate boson and the incoming hadron respectively. This leads to the following form for the NC cross-section

[1] If the scattering is elastic, then the four-momentum of the proton is unchanged by the collision: $p = p'$. By conservation at the vertex, $p+q = p'$ so $(p')^2 = p^2 + 2p\cdot q + q^2$ and $2p\cdot q = -q^2 = Q^2 = 2m_p\nu$ holds for elastic scattering.

$$\frac{d^2\sigma_{NC}(e^{\pm}p)}{dxdy} = \frac{4\pi\alpha^2}{sx^2y^2}\left[(1-y)F_2(x,Q^2) + xy^2F_1(x,Q^2) \pm \left(y - \frac{y^2}{2}\right)F_3(x,Q^2)\right] \tag{1.29}$$

in which three new parameters have been introduced. F_1, F_2 and F_3 are the *structure functions* of the proton.

Bjorken scaling postulates that in the DIS regime, the Q^2 dependence of the structure functions should disappear, leaving only the x variation. Intuitively, this is pictured as being related to the idea that at high Q^2 the virtual boson interacts at short distances inside the proton, essentially with only one parton. This may then be regarded as free on the short timescales involved and the scattering is elastic. Then $y = x$ and the structure functions depend only on one variable. QCD predicts a violation of this scaling behaviour due to the addition of gluon loops.

1.2.3 Boson-gluon Fusion

1.2.3.1 Heavy-Flavour Pair Production

The phrase heavy-flavour conventionally refers to events involving the three heaviest quarks, that is the charm, bottom and the so far unobserved top quark. Events are mediated by the exchange of photons or bosons which fuse with a gluon radiated by the proton. This gives the BGF mechanism its name. The lowest order QCD diagrams are shown in figure 1.3.

The CC process is important for top production. However the total cross-section for all processes has a strong dependence on the quark mass [8]

$$\sigma(eq \to Q\bar{Q}X) \propto M_Q^{-4} \tag{1.30}$$

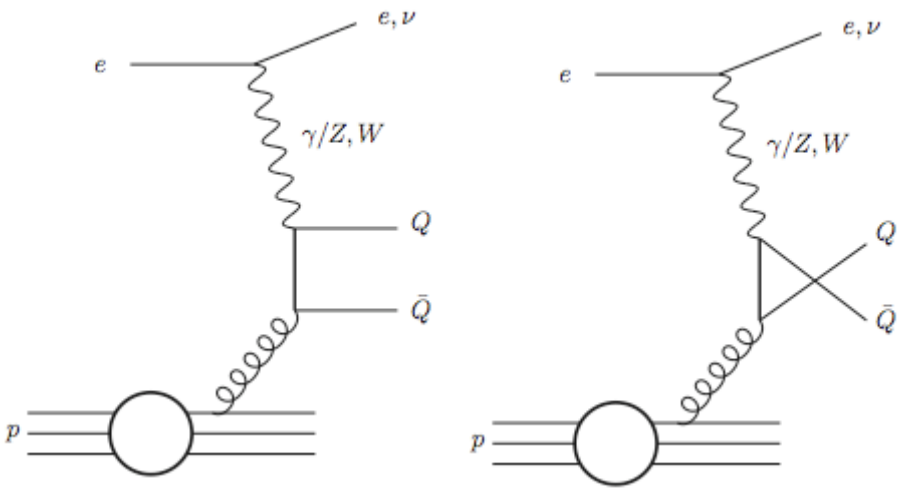

Figure 1.3: The two lowest order QCD diagrams for BGF. A quark/antiquark pair is formed.

At present, the top quark mass is thought to be $122^{+41}_{-32}\mathrm{GeV/c^2}$ so it is no longer expected that HERA experiments will be able to observe any top quark pair events. NC processes (in fact mostly gamma-gluon exchanges at low Q^2) dominate the BGF cross-section.

1.2.3.2 J/Ψ Production

J/Ψ particles may also be produced by the BGF mechanisms shown in figure 1.4. Perturbative QCD has been used extensively to make calculations concerning $c\bar{c}$ pair production as a whole. This is a useful approach because the strong coupling constant α_S becomes relatively small at the charmed quark mass scale. This can be seen from the leading logarithm approximation for α_S as a running coupling constant[1]

$$\alpha_S(Q^2) = \frac{12\pi}{21\ln(Q^2/\Lambda^2_{QCD})} \tag{1.31}$$

in which Λ is a QCD renormalization parameter.

[1]This form is valid only for 6 quark flavours

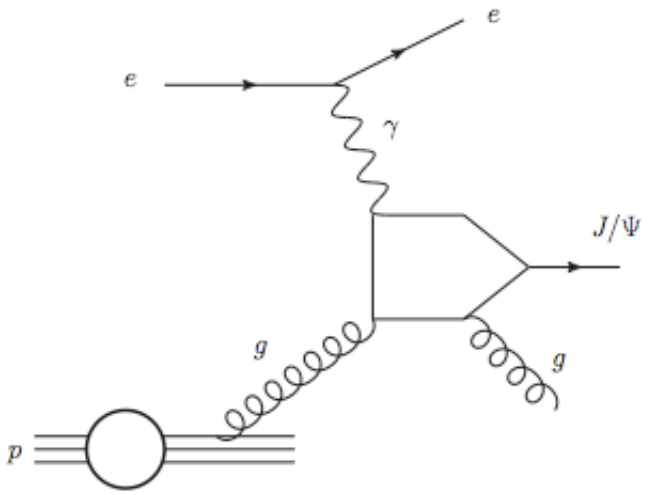

Figure 1.4: Lowest order diagram for inelastic J/Ψ production.

The running of the coupling constant arises, analogously with the QED case, from choosing a mass scale at which to cut off higher-order diagrams with many loops. The running of the coupling constant is a consequence of the colour antiscreening mentioned previously. Clearly Q^2 can be regarded as a measure of the penetration of the probe so it is expected that the coupling will decrease with higher Q^2.

Λ_{QCD} has been found to be between $0.1 \rightarrow 0.2\mathrm{GeV}$. The cross-section is dominated by almost real photons: $Q^{2_{photon}} = 0$ so the gluon must have $Q^2_{gluon} \simeq M^2_{\Psi}$. From equation 1.31 it can be seen that the coupling is relatively weak at the relevant mass scale.

Data so far available (e.g. EMC) supports the 'colour singlet' model of Berger and Jones [9] as the mechanism for J/Ψ production. The model successfully reproduces the transverse momentum and Q^2 dependence of the EMC data [10].

In order to extrapolate cross-sections down to the very low Q^2 domain of J/Ψ production, the Weizsaecker-Williams approximation [11] is important. it states that the cross-section for reactions with initial state photon bremsstrahlung may be factorized into two terms. One is the cross-section at the total energy after photon emission. The

other is dependent on the emitted photon and initial particle energies.

The J/Ψ cross-section is sharply peaked in x just above $x \simeq \frac{m_\Psi^2}{s}$ [12]. Because HERA is a high energy machine with large and variable s, the peaks occur at much lower values of x than at previous experiments so these events will be useful to probe the gluon distribution [13] in a new domain. They will have extremely low Q^2 ($10^{-4}\,\mathrm{GeV}^2 \leq \mathrm{Q}^2 \leq 10^{-2}\,\mathrm{GeV}^2$ for example) and hence a very small scattered electron angle.

1.2.4 Exotica

Three main avenues for investigation of exotic physics [14] exist at HERA. These are searched for excited electrons, leptoquarks/leptogluons and supersymmetry. The crucial parameter in this context at HERA is $\sqrt{s} = 314$GeV, which is the amount of energy available in the centre of mass frame for the creation of new states.

1.2.4.1 Excited Electrons

The existence of excitations would indicate that the presence of a previously undetected substructure. This would require another internal degree of freedom like colour: all observed states would be 'hypercolour' neutral. Hypergluon exchange would confine preons on some compositeness scale. The excited states decay (*e.g.* $l^* \rightarrow e + \gamma$ or $q^* \rightarrow q + W^\pm$) so construction of invariant mass plots from the decay products should prove a useful method of investigation.

1.2.4.2 Leptoquarks and Leptogluons

These are resonant states between leptons and partons [15]. Leptoquark production occurs at fixed x ($x = m_{leptoquark}/s$). The events are similar to DIS, which forms the major background. The DIS cross-sections show a Q^{-4} dependency whereas leptoquark decays are isotropic: they will show no Q^2 dependence. Thus selecting events with $Q^2 \geq 1000$ will produce a clean signature with good event rates if leptoquarks exist. HERA will be able to observe leptoquarks up to $\sqrt{s}$, the kinematic limit.

1.2.4.3 Supersymmetry

Supersymmetry, or SUSY, envisages a more broad symmetry than the usual multiplet schemes. Here, fermions and bosons may be members of the same gauge group multiplet. A usual, however, the supersymmetry must be broken in a manner consistent with low-energy phenomenology.

The minimal model gives each particle a SUSY partner so that there are now eight gluinos as well as the familiar gluons and also there are squarks and sleptons. Processes analogous to standard DIS are envisaged in which the gauge boson is replaced by a gaugino (*e.g.* a Zino or a Wino). This leads to a squark and a selectron in the final state.

The cross-sections for production at HERA should be sufficient to observe SUSY-NC processes providing that

$$m_{\tilde{e}} + m_{\tilde{q}} \leq 200 \text{ GeV/c}^2 \tag{1.32}$$

Chapter 2
Non-Tracking Elements of the ZEUS Detector

2.1 Introduction

The ZEUS detector consists of three main types of detector: those which are sensitive to charged tracks, those that measure energy deposition and those which identify muons. The UK's major responsibility on ZEUS is the Central tracking Detector (CTD). Because of this and the fact that a large part of the work outlined in this thesis has been connected with tracking components, their description deserves a separate chapter, which follows.

The tracking detectors reside in the inner region close to the interaction point. The remaining major components fall into two functional classes: calorimetry and muon detection.

The most significant characteristic common to all groups of components results from the substantial asymmetry in the beam energies at HERA. The forward direction is defined to be the one in which the proton moves. Clearly it is therefore to be expected that the forward hemisphere will be the more active. For this reason components here are more sophisticated than their near region counterparts. An overview of the detector is shown in figure 2.1.

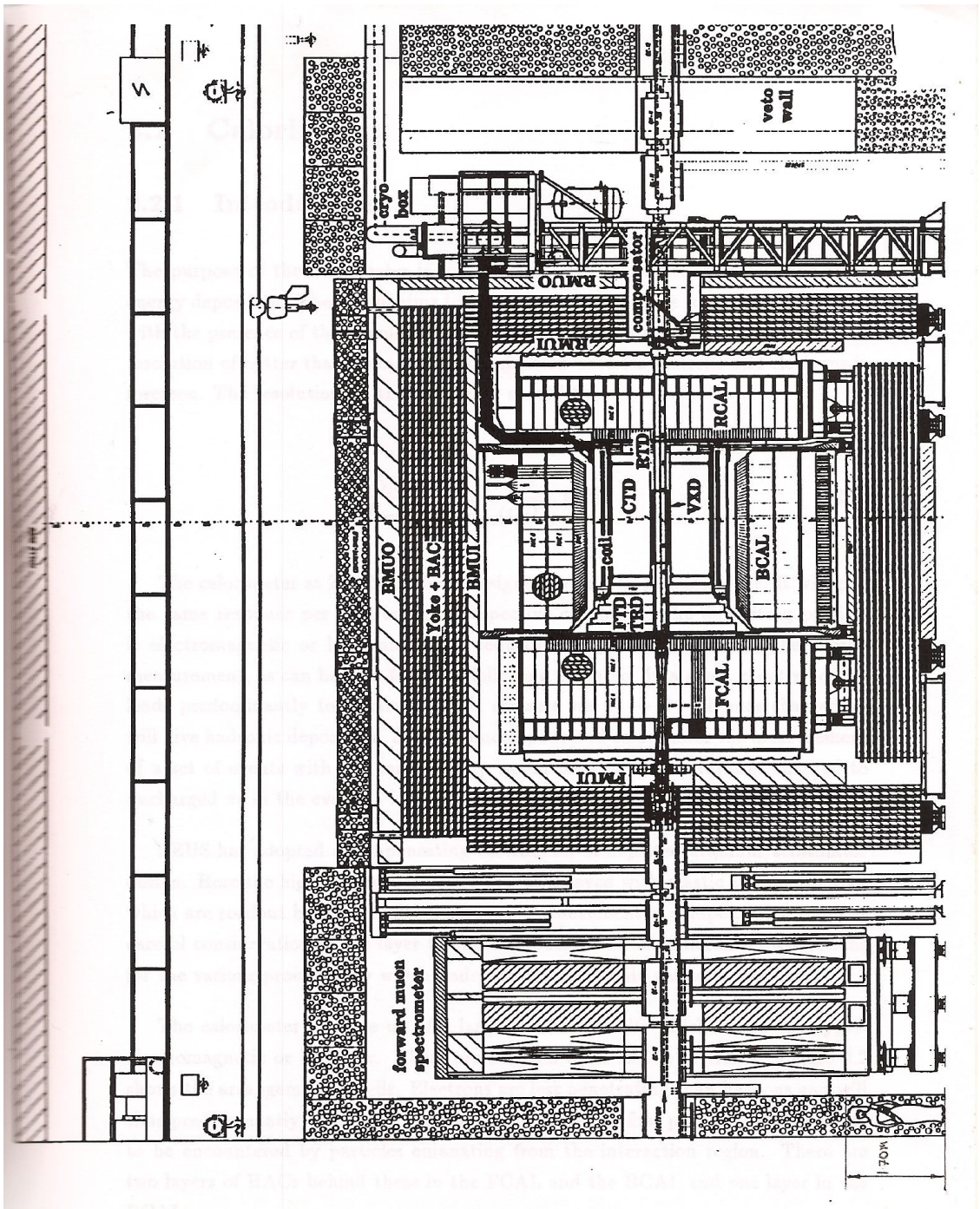

Figure 2.1: Section through the ZEUS detector along the beamline.

2.2 Calorimetry

2.2.1 Introduction

The purpose of the calorimeter is to investigate jet properties by measuring their energy deposition. The design aims to cover the full solid angle so far as is consistent with the presence of the beamhole. It allows for the discrimination of jet angles with resolution of better than 10 mrad. Discrimination between hadrons and electrons is foreseen. The resolution on the jet energy should be

$$\frac{\sigma(E_{jet})}{E_{jet}} = \frac{35\%}{\sqrt{E_{jet}\,(\mathrm{GeV})}} \oplus 2\% \tag{2.1}$$

The calorimeter at ZEUS has been designed to be 'compensating' *i.e.* it will give the same response per unit energy irrespective of whether the depositing particle is electromagnetic or hadronic. This reduces the systematic error in the energy measurement, as can be seen from the following example. In a given event π^0 day leads predominantly to electromagnetic showers vis $\pi^0 \rightarrow 2\gamma$ whereas charged πs will give a hadronic deposition. So in an uncompensated calorimeter the measurement of a set of events with the same energy would depend on the ratio of charged to uncharged πs in the events.

ZEUS has adopted a compensating calorimeter of depleted uranium/scinitillator design. Here the high-Z absorber plates are interleaved with plastic scintillator tiles which are read out by photomultiplier tubes. Achievement of compensation requires careful consideration of the layer thicknesses because of the different cross-sections for the various processes via which hadronic and electromagnetic particles lose energy.

The calorimeter is made up of a large number of cells which are of two types: electromagnetic or hadronic. These are referred to as EMCs or HACs. figure 2.2 shows the arrangement of cells. Electrons are less penetrating than hadrons and will thus predominantly interact in the EMCs which are the first part of the calorimeter to be

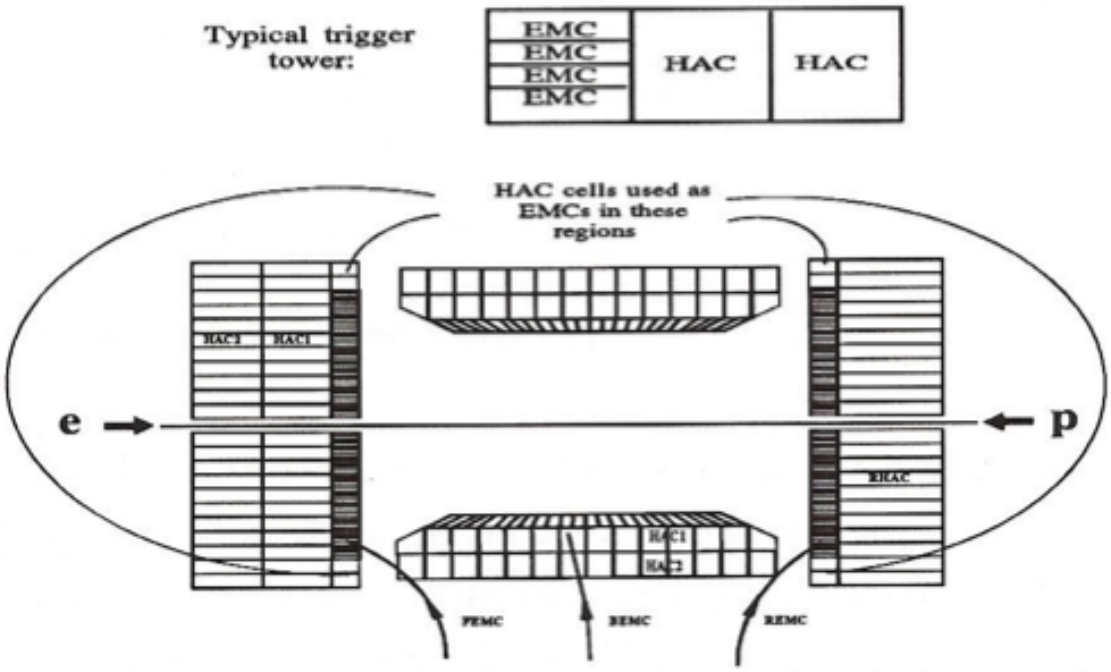

Figure 2.2: Arrangement of cells in the calorimeter.

encountered by particles emanating from the interaction region. There are two layers of HACs behind these in the FCAL and the BCAL and one layer in the RCAL.

2.2.2 Forward, Rear, Barrel Calorimeter (F/R/BCAL)

The calorimeter has three major sections. Their coverage in terms of polar angle and depth is shown in table 2.1. Depth is measured in radiation lengths , X_0, over which distance the energy of an electron will be reduced by a factor of e. it can be seen that there is some angular overlap between sections.

Each section has one interaction length of EMC at its face closest to the interaction point. Behind that, the layer of HACs varies from $\simeq 6\lambda$ in the forward direction to $\simeq 3\lambda$ in the rear. For readout purposes, cells are grouped into 'towers'. In the FCAL and RCAL these are non-projectives as are the BHAC towers. Tower sizes are shown in table 2.2.

Region	Coverage	X_0(EMC)	X_0(HAC)	λ(total)
FCAL	$2.2° \rightarrow 39.9°$	26	162	$5.6 \rightarrow 7.1$
BCAL	$36.7° \rightarrow 129.1°$	25	103	5.3
RCAL	$128.1° \rightarrow 176.5°$	26	81	$3.3 \rightarrow 4.0$

Table 2.1: Polar angle coverage of calorimeter sections.

Tower location	Dimension
FEMC	$5 \times 20cm^2$
REMC	$10 \times 20cm^2$
BEMC	$5 \times 24cm^2$
HAC	$20 \times 20cm^2$

Table 2.2: Calorimeter readout tower size.

2.2.3 Backing Calorimeter (BAC)

The BAC, together with the iron return yoke, is between the inner and outer muon chambers. It is designed to be complementary to the main calorimeter and the muon chambers. It will allow measurement of late-showering particles and it will provide a muon trigger in the bottom yoke where there will be no muon chambers.

There will be around 9 layers of BAC modules depending on the exact location. The layers are made up of either 7 or 8 tubes which each contain one gold/tungsten wire and use an argon/ CO_2 gas mixture. Four modules will be grouped on readout into towers of around $50\mathrm{cm} \times 50\mathrm{cm}$ base and summed in depth. The final position resolution should be 1.3mm and the design energy resolution for hadrons is $\frac{\sigma(E)}{E} \simeq 100\%/\sqrt{E}$.

2.2.4 Hadron Electron Separator

Silicon pad detectors will be mounted on ceramic cards which lie a few radiation lengths inside the EMC parts of the calorimeter. The separator is based on diodes with a small $(3\,\mathrm{cm} \times 3\,\mathrm{cm})$ active area. This improves segmentation and thus position

resolution.

The diodes are operated in depleted mode. The passage of a charged particle creates many charge carriers. The resulting pulse is readout and is of different heights for electrons and hadrons even if they are of the same energy. The ability of the calorimeter as a whole to distinguish electrons is therefore improved. Using only HES data, electron identification efficiency of 90% should be obtainable with only 4% hadronic contamination.

2.3 Muon Detectors

2.3.1 The Forward Muon Detector (FMUON)

This component is based on a toroidal magnet. Its detectors comprise streamer tubes and drift chambers, both of which measure ionization, and a time-of-flight (TOF) plane between the two toroids. It comprises in addition to two 'wall' sections (LW1,2) a 'spectrometer' section with five detector planes. These five planes are labelled LT1 $\rightarrow$ LT5. Particles from the interaction region encounter the wall sections first and then the spectrometer. The walls provide overlap of angular coverage with the BMUON. The planar sections are divided into eight sectors in ϕ. The TOF plane consists of sixteen elements, each are made up of a pair of scintillation counters separated by 10cm.

This component will provide small angle muon momentum resolution of 20%. This information is essential to complement tracking detector data. The purpose of the TOF plane is to ensure that particles are not associated with an incorrect beam crossing.

2.3.2 Barrel/Rear Muon Detectors (B/RMUO)

There are two sets of eight chambers in the barrel section, which thus has an octagonal cross-section looking down the beamline in which the inner and outer octagons are separated by the magnetized iron yoke and and the backing calorimeter. The RMUO has two parts, inner and outer, each of which has a depth of one chamber. A chamber consists of two doublets of streamer tubes which are parallel to the beamline in the

barrel and are placed horizontally in the RMUO. These are readout by time-to-digital converters. Analogue readout of strips in the orthogonal dimension is available in both cases.

2.4 Other Elements

2.4.1 The Vetowall (VETO

This is a large iron wall seven metres in front of the interaction region which has a hole in it through which the proton beam passes, It has hodoscopes on each side consisting of forty-eight individual scintillation counters.

There is a 'halo' of protons not following the nominal beam trajectory and these may produce highly penetrative muons by collision with machine elements. The main purpose of the vetowall is to veto these events and thus reduce the rate of spurious triggers in the detector.

2.4.2 The Luminosity Monitor

The measurement of cross-sections is of primary importance at ZEUS. This requires monitoring to arrive at the figure for time integrated luminosity. It is essential also to have the information online so as to be able to optimize the luminosity in the interaction region.

In order to do this, the LUMI uses the process of photon emission from the interaction of the two beams ep $\rightarrow$ epγ. Also, the LUMI will identify photoproduction processes by tagging small-angle electrons.

The detector itself has two parts, an electron detector near the electron beam at z=-36m and a photon (γ) detector around the proton beam at z=-108m. The electron detector is a shielded lead/scintillator sandwich. The γ-detector is based on a γ-calorimeter which consists of layers of $1\ \mathrm{cm}^2$ silicon pads. A photon causes a shower of electrons through them permitting precise position measurement. A Čerenkov

counter to veto electrons is included in the design; a prototype has been built using a 150cm thickness of polyurethane foam.

2.4.3 Leading Proton Spectrometer (LPS)

It is expected[16] that in 25% of DIS events, the proton will interact diffractively, retaining its identity and losing momentum. If this happens, it may then leave the beampipe and be measured by the LPS with efficiency $\simeq 0.6$ at the most favourable momentum.

The LPS will have six detector stations along the proton line between z$=+24$m and z$=+90$m as shown in figure 2.3. These will be based on turret extensions into which 'pots' can be inserted. pots contain detector elements: their purpose is to allow for precise control of location of the detectors over the last few centimetres close to the beampipe.

The first three stations will have a single pot and the last three will be double pot assemblies. The single pots will be horizontal with respect to the beamline and the double pots will be vertical. The exact location of the detectors is important because it determines the proton phase space acceptance of the LPS.

Each pot will contain a detector element comprising seven planes of silicon microstrips with differing orientations to provide two-dimensional measurement and will be shaped to fir closely to the beampipe. The total area covered by the strips will be $1560\ \mathrm{cm}^2$

2.4.4 Rucksack

The immediate environment of the detector is hostile to electronics owing to radiation from the uranium in the calorimeter and to proximity to the beam. Also, space is at a premium. Large systems of electronics are required however in order to read out the detector components and implement triggers. These factors have resulted in the inclusion in the design of a 'rucksack' which is simply a mobile construction of three floors each of which contains racks and space for the associated requirements in terms of cooling and safety.

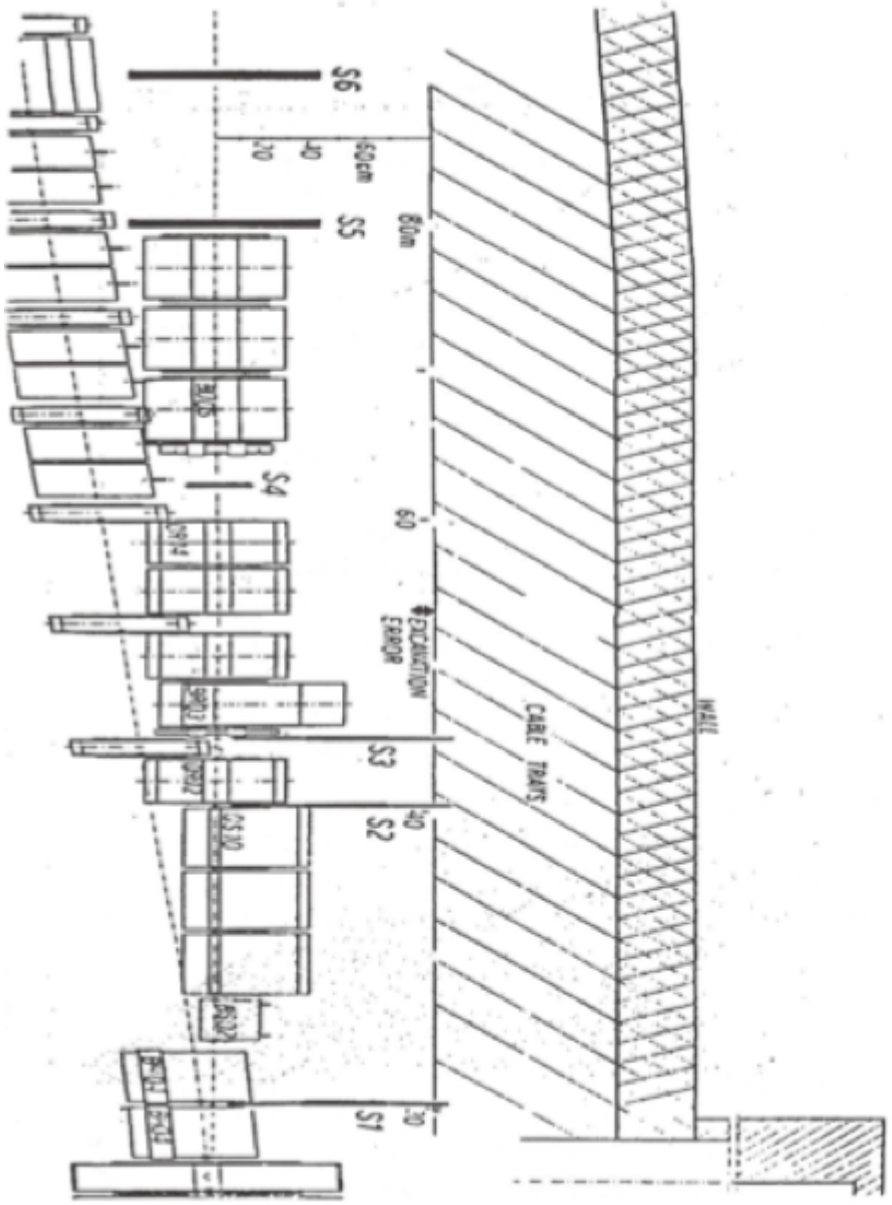

Figure 2.3: The LPS stations along the straight section of the beamline.

The rucksack is connected to the components via a dragchain which is designed to carry cables for readout. The rucksack must be mobile. This is because the yoke - the large iron clamshells and the BMUO/BAC - retracts to allow access to the inner detectors. The rucksack moves in the same rails in which the yoke runs.

2.4.5 Solenoid

A magnetic field must be supplied in the region of the tracking detectors so that charged tracks will bend in it and thus their momentum may be measured. A $1.9\,\mathrm{m}$ diameter superconducting solenoid is located between the calorimeter and the CTD in order to supply this. It is required to supply a field of $1.8\,\mathrm{T}$ within two major design constraints. Firstly, the electron beam trajectory is very sensitive to variation in the B-field and so non-uniformities must be as small as possible. For example, the axis of the field must be centred to within $\pm 1\,\mathrm{mm}$. Secondly, the structure of the solenoid must not present a large amount of material to the passage of electrons and photons as this would introduce an unacceptable systematic error in calorimeter measurements. Therefore the design goal states that at an angle of 90° the solenoid should have a thickness of less than 0.9 radiation lengths.

Chapter 3
Tracking Elements of the ZEUS Detector

3.1 Introduction

Both of the experiments planned for HERA, ZEUS and H1, have specialized tracking detectors in the forward direction because of the beam asymmetry mentioned previously. At ZEUS, there are four separate tracking chambers. The system as a while can take measurements of varying degrees of accuracy for tracks with polar angles between 7.5° and 170°.

All of the tracking detectors are wire drift chambers in which the passage of a charged particle leaves a trail of ionization. Anode wires in each chamber are equipped with electronics to readout pulses due to the arrival of charge produced by this ionization.

All of the chambers are designed to operate in a high magnetic field. This causes particle trajectories to bend thus enabling momentum measurement. The tracking detectors differ in their geometry and in gas mixture, field shape and strength depending on their location. In particular, the magnetic field is highly non-uniform in some regions and this has had to be taken into account.

Of the four detectors, the CTD and the Vertex Detector (VXD) are cylindrical while the Forward Detector (FDET) and Rear Tracking Detector (RTD) are planar. VXD is smaller than the CTD and occupies the space between it and the beampipe. The FDET is a composite of two detectors, the Forward Tracking Detector (FTD) and the Transition Radiation Tracker (TRD).

3.2 The Central Tracking Detector (CTD)

3.2.1 Introduction

The CTD has an overall length of $240\ \mathrm{cm}$ with inner radius of $16.2\ \mathrm{cm}$ and outer radius of $85\ \mathrm{cm}$. However some space must be left inside the chamber to house readout electronics, and allow for cabling and cooling requirements. The sense wires are strung along the $205\ \mathrm{cm}$ active length of the chamber between two $20\ \mathrm{mm}$ thick aluminum endplates.

The requirements which the CTD was designed to satisfy are:

- Event triggering by vertex measurement ($i.e.$ rejection of upstream gas), see section 5.2.
- High resolution momentum measurement of tracks.
- Identification of electrons by measurement of energy loss.

3.2.2 Mechanical Construction

The CTD[17] is radially subdivided into superlayers (SLs) which are numbered from one at the smallest radius to nine at the largest. Each SL thus forms an annular cylinder eight wires thick. There are two types of SL. In the axial SLs, the sense wires run parallel to the z-axis (see figure 3.1). In the stereo layers however a twist of five degrees has been introduced corresponding to a two-sell displacement at the endplates, in order to allow reconstruction of the z-coordinate of the tracks.

Within a SL, groups of eight sense wires are termed cells. The line of eight wires is at an angle of $45°$ to a radial lien from the centre of the chamber. This angle matches the Lorentz angle so as to maximize use of drift space. This geometry is shown in figure 3.2. There are 32 cells in SL1 with more in the outer SLs so that the cell size is roughly constant.

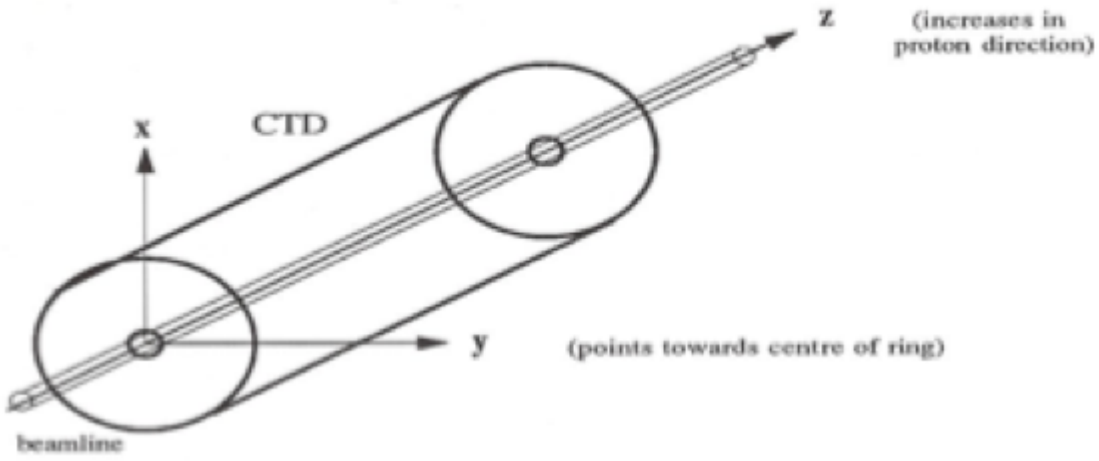

Figure 3.1: Central Tracking Detector Coordinate Systems.

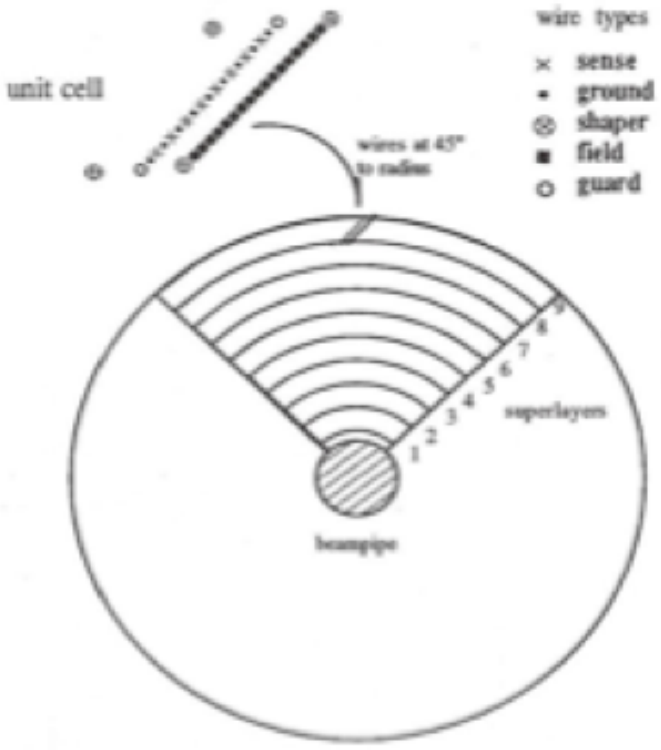

Figure 3.2: Central Tracking Detector Coordinate Systems.

Cells consist of the eight sense wires plus a variety of other wires which are all designed to supply and shape the electric field within a cell such that electron drift trajectories are uniform. The maximum drift distance is $25.6\,\mathrm{mm}$.

The uniform electrical field within each cell means that the drift velocity is independent of trajectory within the cell, simplifying reconstruction. It would be helpful if the drift velocity could be fixed such that the maximum drift time was small compared ti the beam-crossing interval. This would minimize difficulties in identifying which crossing a particular track is associated with. this would indicate a small cell size, but this would then require a larger number of wires to be readout. SO the cell size has been fixed at $\simeq 2.5\,\mathrm{cm}$ which maintains a small probability that two events will overlap in the same cell, satisfies the requirement that a not unreasonably large number of wires must be readout, and produces a maximum drift time of $500\,\mathrm{ns}$.

3.2.3 Electronic Readout

There are a total of 4608 sense wires in the CTD. It is necessary to terminate the wires in the 390Ω characteristic impedance of the chamber in order to prevent pulses being reflected back into it. At the FTD end, this is done by a resistor network (for those wires not equipped with z-by-timing readout). At the RTD end, it is done by preamp. cards [18] which are designed to increase the signal strength.

The preamps are connected to $42\,\mathrm{m}$ long high quality coaxial cables which run through the dragchain. This connects the chamber to the rucksack (section 2.4.4) which houses the majority of the electronics. Postamp boards amplify the signals. At this point the readout chain splits into two with both parts simultaneously being fed data. Both parts are concerned with coordinate identification in different planes.

3.2.3.1 R-ϕ Coordinates

The pulses from the postamps are sampled by 8 bit 104 MHz flash analogue-to-digital converters (FADCs). The results are continuously written to 512 location deep pipelines. Onboard Digital Signal Processors (DSPs) [19][1] produce drift times and do

[1] DSPs are microcomputers providing several MIPS of computing power and suited to high data throughputs.

pulse height/area analysis.

The radius of a hit is defined by the wire number, The ϕ coordinate may then be found from this and the drift time. There is, however, a left-right ambiguity. The drift time may be used to find the distance from the sense wire plane of the ionization causing it but not on which side of the wire it was produced. This has the effect that two sets of hits are found in each cell. Because of the $45°$ angle of the sense wire planes, one of these sets does not point to the interaction region and can be easily discarded. The design resolution is $100\mu\,\mathrm{m}$.

3.2.3.2 Z-coordinate

There are two methods of measuring the remaining z-coordinate, with differing degrees of precision. All of the sense wires in SL1 and half of those in SL3 and SL5 are instrumented for z-by-timing[20]. Those wires which are instrumented have preamps at both ends of the chamber and corresponding postamps in the rucksack.

On a given wire, pulses arrive at different times at the two ends of the chamber depending on where along the wire the ionization was produced. Preamplifiers mounted on the chamber drive the signal along coaxial cable to the rucksack where postamplifiers feed into constant fraction discriminator units. One end of the chamber has an extra $10\,\mathrm{ns}$ delay so that the pulses will always arrive in the same order. This enables time-to-amplitude conversion to take place based on charging a capacitor starting from the arrival of the start pulse and ending with the arrival of the stop pulse. The time difference is then proportional to the charge on the capacitor which is sampled by a FADC which has seven bits available to measure the z-coordinate. The design resolution is $3\,\mathrm{cm}$[21]. The FADC data is sent to the pipeline (section 4.3.1), which is read out in the event of a trigger.

Secondly, the wires in the stereo layers enable a three-dimensional track fitting. The drift times for hits in the axial layers for a given track are clearly independent of its location in z. However, moving in the z-direction, the cells in the corresponding stereo layers appear to rotate. Correlating the shift in $r\phi$ coordinates allows a measurement

of the z-coordinate. At present it is likely that this data will only be used in the full event reconstruction, where it should provide a resolution in z of $1.2\,\mathrm{mm}$.

3.3 Forward Detector (FDET)

The FDET consists of three FTD subchambers with two TRD modules in the gaps between them.

3.3.1 The Forward Tracking Detector (FTD)

A drawing of a subchamber is shown in figure 3.3. The FTD is intended to complement the angular coverage of the CTD and is crucial in providing data relating to tracks close to the beampipe.

Each of the FTD subchambers contains three readout planes, each containing more than a thousand wires. The sense wires are parallel to each other within a plane but there is a 60° offset between the planes to permit three dimensional hit location. The Siegen group is designing $100\,\mathrm{MHz}$ FADC cards similar to those that have been produced for the CTD which will be used to readout the FTD. However, the design here will be simpler.

3.3.2 The Transition Radiation Detector (TRD)

Charged particles crossing an interface between materials having different dielectric properties will lose energy by emission of photons. These photons will in turn transfer energies to atomic electrons via excitation and ionization processes. In this way, if the original particle was sufficiently energetic, an electromagnetic shower may be built up.

The TRD relies on this phenomenon. it has two parts. Firstly there is a radiator stack which consists of a nitrogen filled polypropylene fibre mass. Photons are produced here. A second stage is a drift chamber. The photons leave the radiator stack and enter a drift/amplification region. This part of the chamber is filled with xenon and the photons will excite atomic electrons which will cause an avalanche by further

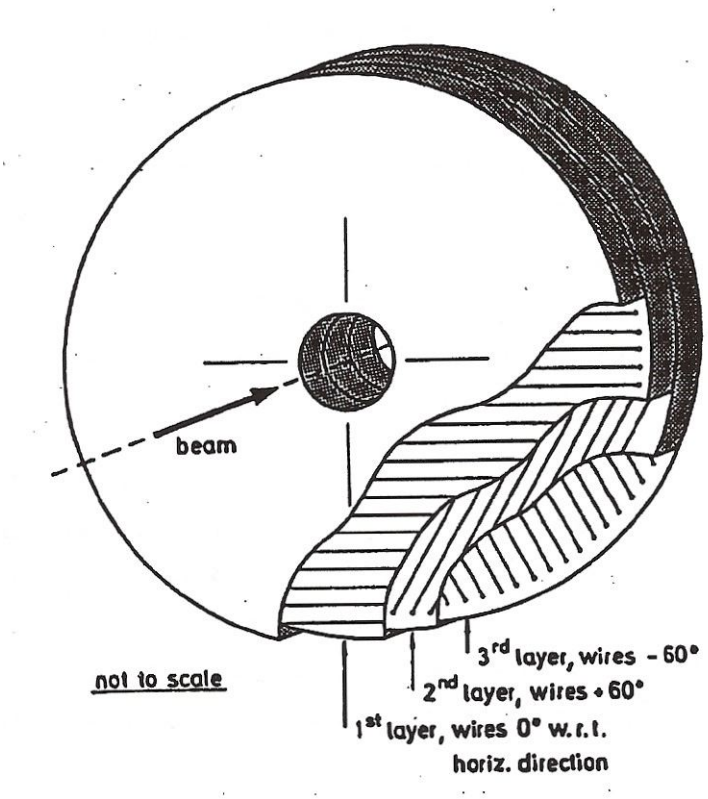

Figure 3.3: Sketch of an FTD subchamber.

interactions. The shower results in an anode pulse which is read out by FADCs as in the CTD. The primary purpose of the TRD is to permit electron tagging. Transition

radiation is not produced by πs with momentum below $40\ \mathrm{GeV/c}$[22] so while πs and electron have similar dE/dx characteristics the pulse shapes produced will differ. This should allow the TRD to distinguish between the two with a discrimination factor of 100 (for electrons with energies between $1\ \mathrm{GeV}$ and $30\ \mathrm{GeV}$).

3.4 The Rear Tracking Detector (RTD)

The RTD is basically identical to one FTD subchamber but of slightly smaller size. Its sensitive volume extends down to 10° in the rear direction.

3.5 The Vertex Detector (VXD)

In order to obtain improved resolution, the design of the VXD progressed assuming the use of a 'slow' gas; dimethyl ether was chosen. This then meant that the cell size would be smaller than in the CTD in order to restrict drift times to a reasonable length. Constraining the number of readout channels led to a maximum drift time of $500\ \mathrm{ns}$ over a distance of no more than $3.6\ \mathrm{mm}$. There are twelve sense wires at $3\ \mathrm{mm}$ intervals in a VXD cell.

Taken in conjunction with the CTD, the VXD will improve the resolution with which tracks coming from the interaction region may be measured. The design goal is to improve the resolution on the impact parameter to $50\mu\ \mathrm{m}$ or better. This enhances the prospects of identifying particles with short lifetimes which decay before they leave the interaction region. If this occurs, the VXD may be able to separate tracks coming from the interaction in which the short-lived particle was created, and those coming from the point at which it decayed. There will be no z information from the VXD.

Chapter 4
The ZEUS Trigger Environment

4.1 Introduction

Triggering is the selection of physics events of interest in conjunction with the rejection of background processes which it is not desired to investigate. The success of any HEP experiment is critically dependent in its ability to achieve a high trigger efficiency. Identification of interesting physics must be as close to perfect as possible in order to avoid the introduction of unacceptable systematic errors and to maximize the amount of recorded data relating to physics events. A trigger is a complex entity comprising, at HERA, readout electronics, hardwired algorithms and much sophisticated software running on powerful dedicated processors well matched to particular tasks.

At HERA, triggering has assumed even greater importance than in the past partly due to the high rates of background and partly due to the short beam-crossing interval of only $96\ \mathrm{ns}$. At other machines, a longer interval simplifies trigger design so that no pipelining of data is required. For example, the Large Electron-Positron collider at CERN has a crossing every $10\mu\ \mathrm{s}$. Experience gained at HERA will prove invaluable in the design of the yet more complex triggers which will be required at the next generation of colliders, notably the Superconducting Supercollider in Texas which will have a beam crossing interval of $16\ \mathrm{ns}$.

4.1.1 Overview of Dataflow

An overview of the system is shown in figure 4.1. each component feeds data to local pipelines and the global first level trigger (GFLT). If this decides to accept the event, the pipelines are read out to the second level trigger (SLT): raw data from each component remains separate at this stage though the global second level trigger (GSLT) can clearly consider the results from processing in all components. If the GSLT issues an accept, the event builder (EVB) assembles the whole of the information

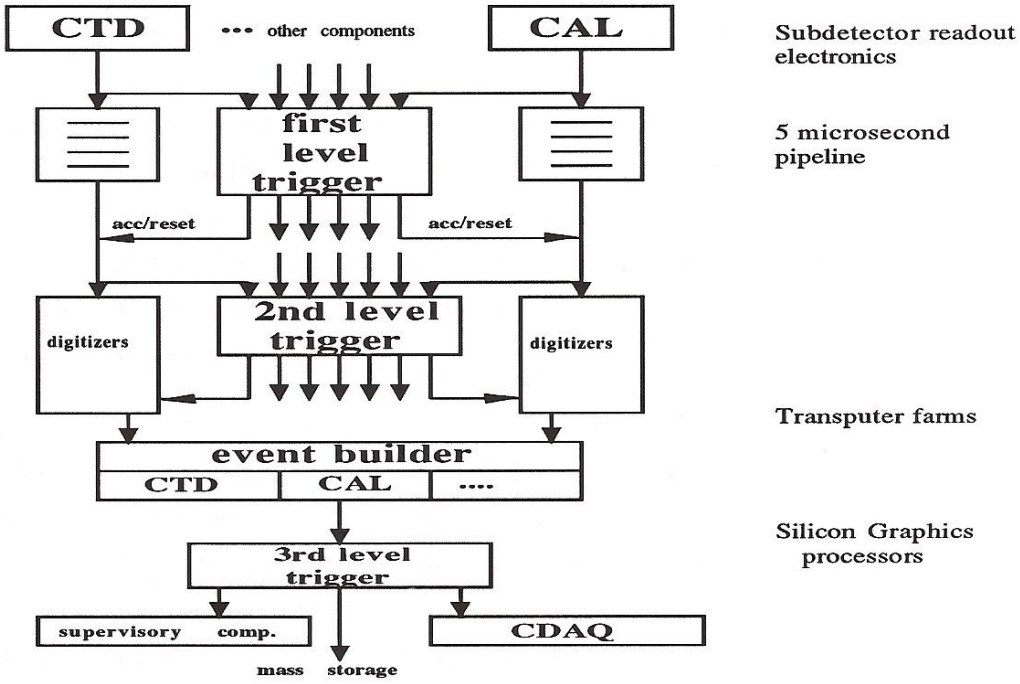

Figure 4.1: Flow of data through the DAQ system.

acquired for the event and sends it to the third level trigger (TLT). This, mediated by the Central Data Acquisition (CDAQ) VAX and run control (RC), writes events passing the final stage to tape. There is also some facility for local disk storage.

4.2 Rates and Background

The trigger philosophy has been developed with the characteristics of physics events in mind. These in general have many tracks coming from the origin which will be observed in the tracking detectors. large depositions of energy, especially at thigh angles to the beamline, often result from physics processes. If there is a neutrino in the final state, this will not be seen by any part of ZEUS and so and asymmetry in transverse energy may be found.

It is envisaged that there will be three main sources if background in ZEUS; cosmic rays passing through the detector, losses from the proton beam, and interactions of the beam with residual gas inside the beampipe. The latter are known as *beamgas* interactions and much effort has been expended to try and devise triggering strategies to prevent them from causing triggers.

Cosmic ray events will on the whole be rejected by the use of timing information from the calorimeters.

Protons not following the nominal beam trajectory hit machine elements thus producing hadronic showers including pions. These can subsequently decay into muons which are very penetrating. There are approximately 2×10^{13} protons in the beam. The circumference of the ring is $6336\ \mathrm{m}$ If it is assumed that the beam will have a lifetime of about ten hours, these interactions may occur at a rate of up to $100\ \mathrm{kHz}$ per metre of beamline. However, structural elements such as collimators, beam scrapers and the vetowall will substantially reduce the rate of these events causing activity in the detector.

It is estimated that the rate of beamgas interactions will be up to $2\mathrm{kHz}$ per metre [23]. Near the interaction region they will fake good events in the tracking trigger. Upstream of it, their modest energy deposition may be misinterpreted by the calorimeter as a high transverse energy deposition representing a large Q^2 interaction. This is because upstream tracks which are in fact only leaving the beampipe by a shallow angle can arrive a long way away from it once they are intercepted at the interaction region. Also, upstream beamgas can have secondary interactions producing tracks which come from the interaction region. This background is potentially the most serious.

All of these backgrounds can be reduced by combining together triggers from different detector components. These have different discrimination powers against the various types of background and by combining them in a flexible way the sensitivity to physics can be maintained while minimizing the background. This is discussed in the next section.

Assuming the design luminosity of $1.5 \times 10^{31}\ \mathrm{cm}^2\ \mathrm{s}^{-1}$ leads to the rates shown in table 4.1 for events observed in the acceptance of the ZEUS detector.

Process	**Rate**
DIS NC	0.075 Hz
DIS CC	0.001 Hz
BGF J/Ψ	0.045 Hz
BGF $b\bar{b}$	0.015 Hz
beamgas	100 kHz
cosmic rays	5 kHz
proton halo	~ 100 kHz

Table 4.1: Rates of physics and background.

4.3 The Trigger

As mentioned above, the ZEUS trigger will have three levels. In order to allow more sophisticated processing on a more complete subset of component data at successive levels, each level will have a longer period of time with which to make a decision. This is shown in table 4.2.

Level	**Time**
First	5μs
Second	~ 7 ms
Third	~ 0.3 s

Table 4.2: Processing time allowed per event by level of trigger.

4.3.1 The First Level Trigger

it is impossible to decide whether or not to accept an event within the $96\ \mathrm{ns}$ between beam crossings. In the first level trigger (FLT) [24] [25] [26], this forces the storage of data in *pipelines* which must be able to hold data relating to $5\mu\mathrm{s}$.

Processing takes place both at the level of individual components and in the *Global First Level Trigger Box* or GFLTB [27] [28] [29] [30] [31] [32]. because of these constraints the sophistication of processing that may be done by components at this level is restricted. The output rate from the FLT will be $1\ \mathrm{kHz}$, after the fast clear section 4.3.1.2.

The components must write the data relating to the event to their internal pipeline. Each of the components have 26 beam crossings to perform calculations on their data. They must then send the results of these calculations to the GFLTB. If the GFLTB decides to accept the event, it will send an accept bit to each component exactly 20 beam crossings later. The GFLTB must therefore complete its calculations within this 20 beam crossing period. The components then read out the relevant data to the *component* second level trigger.

The tracking detector FLT is is central to the work presented in this thesis. Its discussion is therefore postponed to the following chapter.

4.3.1.1 Calorimeter FLT

The calorimeter first level trigger (CALFLT) [32] [33] [34] is designed to detect isolated electrons and muons and to measure momenta and energy deposition. it is essential tp use angular information in this trigger. The distinction between transverse energy and momentum in the CALFLT is an important one. Momentum is a vector quantity whereas energy is a scalar. The difference between energy and momentum is expressed in the statement that momentum is signed so that tracks in a opposite hemispheres might sum to give zero transverse momentum whereas energy would always add. transverse energy is a calculated value in which depositions at high angles are accorded more weight. This quantity is a good measure of activity in the detector characteristic of desired physics events. Lookup tables (LUTs) are used to consider transverse energy

deposition in order to recognize patterns associated with good events.

The original intention to measure longitudinal momentum will not now be fulfilled due to financial reasons.

The calorimeter is mostly non-projective: only the electromagnetic section of the barrel has cells aligned parallel to lines radiating from the interaction point. For this reason, the subdivision of the calorimeter into regions for trigger purposes is different to its physical division. Entities known as 'trigger towers' are formed from calorimeter cells such that a straight line from the interaction point will be fully contained within them.

Most towers contain two electromagnetic calorimeter (EMC) cells representing approximately 25 radiation lengths as was shown in table 2.1. Beyond that are the two paris of HACs (hadronic cells) which map most closely on to the EMCs. In a small number of towers at the edges of the FCAL and of the RCAL, the BCAL is between the first cell in the tower and the interactions region. In this case, the tower contains only HACs (see section 2.2.1). The makeup and number of towers in the calorimeter is shown in table 4.3 .

Region	**Number of towers**	**Number with EMCs**
FCAL	460	264
BCAL	448	448
RCAL	452	262
sum	1360	974

Table 4.3: Calorimeter tower numbers and makeup by location.

It can be seen from the table that there are a total of 1360 towers: these all provide a HAC sum. Of this total, 974 also provide an EMC sum. The non-projective cells must be grouped into projective towers. This is done by using the EMC sections to define tower geometry and then assigning HACs behind them to form a tower with the best possible match. It transpires that 896 projective towers with a sensible geometric

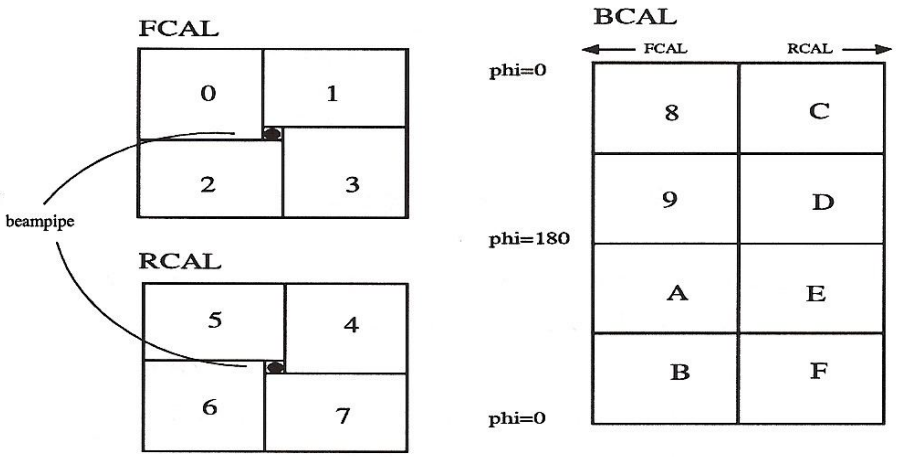

Figure 4.2: Trigger regions in the calorimeter.

division emerge from this process. The calorimeter is now divided into sixteen trigger regions: four for each of the RCAL and FCAL and eight for the barrel. This is shown in figure 4.2. Each region contains 7×8 towers.

Each calorimeter cell is read out by two photomultiplier tubes. EMC and HAC energy depositions are summed within a tower by onboard cards known as trigger sum cards (TSCs). These sums are sent to trigger encoder cards (TECs) in the rucksack: each TEC covers four towers. So there are 14 TECs in a crate to cover the 56 towers in each of the sixteen trigger regions.

For each tower, EMC and HAC energy deposition is measured on two digitization scales by flash analogue-to-digital converters (FADC): high gain (12.5 GeV on an 8 bit scale) and low gain (400 GeV over 8 bits in the FCAL and 100 GeV over 8 bits in the RCAL and BCAL). If the deposition exceeds a scale an overflow bit is set. If neither the HAC nor the EMC in a tower set off the high-gain channel, the TEC ceases to perform energy sum calculations and begins testing for electrons and minimum ionizing particles as described later.

The geometric position of each tower in terms of θ and ϕ is known to the TEC. It

uses these and the finest resolution energy scale available (depending on whether the high or low gain channel has been used) to find transverse energy depositions. Total and transverse energy sums for the four towers covered by each TEC are sent to a trigger adder card (TAC). There are two of these in a crate.

The TEC's run test procedures may result in three bits being set for each tower. An E-bit is set if the depositions found are characteristic of an isolated electron: these will predominantly deposit their energy in the EMC part of a tower. The design aims to find all electrons with energy greater than $5\ \mathrm{GeV}$.

The EMC threshold is set at $2.5\ \mathrm{GeV}$ however since an electron may deposit its energy in adjacent cells. Since there is a small likelihood that an electron with energy between $2.5\ \mathrm{GeV}$ and $5.0\ \mathrm{GeV}$ will 'punch through' the EMCs to reach the HAC layer, only $0.1\ \mathrm{GeV}$ is allowed in the HAC layer. If the EMC deposition is greater than $5.0\ \mathrm{GeV}$, then the ratio $\frac{\mathrm{E_{EMC}}}{\mathrm{E_{HAC}}}$ must be greater than 10. A slightly different requirement is implemented in the more active FCAL but clearly the requirement for this bit to be set is also based on substantial symmetry between the two types of cell.

The rate at which charged particles passing through matter lose energy by ionization depends on their energy. In fact, the rate decreases to a minimum and then increases to a plateau at high energy. Particles above the minimum are called minimum ionizing particles or MIPs. The energy deposited by a particle at the minimum in a tower is shown in table 4.4.

Cell Type	$\mathrm{E_{MIP}}$**/MeV**
BEMC	321
BHAC	1360
FEMC	363
FHAC	2268

Table 4.4: Total HAC and EMC energy deposited by a MIP by location of tower.

If a situation not unlike the reverse of what is necessary to set the E-bit occurs, then an M-bit (M is for minimum ionization particle) is set. it is required that the

deposition E fulfills the condition $0.2\mathrm{E_{MIP}} \leq \mathrm{E} \leq 2\mathrm{E_{MIP}}$. It is generally likely that a muon is the cause. Muons are comparatively penetrating and so do not deposit most of their energy in the EMCs. Genuine hadrons will usually have energies which are much too large to set the M-bit.

Towers in the active region around the beampipe are not permitted to set E or M bits. If insufficient energy is deposited to set either of these bits, LUTs are used to find if the tower is 'low-activity' for the Q-bit. 'Q' stands for 'quiet'. In fact, the requirement to set the Q-bit is that the pulse height be less than 20% of the pulse height required to set the M-bit.

In the TACs, pattern logic searches for groups of up to four E or M-bits set and surrounded by Q-bits in each of the sixteen regions. NC events have a high-energy isolated electron and this pattern logic forms an excellent trigger on these events. On the other hand, isolated muons are characteristic of many interesting physics processes including heavy quark production.

The exact thresholds for these bits vary depending on the location of the tower being processed. The thresholds for the E, Q and M-bits must be matched to each other because otherwise a legitimate electron may fail its isolation requirement. Therefore a quiet tower is defined by having less than the minimum EMC energy for an E-bit and the minimum HAC energy for an M-bit. For example in the FCAL a quiet tower must have $\mathrm{E_{EMC}} < 2.5\,\mathrm{GeV}$ and $\mathrm{E_{HAC}} < 2.268\,\mathrm{GeV}$. These bits are sent to the CALFIT processor.

The CALFIT processor receives the energy sums for the sixteen regions and also on a finer *subregion* scale. This finer scale is designed to have better resolution around the beampipe and to prevent loss of the flexibility to examine data relating to areas covered by more than one trigger crate. The CALFIT processor will be able to examine in this way deposition in the FCAL and the RCAL in annular regions at different radii from the beampipe. this is useful because beamgas events are more likely to have high deposition around the beampipe region than physics events for Q^2 values of interest to ZEUS.

Sums are made of the number of towers in each region which have energy sufficient to set the bits. This enables the processor to search for jets which will appear as clusters of towers with bits set.

The processor sends data to the GFLTB relating to the whole calorimeter and to the 16 subregions. The global data is: E_{EMC}, $E_{EMC} + E_{HAC}$, $E^x_{EMC} + E^x_{HAC}$, $E^y_{EMC} + E^y_{HAC}$, E^x_{EMC} , E^y_{EMC} , missing energy, cluster data and the total number of E and M-bits set. Further, the result of a beamgas likelihood algorithm[1] is sent. On the subregion scale, the M and Q-bitmaps are sent to the GFLTB long with E_{tot} , E_{trans} , E_{emc} , E_x and E_y .

4.3.1.2 Fast Clear

To ensure that the accept rate to the second level trigger is no greater than 1 kHz an element of parallel processing of calorimeter data has been introduced [35]. The fast clear (FC) will consider data simultaneously from the FCAL, RCAL and BCAL relating to events which have had an FLT issued. Each accept is accompanied by an indication of whether the GFLTB will permit the FC to abort the event, based on the strength of its acceptance by components other than the calorimeter.

The FC works by searching for clusters [36] and finding their angle and energy. Cuts are made to discriminate against beamgas which can be quite stringent compared to those in the FLT because the FC will be permitted to abort a trigger only if the other components show a weak accept decision.

An important quantity in the FC is shown in equation 4.1

$$E_f = \frac{E_{EMC}(RCAL) - E_{HAC}(RCAL)}{E_{EMC}(RCAL) + E_{HAC}(RCAL)} \tag{4.1}$$

In CC events, hadron jet do not often have trajectories which take them through the RCAL. On the other hand, about 80% of particles in beamgas interactions are hadronic. So physics events have high-angle clusters with large E_f. It has been shown that a cut based on this ratio for the highest energy cluster in the RCAL yields a

[1] This uses the regional energy sums and also the sum of energy in the beampipe region (because beamgas events cause much activity here). Also the presence of towers showing kinematically disallowed energies is a useful sign. Because they have upstream vertices, beamgas events can fake larger transverse energy than would be possible for any real event.

rejection factor of 400[37]. this clearly indicates that efficient recognition of electron or hadron jets is possible.

If an abort does occur, the GFLTB stops component readout to the second level. The FC operates in around $10 \rightarrow 30\mu$s. This is longer than the 5μs available to the GFLTB because the FC does noes not have to consider every event. In this way, more detailed considerations of clusters are possible thus enhancing efficiency while the design goal of 1 kHz input to the GSLT is not compromised. In fact, the exact amount of time available depends on the FLT rate but flexibility has been inbuilt here by simply declaring that the FC will cease incomplete operations on an event and allow it to proceed through the readout chain as soon as the next FLT decision is issued.

4.3.1.3 Other FLT Components

Forward muon detectors A muon trigger[38] will be formed taking account of direction and momentum by requiring a strip-to-strip coincidence between first and last planes of streamer tubes (LT1 and LT5, see section 2.3.1). The susceptibility of this method to background is reduced by additionally requiring signals in corresponding ϕ-sectors of all five planes LT1 to LT5, as shown in figure 4.3. The time-of-flight plane will assist the association of a triggered muon with its correct beam-crossing. The FMUFLT will have three subdivisions in terms of polar angle as shown in table 4.5.

Region	θ range	Detector sections
very low	$5^\circ \rightarrow 7^\circ$	LT2, LT3, LT4
low	$7^\circ \rightarrow 15^\circ$	LT1,LT2, LT3, LT4
high	$15^\circ \rightarrow 32^\circ$	LT1, LW1, LW2

Table 4.5: FMUFLT polar angle subdivision.

Correlation matrices select tracks consistent with having originated in the interaction region. this is done by logically dividing the readout channels into θ and

ϕ windows as shown in figure 4.4 for the BMUO. The RMUO is covered by four sections.

Vetowall signals indicating the passage of a muon from the beam halo inhibit triggers in the RMUO while CTD timing data reduce the cosmic background in the barrel to a manageable level.

Coarse scale muon multiplicities are sent to the GFLTB: these give the number of muons found in left or right barrel and rear regions.

Vetowall By virtue of its presence, this device (section 2.4.1) will reduce rates from beamgas and beamhalo[39]. Apart from the veto signal to the RMUO described above, it is instrumented to set three flags. These will indicate to the GFLTB the presence of signal in the inner and outer scintillator planes and sum up such activity to produce a multiplicity.

Luminosity monitor The LUMI[40] continuously scans the energies of photons registered in its photon detector and of electrons in its other subcomponent. The energies measured are sent to the GFLTB. The LUMIFILT raises a flag if the arrival times and the sum of the two energies are consistent with a bremsstrahlung event in the interaction region: $\mathrm{E_e} + \mathrm{E_\gamma} = \mathrm{E_{beam}}$. A photoproduction flag indicates $\mathrm{E_e}$ in a proper window and photon energy below a threshold (in practice no deposit).

Leading proton spectrometer Horizontal and vertical position measurements will be made for the FLT in the last three stations (section 2.4.3). Coordinates in the three planes are linearly related for straight tracks from the interaction region (figure 4.5). Selection logic searches for valid spatial coincidences.

Beam halo events however are expected to produce a rate of $3\,\mathrm{kHz}$ so this will not be a standalone trigger. By combination with an independent trigger the GFLTB will use the hit pattern from the LPS to obtain an additional background rejection factor.

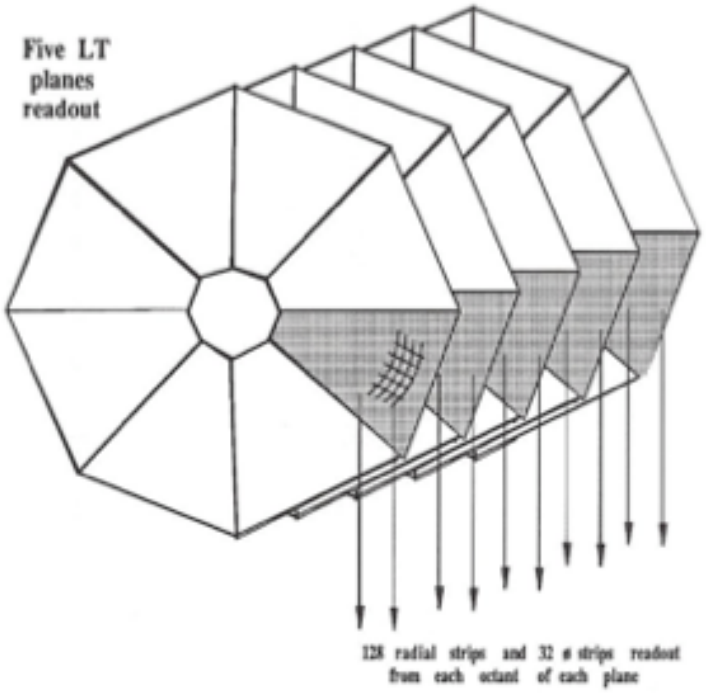

Figure 4.3: Forward muon detector first level trigger.

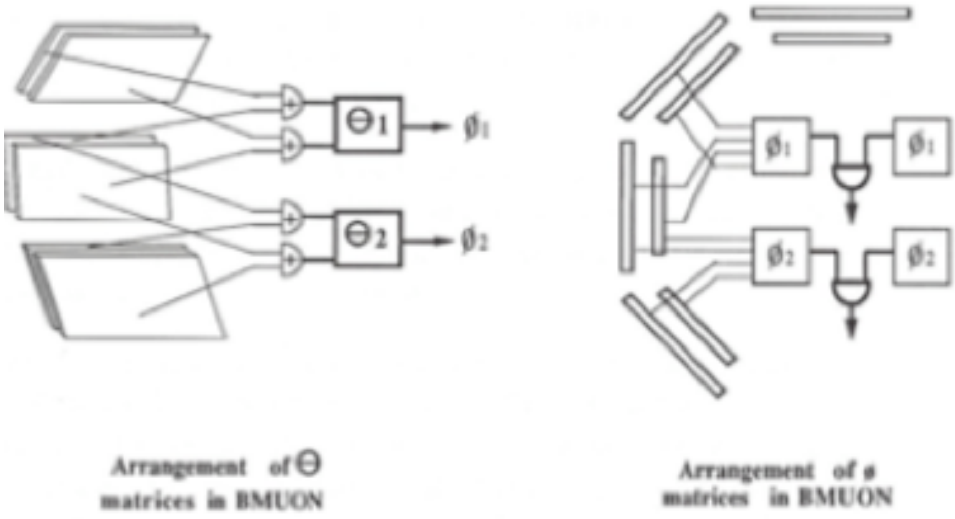

Figure 4.4: Barrel muon detector first level trigger.

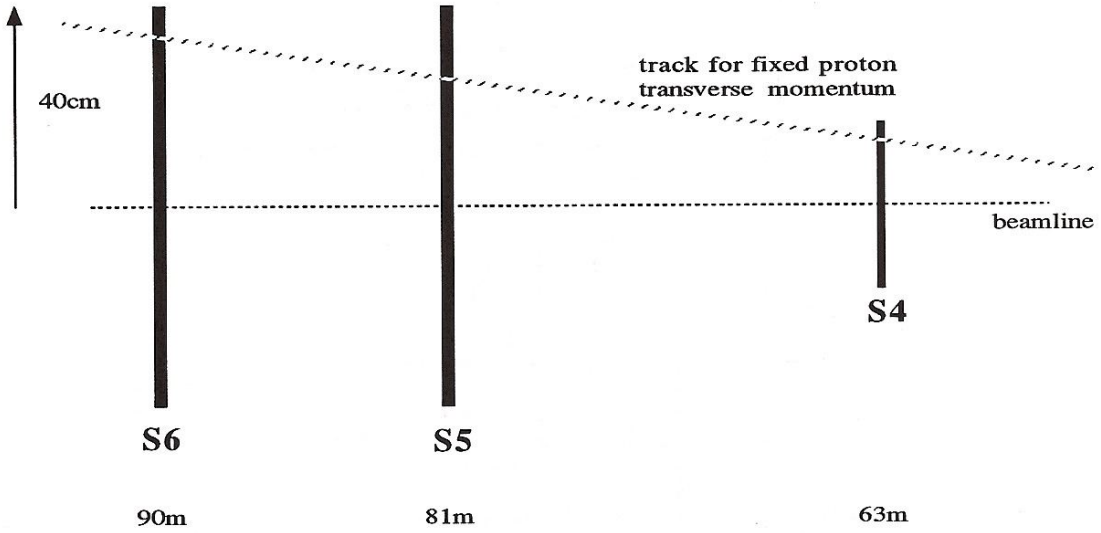

Figure 4.5: LPS input to FLT: proton search.

4.3.1.4 Global First Level Trigger Box

The GFLTB collates data from all participating components and performs calculations to make the final decision at this level on whether or not to accept an event. It also has test and calibration functions. It will send data to RC enabling online investigation of deadtime, luminosity *etc*.

To make an event decision, it performs logical operations of great complexity. These have been designed to a high level of sophistication in advance of data taking at ZEUS, but flexibility exists to make adjustments because it is certain that reality will differ to some extent from simulation.

The information from the components comes on 16-bit cables. Fifty-one 16-bit words of data arrive for every beam-crossing. This information is fed into a set of subtriggers. The hardware allows for 64 such subtriggers to be defined, all of which must eventually be combined into a single decision. The subtriggers are grouped into

several functional classes dealing with similar data as shown in figure 4.6.

An example of the kind of cross-matching possible in the global box may be seen from the diagram: isolated muons found in the calorimeter are correlated with tracks from the tracking detectors which may plausibly have been produced there by the same muon. Further, transverse energy from the calorimeter is multiplied by the track count from the tracking detectors: this quantity should be large for good events.

4.3.2 The Second Level Trigger

The SLT has access to a more complete and precise set of data than the FLT by virtue of the longer timescale on which it operates. It is currently envisaged [41] that the Global Second Level Trigger (GSLT) box [42] [43] will make an event decision available to components around $7\ \mathrm{ms}$ after the beam crossing. Unlike the FLT, the SLT is *asynchronous*: different parts of the system are at any given moment analyzing data which was not all acquired at the same time.

4.3.2.1 Tracking Detector SLT

The algorithm for the CTDSLT [44] [45] [46] [47] [48] proceeds in two stages: segment finding [49] and track finding [50]. Segment finding is the grouping of hits in an eight-wire cell to produce small portions of tracks: these are then combined to form a complete track. The pulse heights from the DSPs (section 3.2.3.1) will enable electron tracks to be identified when the events are fully reconstructed because their characteristic dE/dx differs from that of other charged particles.

Drift times are the input to the CTDSLT which resides on a network of transputers. These are microprocessors with four bidirectional communication channels which mean that a wide range of topologies are available. They have their own language (occam [51]) which is deigned to fully exploit the inherent parallelism of the networks. For applications in the CTDSLT, factors of four improvements in time requirements have been measured using occam [52] as compared to more conventional languages.

In axial SLs only, hits in each cell are examined to find track segments. Each cell is considered in turn, and the 'single cell mask' is stepped around the whole chamber.

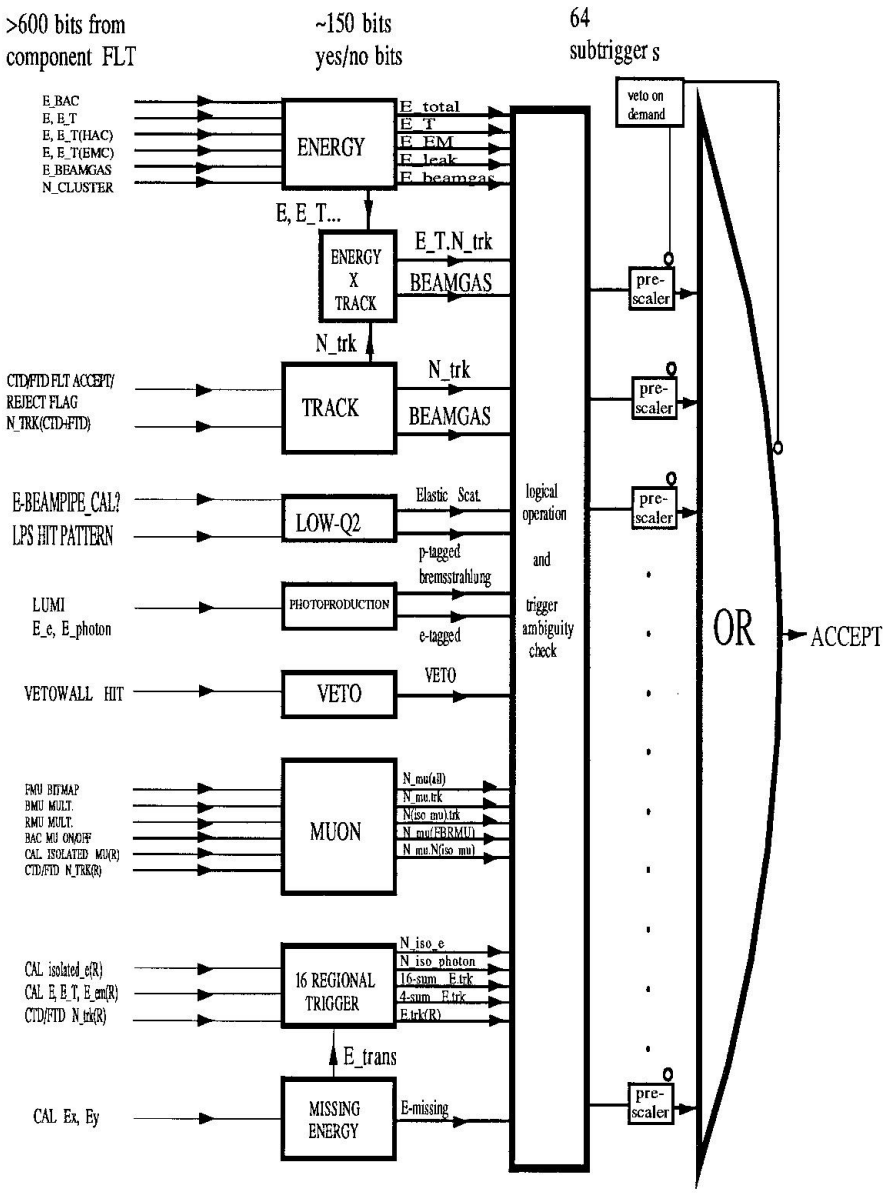

Figure 4.6: Schematic of logic in the GFLTB.

'Roads' are defined so that the drift time at the nest wire is predicted from the previous hit on a segment. The gradient, intercept, variance and the mean z and r coordinates are passed on to the track finding stage.

The track finding sorts segments in overlapping octants making use of their angular values to consider groups likely to be on the same track. Three-dimensional tracks are formed from z-by-timing data associated with $r\phi$ segments via a straight line fit in rz.

The CTDSLT will send two tables of results to the GSLT. Exit point and direction and $\mathrm{p_t}$ will be available with error estimates for each track that has been found. Also the charge and origin will be known. The vertex for the event as a whole is calculated, as is the total number of tracks found together with an estimate of how many tracks were missed (from the number of unused segments).

The present design of the FTDSLT envisages a tree search method which will be implemented in online memory. It will identify coordinate outputs from the chamber corresponding to straight tracks from the interaction region.It will require one cell hit in each layer: this corresponds to a polar angle requirement of $7\,^\circ \leq \theta \leq 30\,^\circ$. The FTDSLT should find all such tracks with momentum over $1\,\mathrm{GeV/c}$ coming from within $20\,\mathrm{cm}$ of the vertex.

4.3.2.2 Calorimeter SLT

As is common in the SLT as a whole, transputer networks are used for readout and triggering[53].

Timing of energy deposition in the calorimeter is very precisely measured at the second level. Because the distance from the interaction region is not the same for the FCAL and the RCAL there will be a $2\,\mathrm{ns}$ difference in arrival times for good physics events. More importantly, most beamgas events originate from upstream of the interaction point at negative z-coordinates. These are expected to produce a difference in arrival times of $12\,\mathrm{ns}$[54]. This permits discrimination between physics and background. Prior to this enhancement of capability, the design called for those calorimeter towers around the active beampipe region to be disbarred from setting isolated electron bits because of the intolerable leakage rate that would result. With

this timing information however it appears that this restriction may be relaxed thus improving efficiency. In addition, events with unphysical longitudinal momentum will be vetoed.

4.3.2.3 Other SLT Components

Other components are in communication with the GSLTB. It is clearly to be expected that the quality and quantity of information available at the second level will in general be superior to that at the FLT.

GFLTB The GFLTB sends the results of its calculations to the GSLTB along with component data and the FC information.

BAC Eight-bit 10MHz FADCs sum charges over two successive beam crossings. Two networks of transputers will be used: one will be in communication with the GSLT and the other with the EVB[55]. If an energy threshold is met, cluster data will be sent to the GSLT. Also, a muon trigger is formed from coincidence logic in the bottom yoke where there are no muon chambers. The data should in general be more precise than that from the BACFLT.

BMUON Coordinates of found muons should be available.

FMUON The FMUSLT will make an estimation of momentum from the sagitta of the particle found at the first level using the LT planes.

LPS A bit will be sent to the GSTLB to confirm or negate the LPSFLT. Further, a measurement of the proton momentum is made and is expressed as a fraction of the beam momentum. Horizontal and vertical projections of the transverse momentum of the proton are supplied.

LUMI The measurements made at the first level remain available. Further, the location of electromagnetic shower centres is measured and also photon shower centres if the bremsstrahlung flag is up.

VETO The number of hits and their positions should be available.

4.3.3 The Third Level Trigger

The composition of the code to be run a this level[56] has proved to be quite volatile. This is due to two factors. Firstly, there is great uncertainty as to the form of events, both background and physics, which will survive the first two levels of trigger. because of the high efficiency with which these reject beamgas, the entire Monte Carlo production which has taken place so far has resulted in only around 350 events (from a generated sample of 750000). this is clearly not a large enough sample to base definitive conclusions on.

Secondly, the compute power available within resources at this level has fluctuated. The system is now based on Silicon Graphics (SGI) processors, the specification of which have quite considerably improved over time. Initially, it was thought that code would need to be written specially for this application: later it seemed that it would be possible to run the full offline reconstruction code online! At present, there has been some retreat from this bold position so that now it is envisaged that there will be some form of vertex rejection to eliminate remaining beamgas before running the 'offline' code. Possibilities for this include pattern recognition or a helix fit to find tracks and look for upstream vertices. Use of CTD stereo layers will permit a better z-resolution so as to improve on the SLT. Also, the VXD data becomes available here for the first time. It is likely that most of the remaining beamgas will have a vertex very close to the interaction region so improvement of the resolution here is the critical factor.

The TLT[57] [58] [59] is intimately linked to the Event builder (EVB). The EVB resides on transputer-based standard 'VME' boards similar to those of the GSLT and CALSLT. The EVB assembles the events and makes them available in a Triple Port Memory. The TLT then reads events into SGI workstation memory.

It is hoped that the SGI workstations will provide an online event display, These will also read out the EVB to IBM and VAX computers. The IBM will write events to tape with a rate of $0.5\ \mathrm{Mb\ s^{-1}}$. The speed with which this is possible is the final constraint on the whole of the trigger. Over $100\ \mathrm{Gb}$ will be accumulated during a year of operation.

The amount of processing time is a function of the input rate and the number of TLT nodes. It is currently envisaged that there will be 32 $4D/35$ processor nodes and 6 $4D/25$ machines handling communications. The time allowed per event is given by dividing the number of nodes by the number of events which must be handled every second: $32/100 = 0.32\,\mathrm{s}$ per event.

The VAX is the main Central Data Acquisition computer (CDAQ) and represents the interface between the experiment and operators in the control room. Many interlinked processes will run on the CDAQ VAX. Run control will start TLT processes and setup runs without human intervention. For monitoring purposes, RC will be connected to components down optical transputer links running from the rucksack to the control room. These will carry 'analyse', 'reset' and 'error' signals. Slow control will monitor parameters not varying on the timescales of beam crossings, such as temperatures in the racks housing readout electronics. cooling fan status and gas flow rates.

Chapter 5
Tracking Detector FLT

5.1 Introduction

The processing of data from the CTD and the FTD will be integrated at the output stage of the tracking FLT. The RBOX is responsible for this. Chapter **??** describes how performance benefits mat be obtained by extending track-finding methods to use data from both of the tracking detectors. It is likely for financial reasons that there will be some staging of detector readout and trigger electronics. For this reason, the RBOX is able to run separately the two tracking detector standalone triggers which are described here.

5.2 CTDFLT

There are four types of readout module in the CTDFLT: cell processors for SL1, SL3 and SL5 (CP1, CP3, CP5) and sector processors (SP). Measurement of the z-coordinate is central to the CTDFLT, the principle of which is show in figure 5.1.

5.2.1 Cell Processors

The z-by-timing value (see section 3.2.3.2) from the FADC is converted to a z/r bin number before input to the CPs. This is a fairly simple operation (because the radius is constant for a given SL) which is carried out by PROMs[60] on the z-by-timing cards. The CPs work with these values because straight tracks at constant polar angle will produce several hits in the same z/r bin. This means it is relatively straightforward to perform pattern recognition in this space to find such tracks.

Pairs of cells are read out by each CP[61] because the tilt of the cells means that straight tracks from the origin will pass through two cells. The CPs search fro patterns

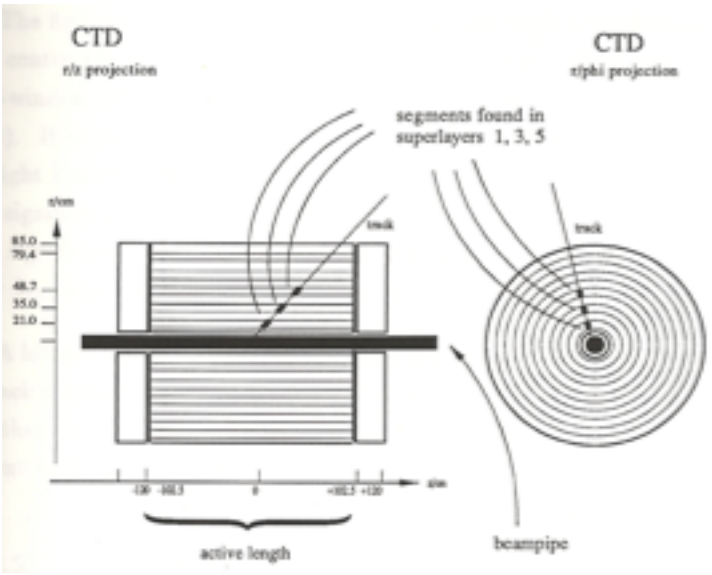

Figure 5.1: Principle of the CTDFLT.

of hits at the same z/r. This pattern recognition logic is implemented in two stages consisting of RAM lookup tables and Xilinx[62][1] field programmable gate array (FPGA) chips which are also used in the GFLTB.

The input stages of the CP1 boards consider hits arriving within a short timespan of each other in an 8×32 bit table. The eight bits represent the layer number within SL1 and 32 bits is the division into z/r for this SL. Due to hardware constraints, the entire table cannot be processed simultaneously but instead is considered in a 4×8 bit window. This window is stepped along the 32 bit length of the table. Each window is further subdivided into an upper and lower half of 4×4 bits. For each half, a $64\text{k} \times 4$ RAM produces four bits from the input z/r pattern:

- Vertex cut bit
- Centre cut bit
- pattern weight (two bits)

[1] These allow logical networks of great complexity to be defined. Their most important property is that the networks may be reconfigured in the light of new requirements.

The first bit is set if hits are found consistent with a track from the vertex and the centre bit is set if the hits were mostly in the middle two bins of the 4-bin half-window (this reduces the frequency with which the same track sets bits in two CPs). If wires are missing in a sequence of hits they ay still be formed into a straight line from the interaction point but it is desirable to accord such a pattern less significance than one which has all wires hit. The pattern weight is a measure of this significance. Analogous processes take place in CP3 and CP5 boards but here only four wires in a cell are instrumented for z-by-timing.

A hit pattern in a cell consistent with the hits being part of a good track is called a track segment. The CPs form a 31-bit word which is a z/r bitmap. This indicates whether or not candidate segments have been found in that particular z/r bin and is sent to the relevant SP.

5.2.2 Sector Processors

There are thirty-two SPs corresponding to the number of cells in SL1. Because tracks curve in the magnetic field, more than one CP in the larger radius SLs sends data to a SP. In fact, four CP3s and six CP5s are 'OR'ed together to constitute a single trigger sector, as shown in figure 5.2.

Tracks from the interaction region which have a polar angle of greater than approximately 26° will cross all three instrumented SLs. Assuming that there are no inefficiencies, this would mean that three segments would be found by the CPs. Each SP proceeds by trying to match segments. If the line joining segments in SL5 and SL1 points to the vertex to within some cut, and also passes through SL3 within ± 1 bin of a segment there, then a good track has been found.

Six bits allow for communication from each SP to the rBOX, which must combine information from all sectors to produce a decision for the CTDFLT as a whole. These six bits consist of three track bits and three vertex bits. The vertex bits come from processing in rz and the track bits come from $r\phi$ processing.

If in a particular sector a good track has been found as described above, then the

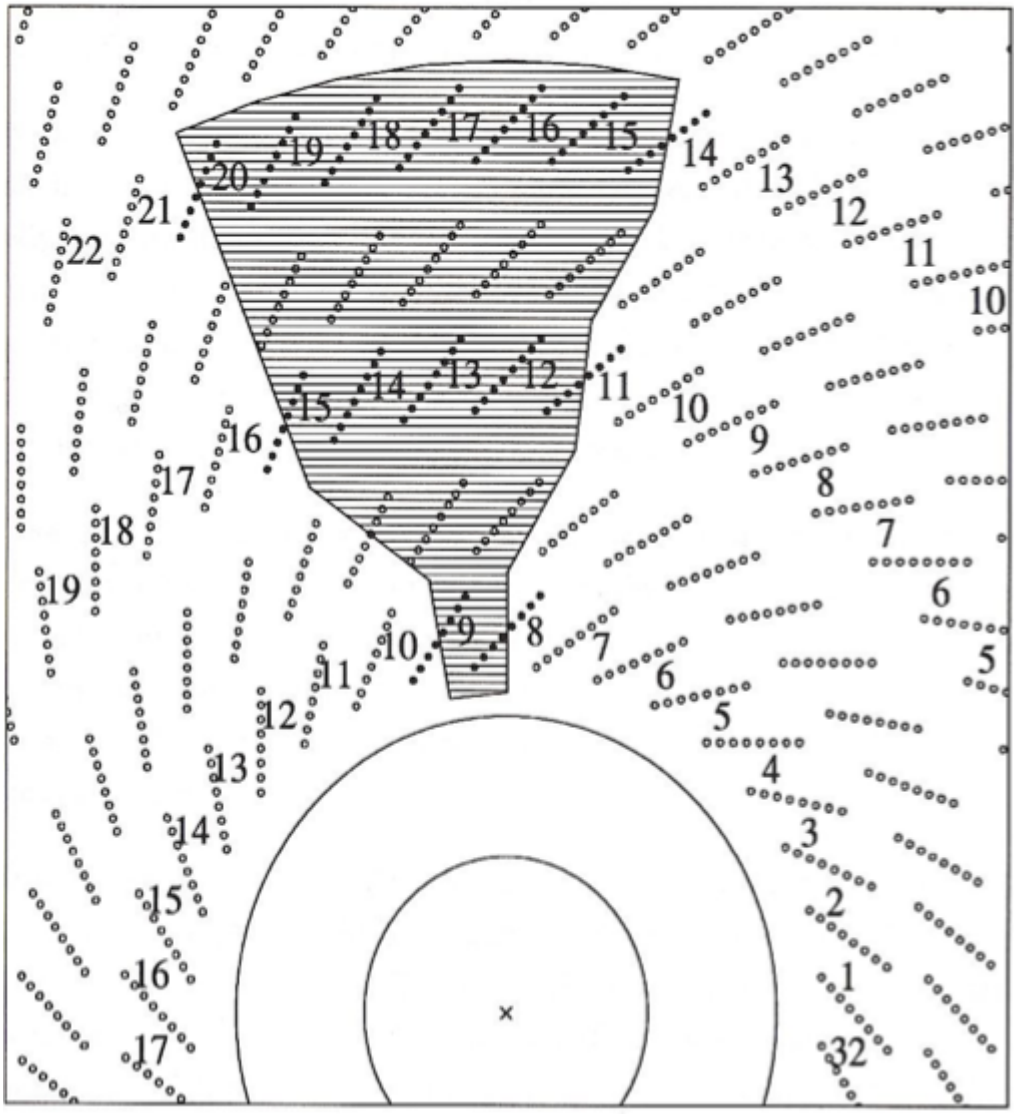

Figure 5.2: One of the 32 trigger sectors of the CTDFLT.

SL5 vertex bit is set. This indicates that successful extrapolation of at least one SL1 segment out to SL5, including a SL3 segment, to find a combined track which points to the vertex has taken place.

However, it is possible that the SL5 segment is not found, if for instance the track has a polar angle such that it leaves the CTD before reaching SL5. In this case it is still possible to do trackfinding by combining segments in SL1 and SL3 only. The SL3 vertex bit is set if extrapolation is successful to this extent. If the rz processing in SL1 finds a segment, the SL1 vertex bit is set.

The three track bits, on the other hand, are measures of activity which has been formed into a track by the relevant CP but which may or may not have come from the vertex. The SL1 track bit indicates that there were sufficient hits in the CP1 in a sector for it to be able to form a track segment. If in addition this was true in one of the CP3s assigned to this sector, then the SL3 track bit is set. Finally, if all three instrumented SLs contain track segments then the SL5 track bit is set.

It is thus to be expected that a single good track within the θ region covered by all instrumented SLs will set all three vertex bits. A real event will of course usually contain more than one track and it is likely that some of these will be due to secondary interactions which will have origins distinct from the interaction region. A decision must be made in the RBOX as to what extent the event looks as if it consists of a minimum number of tracks coming from the interaction region - clearly a description satisfied by a good physics event.

The CTDFLT decision is made by the formation of a ratio; this is the central idea of all the tracking detector triggers. Ratios are formed representing how closely the event conforms to the hypothesis that it emanates from the interaction region and a cut is made on this ratio in order to reject background. The value of the cut is a tunable parameter and has very great influence in the optimization of the particular trigger.

It is the purpose of the three track bits from each SP to permit such a ratio to be formed. The numerator will be a function of the vertex bits, of which large numbers

will be set by a good event. The denominator is a function of the track bits which are a measure of activity in the detector. If the ratio is high this means that a large proportion of activity in the detector is associated with good found tracks and the event may be triggered on with some confidence.

There is much overlap of information relating to the same tracks between different CPs and SPs which therefore need to have a high degree of connectivity. The 16 crates in the whole system, each of which contains the trackfinding and z-by-timing boards for 2 trigger sections, are linked together in a circle so that data from adjacent trigger sectors is available to the processors.

All crates use a customized backplane which concentrates readout bus lines, system control, timing and power supply in the bottom third allowing up to 300 interconnections to be made between cards.

5.2.3 Processing

The RBOX forms several ratios in its processing to produce a final CTDFLT decision which is based on two cuts. Firstly it finds the number of sectors which have their SL5 vertex bits set . It divides by the number of sectors which have their SL5 track bit set.

If the ratio so formed is greater than a cut then the event is accepted. In the simulation this cut is presently set to be 10%. An accepted event is labelled class two in the case of the CTD. If the ratio is less than the cut value but there are nevertheless more than two segments in SL5 then the event is rejected (class one).

For events which fall into neither of the above two classes, the SL1 data is utilized. If the ratio of sectors with their SL1 track bits set divided by the number with vertex bits set is greater than a cut, then the event is placed in class three. This cut is now set at 25%. These are quite possibly good events but one will have less confidence in accepting them. At present these events are simply added to the class twos in order to boost physics acceptance but it is important to remember that scope exists to treat them differently. For example the class threes might be required to fulfill more stringent conditions at later stages of processing.

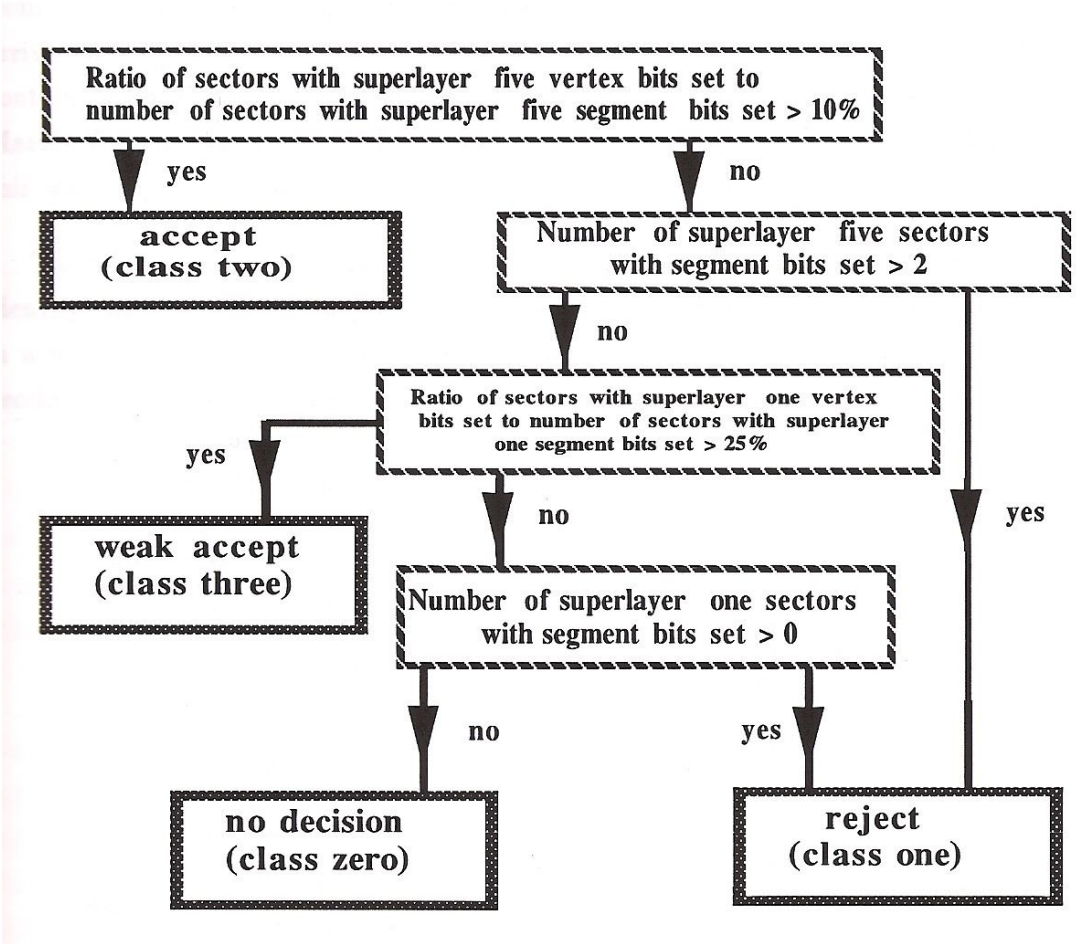

Figure 5.3: CTDFLT event classification flowchart.

The possibility exists to introduce a similar procedure for SL3 segments but studies so far have not looked at this question in sufficient detail to prove the necessity to do this. An additional class of accepted events could thus be provided for.

If the event has failed to be classified so far, then an assessment is made of its information content: if it has and segments in SL1 then it is rejected. If this is not the case, there is insufficient information for the processors to work with and the event is classified zero or 'no decision'. Table 5.1 shows the classes and figure 5.3 shows diagrammatically how they are arrived at.

Class	meaning
Three	'weak' accept
Two	accept
One	reject
Zero	no decision

Table 5.1: Summary of CTDFLT event classifications.

5.2.4 Timing

Other elements of the system are related to timing considerations. Since the drift times are longer than the beam crossing interval, the CTD will contain ionization from more than one crossing at any given moment. It is necessary to consider the arrival times of pulses in order to assign them to a beam crossing. Each crate contains a Local Timing Controller (LTC), each of which is connected to a separate Master Timing Controller (MTC) which receives clock signals from the GFLTB. In this way, the LTCs make a time signal in $48\ \mathrm{ns}$ bins available on each crate.

The CPs have logic designed to recognize patterns and sequences of hits so as to identify the crossing which produced the trigger. A misidentification would result in a $96\ \mathrm{ns}$ difference between measured and real drift times for hits which would produce easily recognizable effects on segments as shown in figure 5.4.

An arrival time circuit (ATC) works in parallel with the pattern recognition. This generates two flags- 'new' and 'valid'. The ATC works in $48\ \mathrm{ns}$ timebins (*i.e.* two per beam crossing) and the new flag is set if a hit arrives which was preceded by three empty bins. This can be regarded as the first hit of a new event, as shown in the same figure. The maximum difference in arrival time of hits from the same track on adjacent sense wires occurs if the track passes through a wire and is given by $\Delta \mathrm{t} = \frac{\mathrm{d}}{\mathrm{v_d}}$, where d is the separation between sense wires, equal to $8\,\mathrm{mm} \times \cos\phi$, ϕ is the angle of the track with respect to the sense wires and $\mathrm{v_d}$ is the drift velocity. Using the nominal drift velocity of $50\ \mu\mathrm{mns}^{-1}$ this means that $\Delta \mathrm{t} = 160\ \mathrm{ns}$ with $\phi = 90°$. This is more than the three bin ($48\,\mathrm{ns} \times 3 = 144\,\mathrm{ns}$) gap requirement. However, ϕ will not approach $90°$ but will be closer to $45°$ for tracks from the interaction point. It follows from this

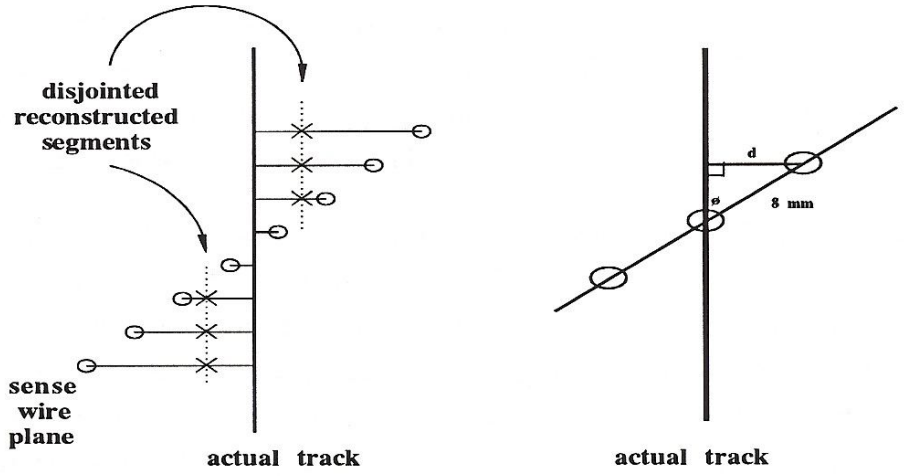

Figure 5.4: Effect of crossing misidentification on segments and maximum difference in drift times on adjacent sense wires.

that the maximum gap permitted in a sequence of hits is 2 bins if they are to all be considered a part of the same event. The maximum drift time covers ten bins and so the valid flag is set ten bins after the new flag was raised and remains up for one timebin or until the last hit in the sequence arrives. The flag is sent directly to the output stage of the CPs.

5.3 FTDFLT

5.3.1 Introduction

The Forward Tracking Detector First Level Trigger (FTDFLT) is based on the same principle as the CTDFLT: straight tracks from the interaction region are again searched for. However the different geometry of the two detectors means that different logic is necessary to achieve this.

As described in section 3.3.1, the FTD has three subchambers each containing planes of wires with 60° relative offsets. These planes are known as u, v or w-layers

depending on their orientation. The planes contain a large number of wires which cannot be used individually in the trigger because of hardware constraints. For example, the number of connections which may be made to a single electronic readout board is a limiting factor. It is necessary to OR wire signals together in such a way as to retain sufficient resolution to leave the FLT efficiency unimpaired.

5.3.2 Diamonds

The concept of *diamonds* [63] [64] was developed to represent an optimal method of combining cells. Two of the three planes in an FTD subchamber are used to define a hit location, simply by 'AND'ing the hits together. These must then be confirmed by a further hit cell in the third plane. This third cell is not required to be exactly in coincidence with the first two: the precision of the match is a parameter which may be adjusted in order to optimize performance. At the moment, it is envisaged that either the central cell in the third layer or either of the two adjacent cells may confirm a diamond.

Figure 5.5 shows the method of forming diamonds. A cell numbering convention has been defined whereby for good three-dimensional combinations, the sum of hit cells will be zero. There is a further combination of diamonds into superdiamonds in the outer regions. Near the beampipe where high resolution is required, the processing to find hit diamonds proceeds exactly as described. However, further out, they are combined into larger entities composed of 2×2 standard diamonds. At the largest radii, a superdiamond contains nine standard diamonds.

For financial reasons, only FTD subchambers one and three will be instrumented with diamond logic. It can be seen by similar triangles (figure 5.6) that if a pair of superdiamonds found in the two detectors lie on the same straight track from the interaction region, then their coordinates are related by

$$\frac{Z_{\mathrm{ftd1}}}{r_{\mathrm{ftd1}}} = \frac{Z_{\mathrm{ftd3}}}{r_{\mathrm{ftd3}}} \tag{5.1}$$

Conversely, tracks emanating from upstream of the interaction region will fail to satisfy this relationship by an amount which increases proportionally to their distance from the nominal interaction point.

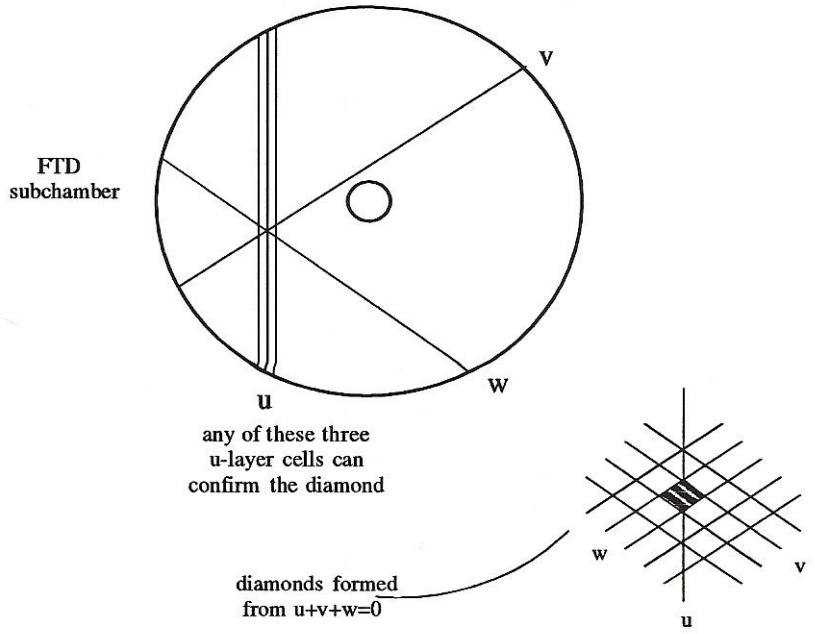

Figure 5.5: Method of diamond forming to confirm three-dimensional hits.

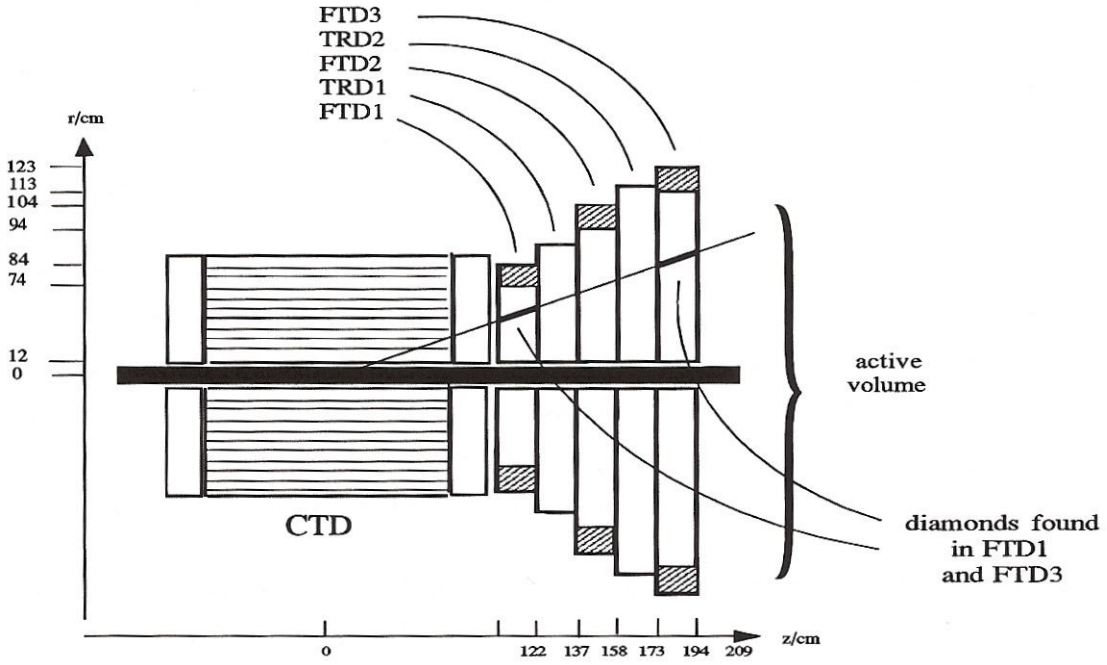

Figure 5.6: Principle of the FTDFLT.

The wire planes are orthogonal to the z-axis, and the u, v and w-layers are separated by $5\,\mathrm{cm}$ in z. In principle it would be necessary to examine how layers have been used to form a superdiamond. However it has been shown [65] that in fact this small correction is not significant. It is therefore assumed that the same z-coordinate is obtained everywhere in a subchamber and so this reduces to a simple factor which can be applied to the radius of a hit superdiamond in FTD1 to predict the radius of a matching superdiamond. For infinite momentum tracks, the ϕ coordinate should be the same for both superdiamonds.

These principles form the basis on which the FTDFLT works. It attempts to match superdiamonds from FTD1 with those from FTD3. In the ideal case, all superdiamonds in a good event will be matched. In practice, some superdiamonds will fail to be matched because of inefficiencies and interactions *etc.* The FTDFLT finds the ratio of superdiamonds in FTD1 which have been matched with FTD3 superidamonds divided by the total number of FTD1 superdiamonds and makes a cut on this quantity. This is a valid approach since beamgas events have fewer tracks coming from the interaction region, and hence will have less correlation of superdiamonds between the two subdetectors.

5.3.3 Hardware

Figure 5.7 shows the hardware design for the FTDFLT. The chamber will be readout by FADCs as described in section 3.3.1. These are interfaced via a discriminated postamp signal to cellhit boards (CHBs) [66] which produce hit wire numbers. Each CHB should be able to contain logic units able to read out 32 cells. This means that a total of 16 CHBs, fitting into a single crate, will suffice for the FLT readout of FTD1 and FTD3. As shown in the diagram, this CHB crate has 3 fan-outs linked to 2 fan-ins on the second crate. The second crate contains 6 Sextant Boards (SBs) and 6 Segment Builder Modules (SBMs). This subdivision is a consequence of the FTD geometry.

The SBM and CHB electronics will rely on Xilinx FDGAs for logic implemented by lookup tables. These chips will be reprogrammable by the ROC. The CHBs will define hit cells by requiring a minimum number of hit wires out of the 6 in a cell.

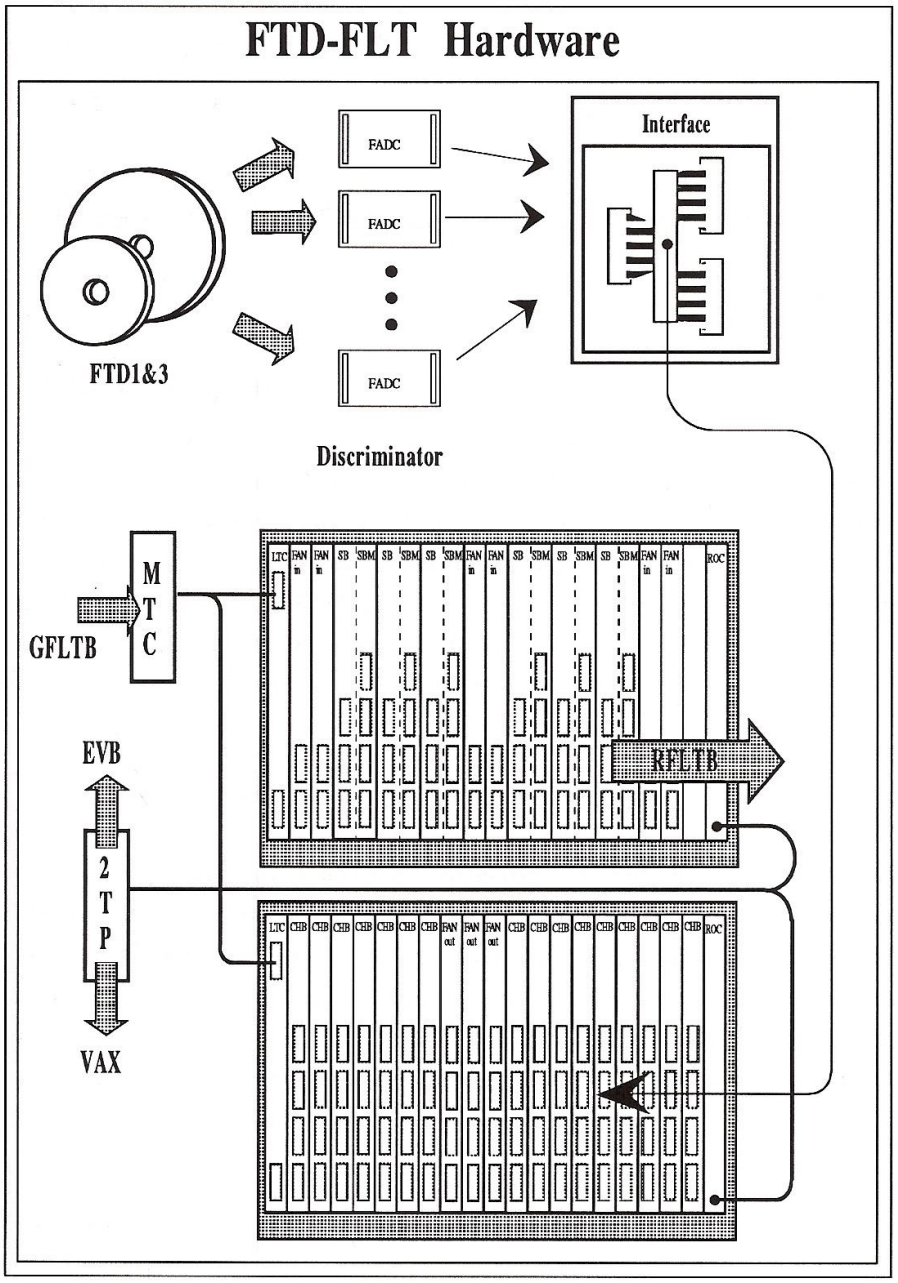

Figure 5.7: Outline of two-crate FTDFLT hardware design.

The SB logic will form superdiamonds from hit cells and then apply coincidence logic to search for tracks from the interaction region in the manner previously described. Finally the SBMs use hit and coincident diamonds to from the ratio for the FTDFLT decision and also to prepare for matching with CTD data.

Timing considerations are as important in the FTD as in the CTD since the FTD also contains ionization from more than one crossing at any given moment. A five bit shift register is connected to each wirehit with each bit corresponding to a beam-crossing interval. An OR of the last four bits is fed into the CHB so that each hit remains valid over sufficient time such that all hits pertaining to a particular event will at some point be considered together.

Finally, the Readout-Controllers (ROCs) are responsible for sending information concerning the status of the FTDFLT to RC and the EVB, for handling of test data, and for reading out the contents of registers *etc.* for diagnosing trigger performance

Chapter 6
The Regional First Level Trigger Box

6.1 Introduction

In this chapter the operation of the RBOX is described. It's development has proceeded by using a simulation of the entire detector. First an overview of the purpose of the RBOX is given in this section. After describing the simulation the principles of the algorithm under which it will function are considered. Results are presented supporting the conclusion that combining tracking detector information leads to definite benefits. An outline of the hardware design is given.

6.1.1 Requirements

The RBOX must provide track angular information suitable for matching to the calorimeters. If a track points in a certain direction, it will be desirable to extrapolate to the relevant calorimeter component and look for energy deposition. Also it is necessary to produce an event classification for the GFLTB. This classification must describe whether the integrated tracking FLT has accepted an event. This indicates the confidence with which the detectors have identified the event as containing a high proportion of tracks coming from the interaction region.

6.1.2 Information Available to the RBOX

The RBOX receives information from hardware in the CTD and the FTD, as described in section 5.2. In both cases the hardware is divided into units relating to the subdivision in ϕ of the two detectors. In the CTD, there are thirty-two *sector processors*: the CTD is divided in ϕ into 11.25° sectors. In the FTD the sextant processors each handle a 60° section.

The RBOX will receive the multiplicities of matched and unmatched superdiamonds from the sextant processors. This means a measure of the amount of activity in the

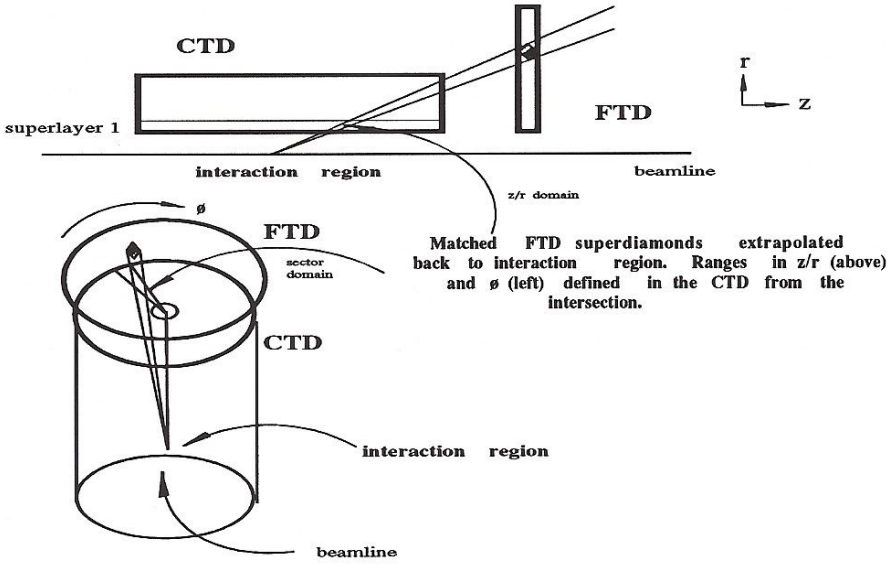

Figure 6.1: Mapping of the FTD onto CTD to define coincidence domains.

detector is possible. Further, the sextant processors will output the coordinates of matched superdiamonds to the RBOX in a from suitable for matching with the CTD. In order to do this, it was necessary to know the coordinate ranges of superdiamonds which might be matched with a given segment. These ranges are termed coincidence domains. Once the domains have been defined, each matched superdiamond could be assigned to a 'pseudobin' and a 'pseudosector'. These are simply the sector or z/r bin in which it would be expected to find CTD segments given various diamond positions. This is illustrated in figure 6.1.

In the simulation for which results are presented later in this chapter the coincidence domains were deduced empirically. Large numbers of single straight tracks from the origin were simulated. It was arranged that these tracks would have polar angles such that all possible coordintaes for matched sets of superdiamonds and segments could be found. This produced very simple results in the trigger simulation: pairs of matched superdiamonds and three matched segments were nearly always found. the coordinates of the superdiamonds, together with the corresponding coordinates of the matched segments, were noted. the RBOX will use the domains defined to perfom matching between the FTD and the CTD.

6.1.3 Processing

The RBOX will use the subtriggers which had been developed for the individual detectors as previously described. However each does not now represent a final decision but rather makes up a part of the information used by the RBOX to form a decision. The FTDFLT version used in the simulation which will be described in this chapter is identical to that which had been used standalone. However the version of the CTDFLT used in the RBOX simulation was modified in the light of the new situation of combining data with the FTD. This RBOX 'quasi-CTD' ratio is similar to the standalone CTDFLT in that it considers a ratio formed from matched segments over total segments. However the RBOX uses only SL5 segments whereas the standalone CTDFLT uses more SLs as described diagrammatically in figure 5.1. it remains useful however to compare these RBOX results with the code that was developed for the CTD alone as described in the previous chapter. This is what is meant in this chapter when when results described as CDT standalone are given for comparison.

The main extension possible in the RBOX is to produce a combined trigger which uses both subtriggers as appropriate and also forms completely new ratios using information from both detectors. In this way maximal coverage in θ can be achieved together with performance improvements.

6.2 Simulation

The simulation was carried out using the ZEUS trigger version[67] of the Geant program, in conjunction with the ZEUS trigger analysis program ZGANA[68]. Both programs have been undergoing continuing evolution so a continued effort has been necessary to keep work up to date as new versions are released.

6.2.1 Geant and ZEUSGeant

Geant[69] [70] is a program written at CERN which is designed to be a universal physics simulation which may be applied by collaborations of particle physicists to the particular geometry peculiar to their detector. Since its inception in 1974 it has greatly

extended its functionality and is in wide use on many different types of machine. Like a great many scientific programs today in existence, it is written in the FORTRAN language. it is fully integrated with graphics packages also from CERN[71] [72]. The combined package has found wide application in the HEP community and all the work presented in this thesis utilizes it.

The code is distributed via PATCHY[73] machine-independent format. This is designed to allow any of a set of common computers/operating systems (*e.g.* DEC VAX/VMS, IBM, SUN workstations) to generate FORTRAN code suitable for running on that machine. Large files are initially issued which are then operated on by smaller 'correction sets' as bug reports are filed and additions to the code are made which are not so substantial as to warrant a new version. This mechanism also allows the substitution and addition of special user programs for the purpose of code development.

The Program relies on the concept of 'volumes' which are defined in terms of their size, shape and composition. The facility exists to create detector elements using a set of standard three-dimensional templates. Clearly, structures of arbitrary complexity may be constructed by use of many such volumes. Sixteen standard materials are defined in terms of their densities, radiation lengths and nuclear absorption lengths. Other materials may be added to the standard list. In this way, a very precise simulation of how any detector will interact with a particle can be produced.

Geant makes use of the ZEBRA[74] management system which aims to utilize computer memory efficiently by allowing definition of data structures at run-time.

This is advantageous because FORTRAN does not allow variable length arrays. This package is also useful in terms of reducing disk space requirements. This is crucial because very large data volumes result from the necessity to have large numbers of events in studies so as to provide adequately small statistical errors. To give a flavour of this problem, a standard data sample of one thousand CC events required in excess of 124 Mb of storage space at the time of writing.

Geant accurately simulates the dominant physics processes over an energy range from $10\,\mathrm{keV}$ to $10\,\mathrm{TeV}$. To do this it contains interfaces to may previously standalone

programs and can consider a large number of processes, as shown in table 6.1. Geant contains information about 48 particles: again, the user may define others if this is required.

Photon processes	**e^+e^- pair conversion**
	c $\rightarrow$Compton scattering
	photoelectric effect
	induced fission
Electron/positron processes	**multiple scattering**
	ionization and delta ray production
	bremsstrahlung
	annihilation of electrons
Muon/antimuon processes	**decay in flight**
	multiple scattering
	ionization and delta ray production
	bremsstrahlung
	direct e^+e^- pair production
	nuclear interaction
Processes involving hadrons	**decay in flight**
	multiple scattering
	ionization and delta ray production
	hadronic interactions

Table 6.1: Geant physics processes.

The ZEUS version of Geant mainly consists of a set of command procedures which make the physics routines accessible together with a description of the ZEUS detector in terms of the volumes and materials mentioned earlier. This description is obviously an entity of great complexity, mirroring the nature of the detector. It requires at present around 50000 lines of FORTRAN.

Some additional physics processes which are of special interest at HERA are also added at this stage. For example. background processes which are expected to be

important have internal generators. In particular, beamgas interactions may be studied using either the UA5[75] or FRITOF[76] packages. The differences between these two are discussed in section 6.4.3.1.

6.2.2 ZGANA

Once the ZEUS Geant program has been run, a datafile is created representing the response of the detector to the physics events generated. The presence of the detector of course affects the numbers and trajectories of particles produced and this too has been simulated. It now remains to simulate the function of the trigger electronics. This is the purpose of the ZGANA package, which contains an extremely detailed specification which is actually larger than the detector simulation itself. A data model based on ZEBRA is used here: the Adamo[77] system. This allows the implementation in code of the way data will flow and the relationships between different hardware groupings.

The VAX specific module Management System[78] was used to control the substitution of user-written code for supplied ZGANA modules and the grafting on of additional code to represent the working of the RBOX. This meant that a realistic simulation of the information available could be obtained and used to develop the RBOX.

6.2.3 Event Generation

A beamgas sample was produced using the FRITIOF generator. These were homogeneously distributed along the beamline from $z = -1900\,\mathrm{cm}$ to $+100\,\mathrm{cm}$. The sample was not filtered to remove events which cause no activity in the detector. The proportion of FRITIOF events resulting in hits in the CTD, FTD, RTD, CAL, HES, FMUON, BAC, LUMI or VETO was found to be 52%.

A sample of 1000 CC events and 1000 NC events was generated to test the response of the subtriggers to physics. A cut of $Q^2 \geq 100\,(\mathrm{GeV/c})^2$ was imposed as is normal to remove the effect of the beampipe on acceptance. The effective ranges of the kinematic variables are shown in table 6.2.

Minimum	Parameter	Maximum
0.0011	$< x <$	1.0000
0.0010	$< y <$	1.0000
100.0	$< Q^2 <$	92330

Table 6.2: Kinematic variables of CC sample.

The variables x,y were generated according to the behaviour of the cross-section in the allowed ranges. Typical resulting distributions are shown in figure 6.2 for x and figure 6.3 for Q^2.

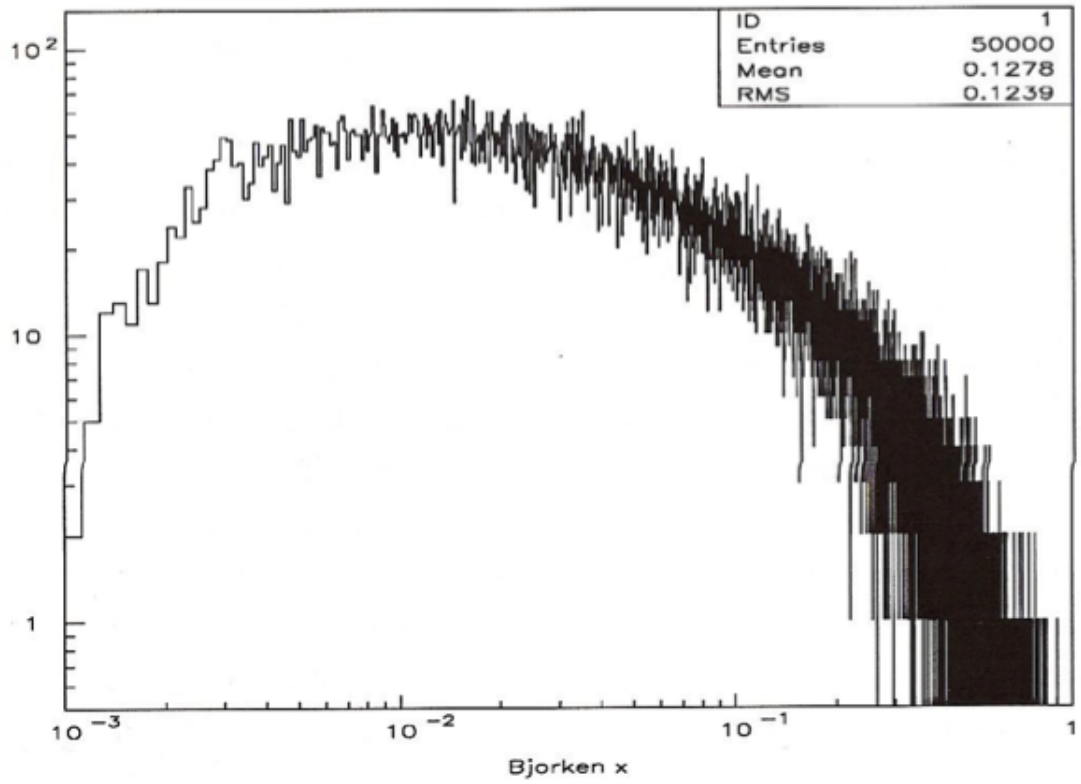

Figure 6.2: Typical values of x for physics sample.

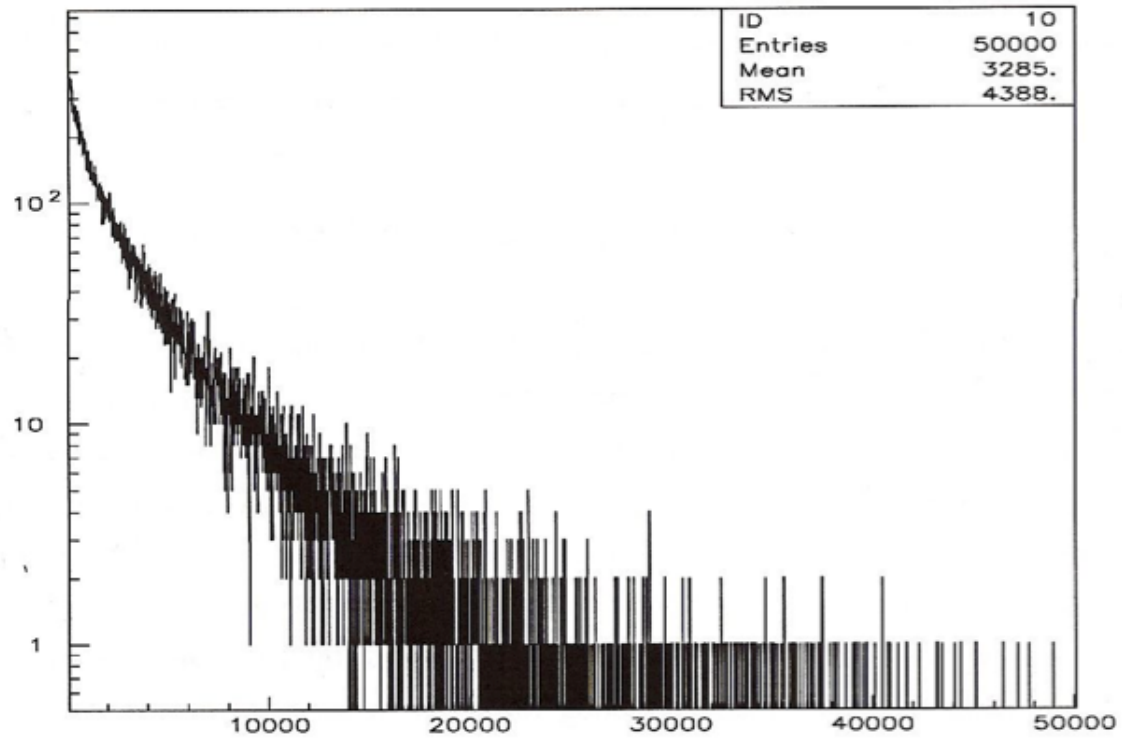

Figure 6.3: Typical values of Q^2 for physics sample.

6.3 Details of the Algorithm

6.3.1 Introduction

In analogy with the two separate FLTs, event classification in the RBOX proceeds from the construction of cuts in four ratios. Each of these constitutes a separate subtrigger. Two of these are more-or-less directly related to standalone subtriggers. One is similar to the CTDFLT ratio and one is identical to the FTDFLT simulation was developed standalone. There are in addition two combined subtriggers which use information from both detectors. Subtrigger three is known as the 'barrel combined' subtrigger. This is because of the spatial region of tracks to which it will be suited. The combined part of this ratio is clearly forward since matching between the CTD and the FTD cannot take place in the barrel region. But the 'CTD only' part of the subtrigger extends the coverage into the barrel region. Subtrigger four only considers matches between the CTD and the FTD and hence provides no useful data in the barrel region. For this reason, it is known as the forward combined subtrigger.

6.3.2 Standalone FTD Subtrigger

The first ratio comes from the FTTD diamond matching procedure in exactly the same way as described for the standalone case in section 5.3.1.

6.3.3 Standalone CTD Subtrigger

There is a 'quasi-standalone' CTD subtrigger which is slightly different to the standalone version which was described in section 5.2. It might be described as a CTDFLT which is biased towards events going into the barrel region since it uses only data from SL5. This means that tracking information is available for polar angles between $25.4°$ and $154.6°$ for this subtrigger. A ratio is formed of the number of segments found in SL5 which are consistent with having come from the interaction region divided by the total number of segments found. Again, a cut is made on this value since it will be close to unity for good physics events and close to zero for background events.

6.3.4 Barrel Combined Subtrigger

Subtrigger three proceeds by using the flags set by the CTD to check all sectors in SL1 for segments which have not been successfully extrapolated. Extrapolation is said to be successful if a pair of segments is found in SL1 and SL5 giving an intersection with the z-axis which coincides with the vertex to within a cut, together with a SL3 segment which is within one z/r bin of the line joining them.

Once those SL1 segments which were unmatched in the CTD have been identified, an attempt is made to match them with the FTD. Having received from the FTD the information in a preprocessed from, it is a simpler matter to try to find pairs of superdiamonds which have the same *pseudosector* and *pseudobin* as previously unmatched SL1 segments. Thus the total number of segments matched either in the CTD alone or in the CTD and FTD combined may be obtained and a new ratio cut produced.

6.3.5 Forward Combined Subtrigger

Subtrigger four operates in a manner quite similar to the barrel combined subtrigger: however it uses a different subset of the total information available. As mentioned in the previous section, the RBOX must provide angular data on tracks suitable for matching with the calorimeter. This data will take the form of an 8×8 bitmap as described in detail in section 6.5. However there is no reason why this information cannot be used by the RBOX in its internal processing: this is the data used by subtrigger four.

Since the purpose here is to match CTD segments with the FTD, the bits set by the RBOX which are intended to facilitate matching with the FCAL are of especial interest. These are termed 'forward bits' or FBINs: in each of eight ϕ sectors they indicate if a good track has been found in each of the three θ regions which would correspond to the FCAL. So the RBOX uses the CTD information to produce the FBINs and do the matching: it is convenient to use the same θ regions for both purposes.

The forward combined subtrigger tries to match all FBINS which have been set in

the RBOX to pairs of FTD1 and FTD3 matched superdiamonds. This is different to subtrigger three which only considers segments which had not been matched already by the CTD.

At this point, every event is characterized by four ratios between zero and one. Each is constructed from the number of matched segments and/or diamonds divided by the relevant total. Good events should produce numbers which will be near to one. Beamgas events will not produce a great deal of correlation within and between detectors and will thus have numbers close to zero.

6.4 Results

6.4.1 Subtrigger Ratios

The ratios obtained for beamgas events are shown in figure 6.4. In all of these plots, the zero bin has been omitted and the number of entries so removed is indicated. The majority of beamgas events actually fall into this bin but these are not of interest because they will in general cause no activity in the detector and no trigger decision will be made. On the other hand, it is possible for events to fall into the zero bin but still to have a non-zero denominator. If this is the case, it means that the event can be positively rejected for it has segments or superdiamonds or both but none of them have been matched. This is a good indication that the event comes from upstream. Table 6.3 shows the proportions of beamgas events which may positively be rejected in this way for each subtrigger.

Figure 6.5 shows the subtrigger ratios obtained for the charged current (CC) sample. This effectively removes the unclassifiable events and so interest clearly lies in this remainder which are likely to reflect the true nature of the background signal passing the trigger. Again, the zero bin has been removed. On subsequent pages, the same plots are shown again (figure 6.6 and figure 6.7) with the zero bins included.

It is apparent from the plots that the forward combined subtrigger achieves much lower matching ratios than the other subtriggers. This is due to the artificial inflation of the denominator: a single segment often sets more than one FBIN. This is because

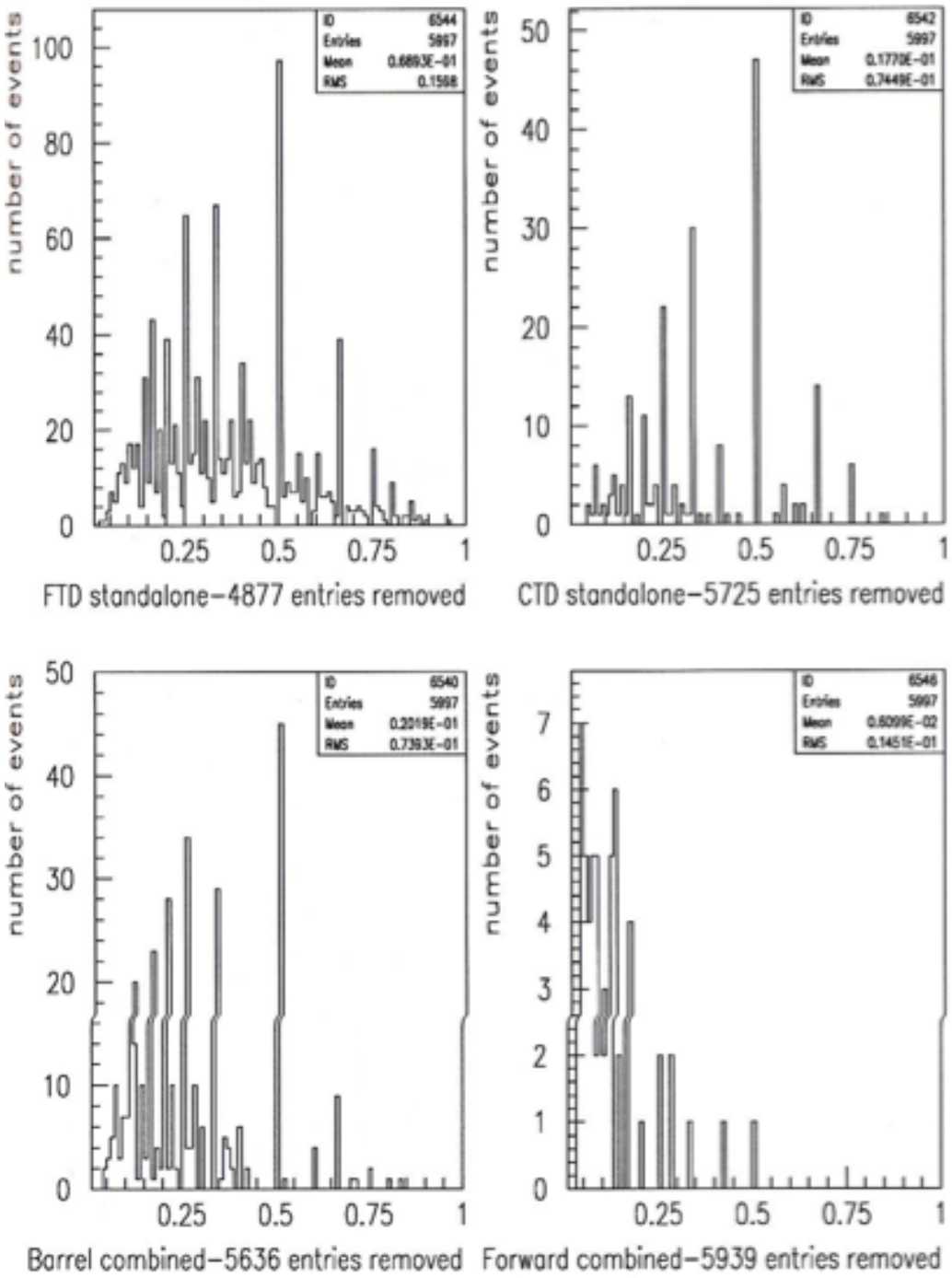

Figure 6.4: Subtrigger ratios for beamgas sample (zero bin removed).

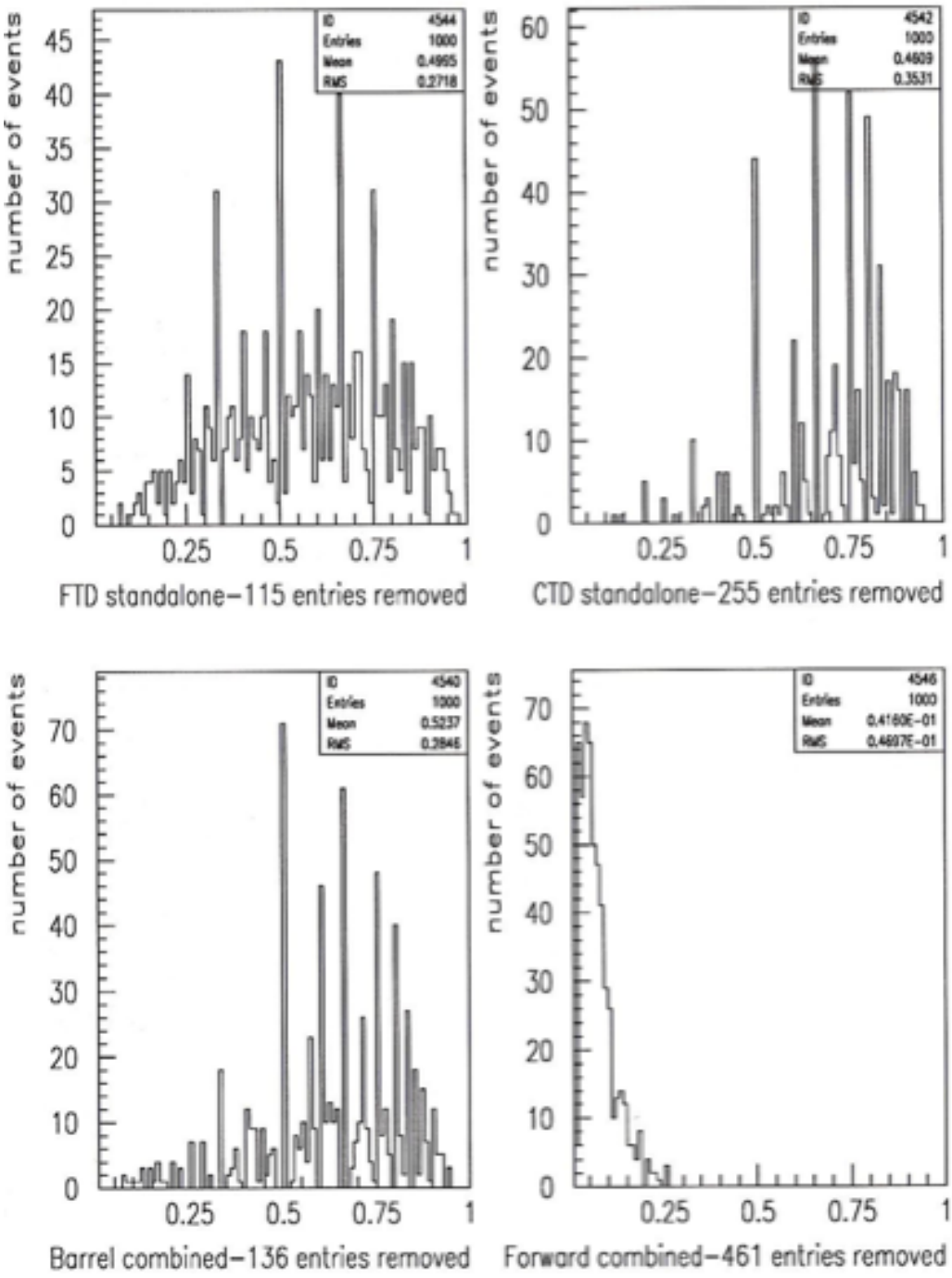

Figure 6.5: Subtrigger ratios for CC sample (zero bin removed).

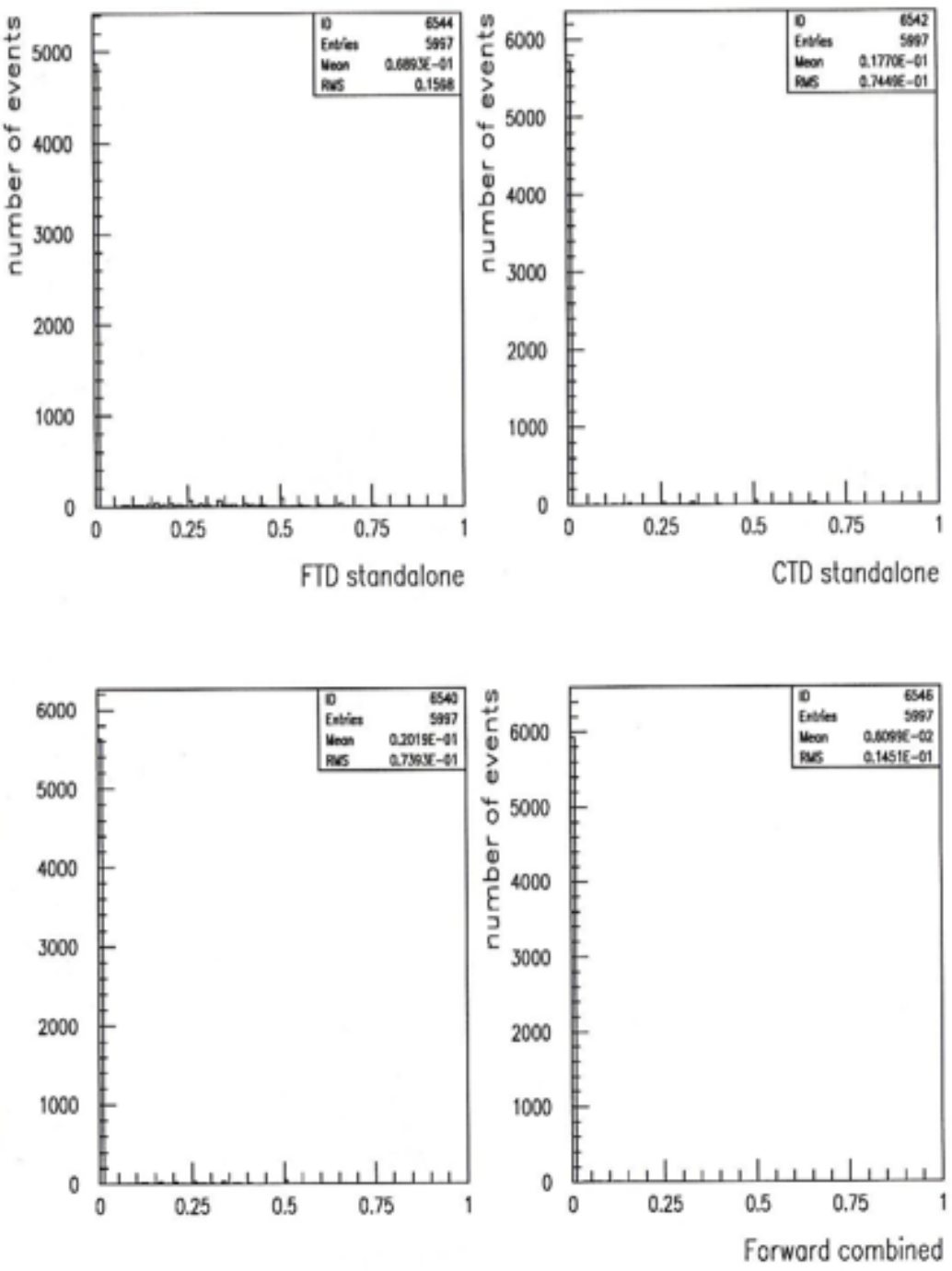

Figure 6.6: Subtrigger ratios for beamgas sample.

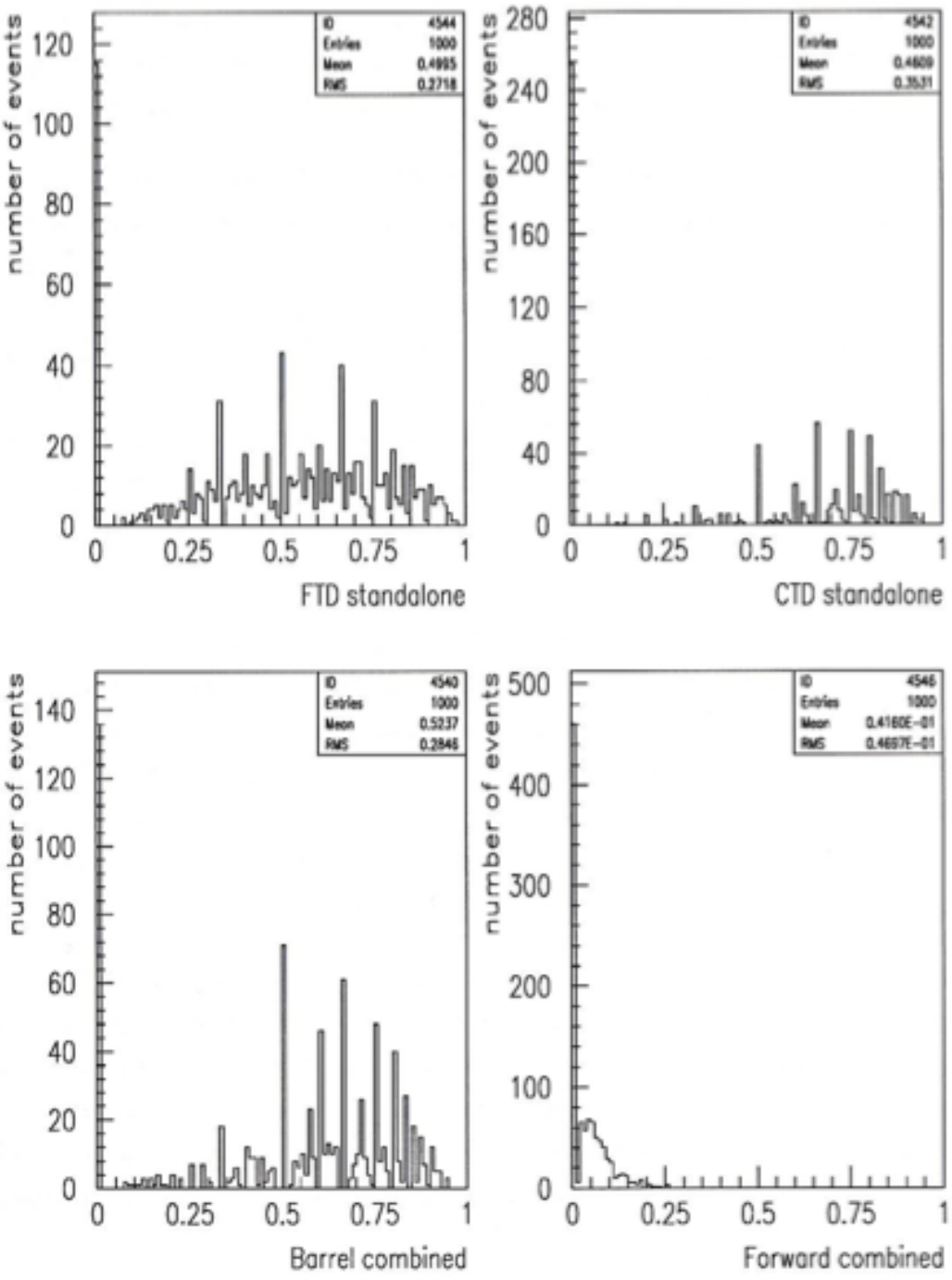

Figure 6.7: Subtrigger ratios for CC sample.

Subtrigger	Non-zero denominator
Barrel combined	23%
CTD	16%
FTD	30%
Forward combined	18%

Table 6.3: Proportion of beamgas events in zero bin with non-zero denominator for the four subtriggers.

of the need to allow for the smearing of the nominal interaction point with σ_z of $20\,\mathrm{cm}$. The electronics will allow SL3 segments in the z/r bin which would be expected from the SL1 segment to set an FBIN, or either of the adjacent bins. This means that a single SL3 segment will set 2 or 3 FBINs. However, it is only in general possible to match one of these with FTD superdiamonds, making the forward combined subtrigger ratio lower than would otherwise be the case.

A sample of single straight tracks was considered from this point of view. It was necessary to filter this sample so that only events setting a single SL1 segment remained. this was done because real particles sometimes interacted before they reached the detector resulting in confusing output. It was found for single tracks generated with $20^\circ \leq \theta \leq 30^\circ$, 72% of single SL1 segments set more than one FBIN. The important fact to remember is that this is not *per se* inimical to to good trigger efficiency. The beamgas plot shows that background events are almost never able to satisfy this stringent criterion and so the use of this subtrigger (with a lax cut) remains highly advantageous.

Two methods of combining the ratios obtained as described above t produce a final decision were investigated. Both had the starting point that any event without either SL1 segments or FTD1 diamonds was unclassifiable by the RBOX and placed into a separate 'no decision' class. The possibility of rejecting events which fail any cut is clearly unsatisfactory: even setting loose cuts resulted in a large proportion of all events being rejected by each individual subtrigger. This would permit good

beamgas rejection but only at the expense of poor CC efficiency. In preference, the idea of accepting all events which passed *any* of the subtriggers was adopted.

Simulation progressed in the expectation that a set of cuts could be defined in such a way as to enable the selection of a high proportion of good events from each plot. It was also hoped that the degree of correlation between the plots would not be high for signal events so that events in a low bin on one plot might frequently be found in a high bin in another. This would mean that overall a good efficiency might be obtained by combining all the ratios.

6.4.2 Tracking Triggers

Cut values were chosen for each of the subtriggers and optimized iteratively. It was decided to find the highest CC efficiency available in the CTD, the FTD and the RBOX while maintaining beamgas leakage at similar levels in each case to aid comparison.

The effect of making a particular cut more stringent is to reduce acceptance of both physics and background events. This effect is illustrated in figure 6.8 for CC events and in figure 6.9 for neutral current (NC) events. A perfect trigger would accept all physics and reject all beamgas and would thus reside in the top left corner of the plots. It can clearly be seen that the RBOX more closely approaches this ideal for CC events than either of the other triggers. In the case of the NC sample, the performances of the CTDFLT and the RBOX FLT are less strikingly different. The RBOX is still better at rejecting beamgas over most of the range, but the CTDFLT performs well here because it is successful in triggering on the electron.

It is interesting to note the effect of the effect of the number of tunable parameters on the shape of the distributions in the figures. The FTDFLT contains only one parameter and the figure shows therefore a smooth curve. The CTDFLT however contains two such parameters as was mentioned in section **??**. This results in the two curves seen. At the low efficiency end of the CTDFLT, the curves become close to vertical. This is because in this region of the plot, which would clearly never be used in a real situation, the cuts are very tight. This means that they are being applied in a region which contains very few beamgas events. The effect of making small

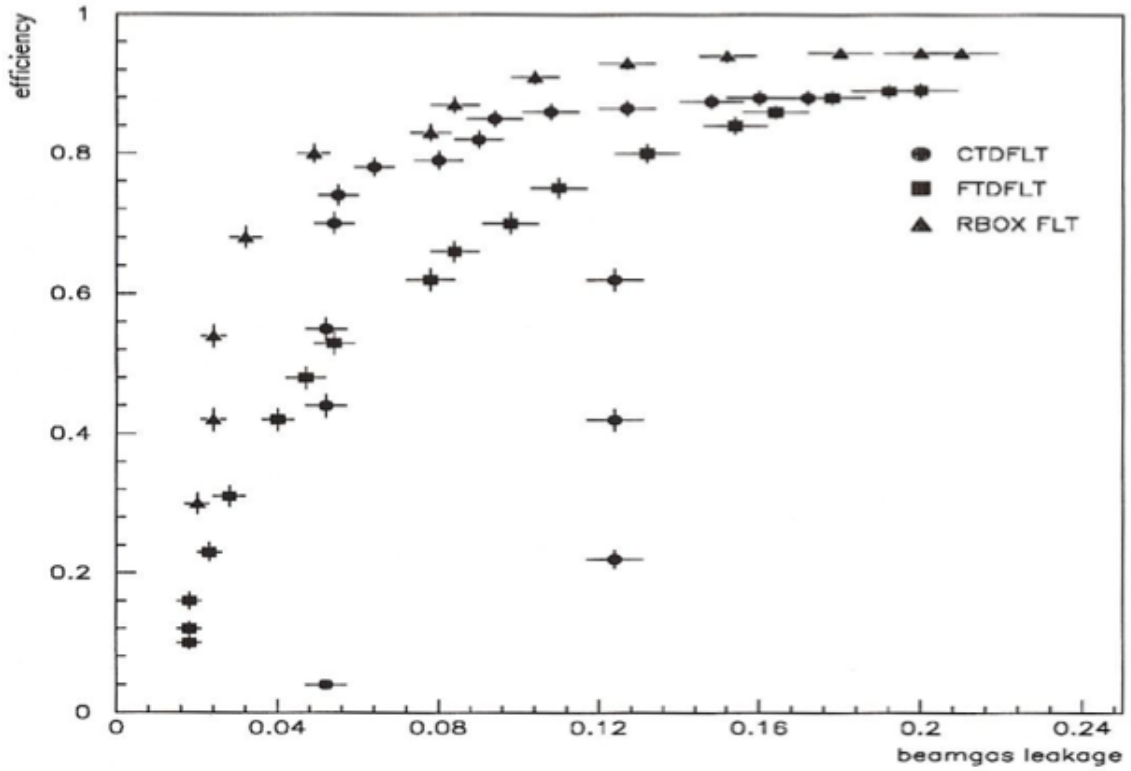

Figure 6.8: Profile of efficiency vs. leakage for CC events.

adjustments to these cuts is to alter the signal efficiency without changing the leakage. This results in the shapes seen. In the four-parameter RBOX FLT, the situation is rather complex but the shape is consistent with the usual form of efficiency vs. leakage plots. It should be recalled that in the RBOX FLT, all events passing any cut are accepted.

The values of the cuts on ratios which were chosen as representing optimal performance for the RBOX are tabulated in table 6.4. The particular cut values are justified by cross-correlation plots showing one ratio plotted against another. These are shown in figure 6.10 for signal events and in figure 6.11 for background events. In both cases lines are drawn showing the cuts.

It is important to realize that the cut values shown above for CTD and FTD subtriggers *in the RBOX* are distinct from the cut values used for the standalone triggers in the CTD and FTD which were run to allow comparison with the RBOX. The

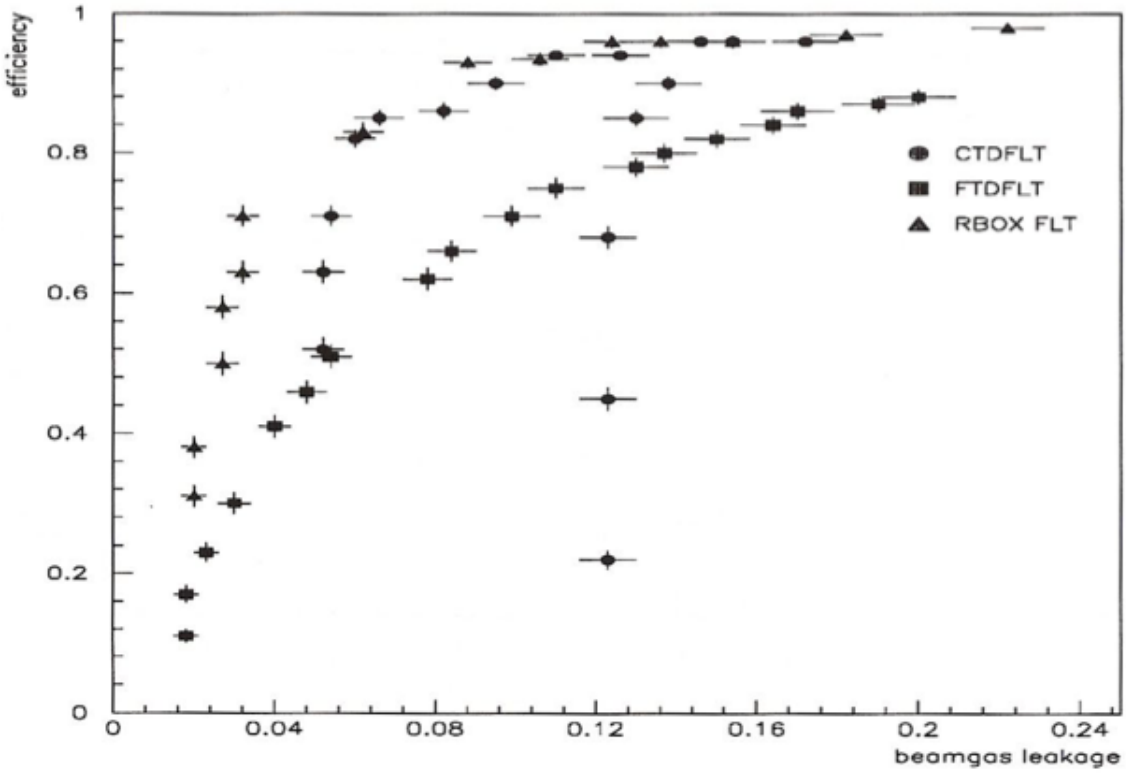

Figure 6.9: Profile of efficiency vs. leakage for NC events.

Subtrigger	**Cut value**
CTD	0.20
FTD	0.40
Barrel combined	0.10
Forward combined	0.01

Table 6.4: RBOX FLT cut values for the four subtriggers.

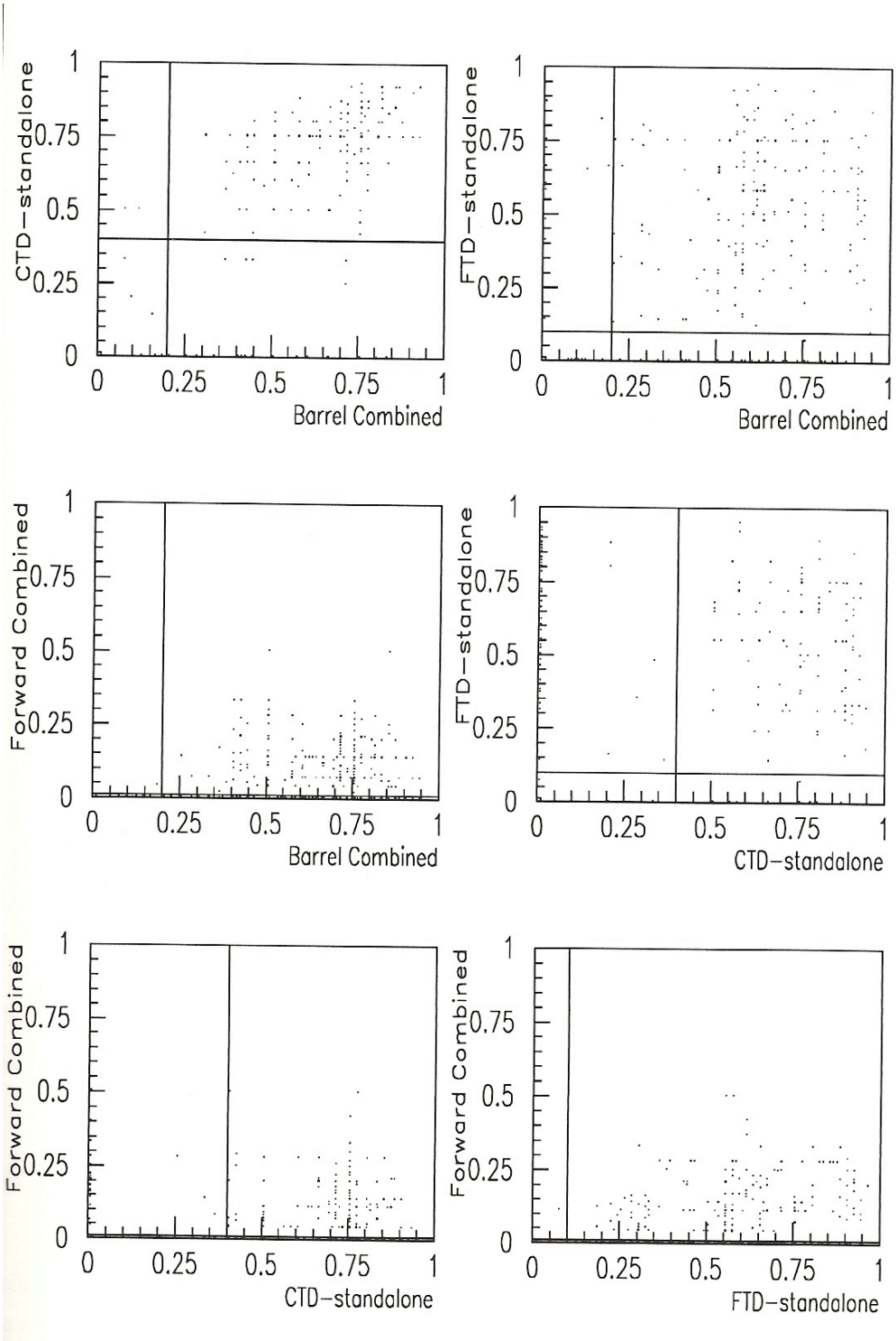

Figure 6.10: Cross-correlation plots for CC events.

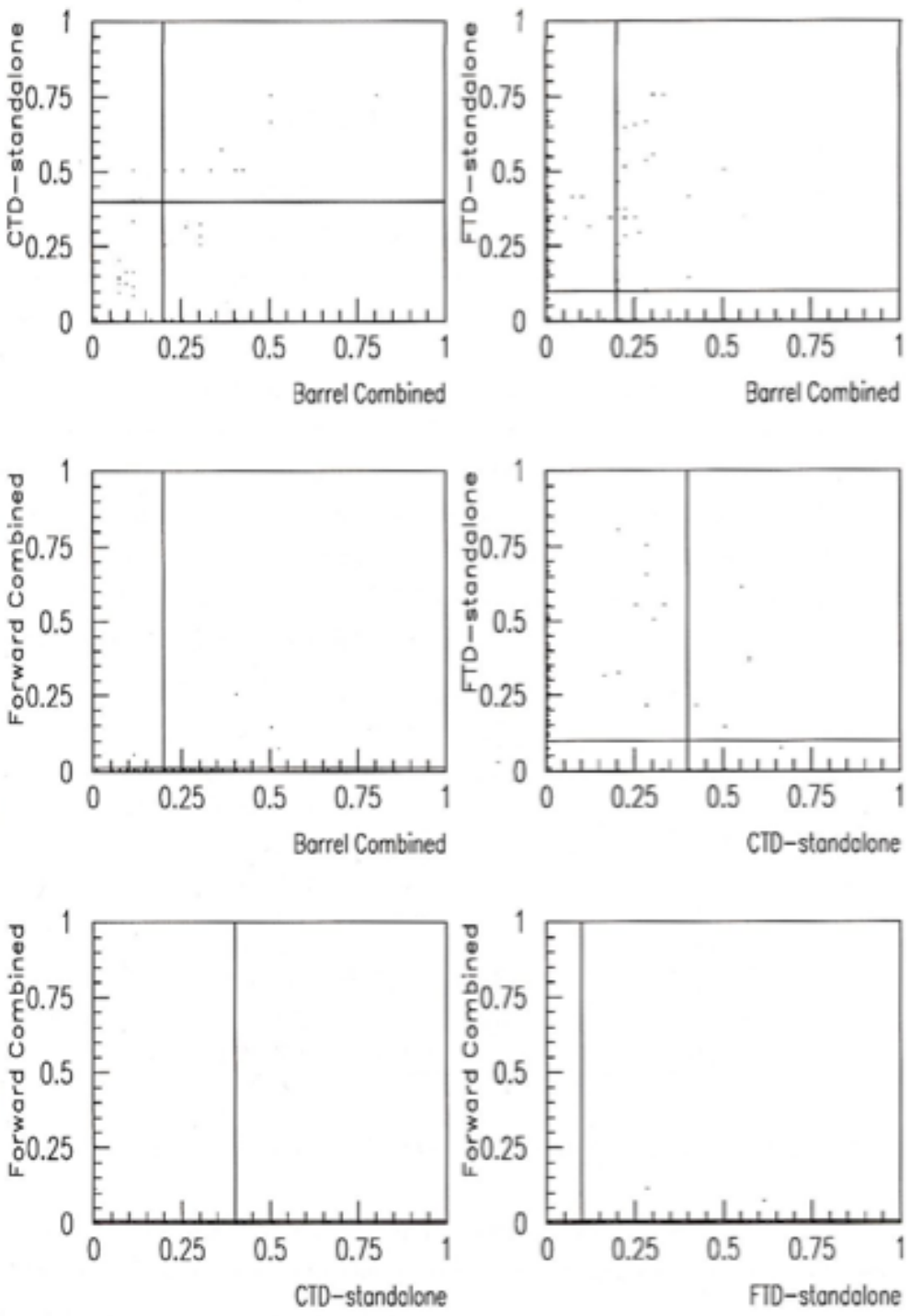

Figure 6.11: Cross-correlation plots for NC events.

standalone cuts were adjusted to produce similar levels of leakage so that efficiencies might more easily be compared. This meant that in the case of the FTDFLT, the requirement was that more than 27% of diamonds found were matched. In the CTDFLT, an event was accepted as class 2 if more than 10% of SL1 segments were matched out to SL5. Otherwise, an event was placed in the weak accept class 3 if more than 25% of sectors in SL1 which have segments also have their vertex segment bits set.

The results obtained[1] using these various cut values are tabulated below. It can be seen from table 6.5 that good CC acceptance was obtained using the RBOX. For the CTDFLT standalone results, it should be recalled that initially class 3 events will be accepted and so count as class 2 (the meaning of the classes was given in section 5.2). So in assessing the relative performances of the CTD, FTD and RBOX FLTs, the sum of CTD class 3 and class 2 events should be compared with FTD class 2 and with RBOX class 2.

Event class	**Efficiency**
Combined RBOX FLT class 2 (accept)	0.932 ± 0.008
Combined RBOX FLT class 1 (reject)	0.042 ± 0.006
Combined RBOX FLT class 0 (no decision)	0.026 ± 0.005
CTDFLT class 3 (weak accept)	0.136 ± 0.011
CTDFLT class 2 (accept)	0.747 ± 0.014
CTDFLT class 1 (reject)	0.042 ± 0.006
CTDFLT class 0 (no decision)	0.075 ± 0.008
FTDFLT class 2 (accept)	0.816 ± 0.012
FTDFLT class 1 (reject)	0.105 ± 0.010
FTDFLT class 0 (no decision)	0.079 ± 0.008

Table 6.5: Results for 1000 CC events generated with a Q^2 cut of $100\ \mathrm{GeV}^2/\mathrm{c}^2$.

[1]The error σ in the efficiency x is calculated from $\sigma = \sqrt{\frac{x(1-x)}{n}}$ where n is the number of events in the class [79].

Table 6.6 shows the results for NC events. They are similar to those obtained with the CC sample except the presence of the electron improves efficiency in the cases of the RBOX and the CTD.

Event class	**Efficiency**
Combined RBOX FLT class 2 (accept)	0.951 ± 0.007
Combined RBOX FLT class 1 (reject)	0.036 ± 0.006
Combined RBOX FLT class 0 (no decision)	0.012 ± 0.003
CTDFLT class 3 (weak accept)	0.121 ± 0.010
CTDFLT class 2 (accept)	0.829 ± 0.012
CTDFLT class 1 (reject)	0.023 ± 0.005
CTDFLT class 0 (no decision)	0.026 ± 0.005
FTDFLT class 2 (accept)	0.824 ± 0.012
FTDFLT class 1 (reject)	0.105 ± 0.010
FTDFLT class 0 (no decision)	0.070 ± 0.008

Table 6.6: Results for 1000 NC events generated with a Q^2 cut of $100\ \mathrm{GeV}^2/\mathrm{c}^2$.

There is some upper limit on the efficiencies which may be achieved. An idea of this can be gained by considering the proportion of signal events in which the trigger can be gained by considering the proportion of signal events in which the trigger identifies tracks. If no entities are found from which to construct tracks, the event cannot be triggered on. The fraction of events with either segments or superdiamonds found is 97.4% for CC events and 99.5% for NC events. In this context the performance of the RBOX trigger can be seen to be good.

Excellent results were obtained for beamgas rejection. These are shown in table 6.7. The aim of the trigger is to obtain good physics efficiency together with good beamgas rejection. The standalone results for the same sample are shown here also for purposes of comparison. It can be seen that the RBOX is on this basis able to outperform either of the standalone subtriggers, because the leakage is less than in either of the standalone cases and the previous tables showed that this is achievable in conjunction with superior physics acceptances.

Event class	Efficiency
Combined RBOX FLT class 2 (accept)	0.129 ± 0.007
Combined RBOX FLT class 1 (reject)	0.325 ± 0.010
Combined RBOX FLT class 0 (no decision)	0.546 ± 0.011
CTDFLT class 3 (weak accept)	0.108 ± 0.007
CTDFLT class 2 (accept)	0.048 ± 0.005
CTDFLT class 1 (reject)	0.140 ± 0.008
CTDFLT class 0 (no decision)	0.704 ± 0.010
FTDFLT class 2 (accept)	0.138 ± 0.008
FTDFLT class 1 (reject)	0.325 ± 0.010
FTDFLT class 0 (no decision)	0.560 ± 0.011

Table 6.7: Results for 2000 FRITIOF beamgas events generated from $z = -1900\,\mathrm{cm}$ to $z = +100\,\mathrm{cm}$.

In particular, the FTD standalone subtrigger cannot achieve very high CC acceptance within a tight beamgas leakage constraint. In fact, an efficiency of 82% is obtainable with leakage of 14%. Similarly, the standard CTDFLT cuts result in an efficiency of 88% with leakage of 16%. The RBOX, however, is able to achieve 93% CC acceptance with less beamgas leakage than in either of the standalone cases.

The origin distribution along the beamline for accepted events can be seen in figure 6.12.

6.4.3 Beamgas Background

6.4.3.1 Comparison of Different Generators

To gain an appreciation of the amount of variation that may be produced in the detector by the use of different background generators, samples of 2000 events from FRITIOF and UA5 were passed through identical versions of ZEUSGeant and ZGANA. In order not to duplicate the results presented in the previous section and to focus attention on the differences produced only by the generators, a non-standard distribu-

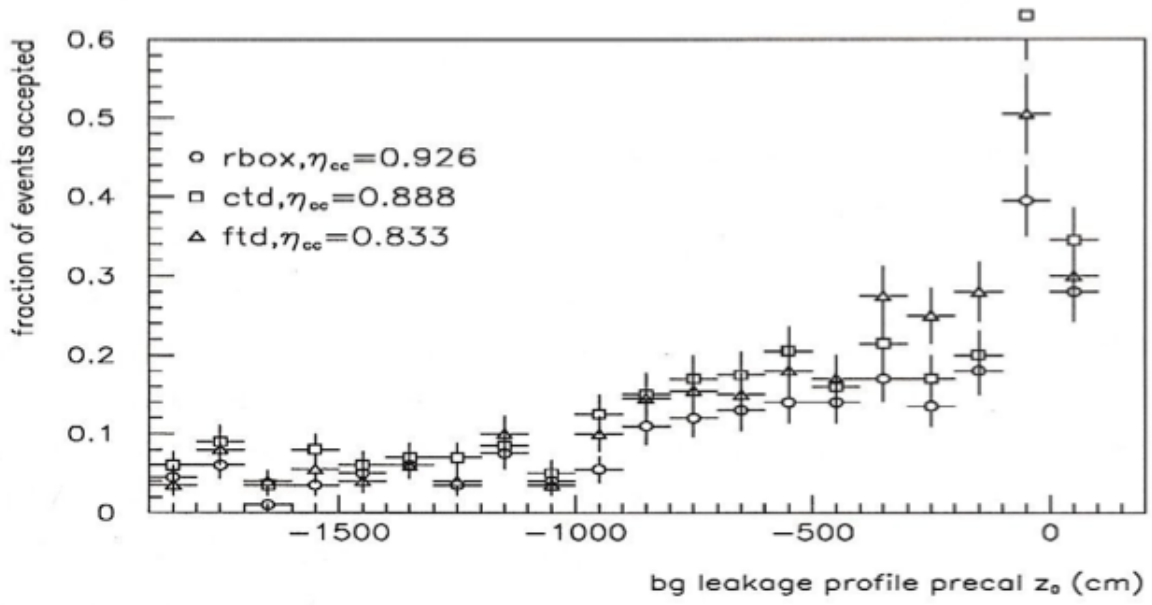

Figure 6.12: Beamgas leakage vertex profile along the beamline. CC efficiencies are also noted here, using the symbol η_{cc}.

tion along the beamline was used for these two samples. In fact, they were generated homogeneously along the section with $-19\,\mathrm{m} \leq \mathrm{z} \leq -9\,\mathrm{m}$. The results obtained are shown in table 6.8 below.

It can be seen that leakage rates are compatible for both generators while significant differences emerged in the balance of the remainder between rejected and unclassified events. In particular, this study indicates that results obtained with different generators should be comparable to within the 5% level. It has been shown [80] that FRITIOF has both a harder transverse energy spectrum and a higher multiplicity than the UA5 generator. These are the reasons for the differences found here because both factors mean that tracking detectors have a higher probability of correctly identifying the upstream vertex.

6.4.3.2 Reasons for Beamgas Leakage

it is important to know the causes of beamgas leakage in the tracking FLT. Only UA5 events were considered here for the sake of consistency. It was a plausible hypothesis

Event class	FRITIOF	UA5
CTD 3 (weak accept)	0.043 ± 0.005	0.040 ± 0.004
CTD 2 (accept)	0.017 ± 0.003	0.017 ± 0.003
CTD 1 (reject)	0.081 ± 0.006	0.070 ± 0.006
CTD 0 (no decision)	0.858 ± 0.008	0.874 ± 0.007
FTD 2 (accept)	0.052 ± 0.005	0.058 ± 0.005
FTD 1 (reject)	0.202 ± 0.009	0.151 ± 0.008
FTD 0 (no decision)	0.746 ± 0.010	0.791 ± 0.009
RBOX 2 (accept)	0.044 ± 0.005	0.049 ± 0.005
RBOX 1 (reject)	0.226 ± 0.010	0.166 ± 0.005
RBOX 0 (no decision)	0.729 ± 0.010	0.786 ± 0.009

Table 6.8: Event classifications for the full FLT simulations for events from two different beamgas generators.

that leakage was due to the events having primary or secondary vertices[1] near the interaction region. To investigate this, plots were prepared showing the numbers of vertices within a certain distance in z of the interaction point for both accepted and rejected events from a total sample of 6000. These ranges were chosen to be $-250\,\mathrm{cm} \leq \mathrm{z} \leq +250\,\mathrm{cm}$. The first corresponds roughly to the size of the CTD and the second is the same as the σ_z of the interaction region.

The results for numbers of vertices are shown in four plots, one for each range in z for both accepted and rejected events. On the plots, the abbreviation 'ir' is used to denote 'interaction region' for the wide range in z and 'ip' to denote 'interaction point' for the narrower range. It can be seen from figure 6.13 that no accepted event is without a vertex in the CTD region. In contrast, for the rejected events the zero bin is by far the largest while there is a tail out to higher numbers of vertices. The means of the two distributions show that a rejected event is more likely to have few vertices in the CTD region.

[1]Vertex information was simply taken from Geant and denotes the coordinate origin of Geant tracks, not all of which will necessarily be observed in the detector.

The figure also shows that a substantial proportion (63%) of accepted events actually have vertices very close to the nominal interaction point, whereas this is true for only around 12% of rejected events. The remaining accepted events are highly active ones causing many hits[1] in the detector and resulting in false correlations. This can be seen in the plots in figure 6.14 which show distributions of hit multiplicity for all beamgas events and those which were accepted and rejected by the CTDFLT. For comparison, the distribution for all CC events is shown. It can be seen that the mean hit multiplicity for rejected beamgas events is 0.65 of the mean for all events while this average ratio is 5.43 for accepted events.

The properties of the track momenta may also shed some light on the reasons for beamgas leakage. The plots in figure 6.15 show the transverse and z-momenta for Monte Carlo tracks in all events and those which were accepted and rejected. It can be seen from considering the means of the distributions that rejected events tend to have lower values of both while accepted events tend to have higher than average momenta.

In summary, it can be seen that the properties of an accepted beamgas event as opposed to an 'average' beamgas event are: very high hit multiplicities, large numbers of tracks originating from near the interaction region, and comparatively higher track transverse and longitudinal momentum. The striking difference in hit multiplicities means that the mechanism for acceptance of beamgas is primarily false correlation: there are simply so many track segments found that many of them must match up. Of secondary importance is the presence of tracks originating from the interaction region which should clearly be perceived as good tracks by the trigger. Since the sample was generated with $-19m \leq z \leq +1m$ this must be due to secondary interactions: particles from upstream beamgas events travel to the interaction region and intereact again with a machine element.

[1] FOOTNOTE

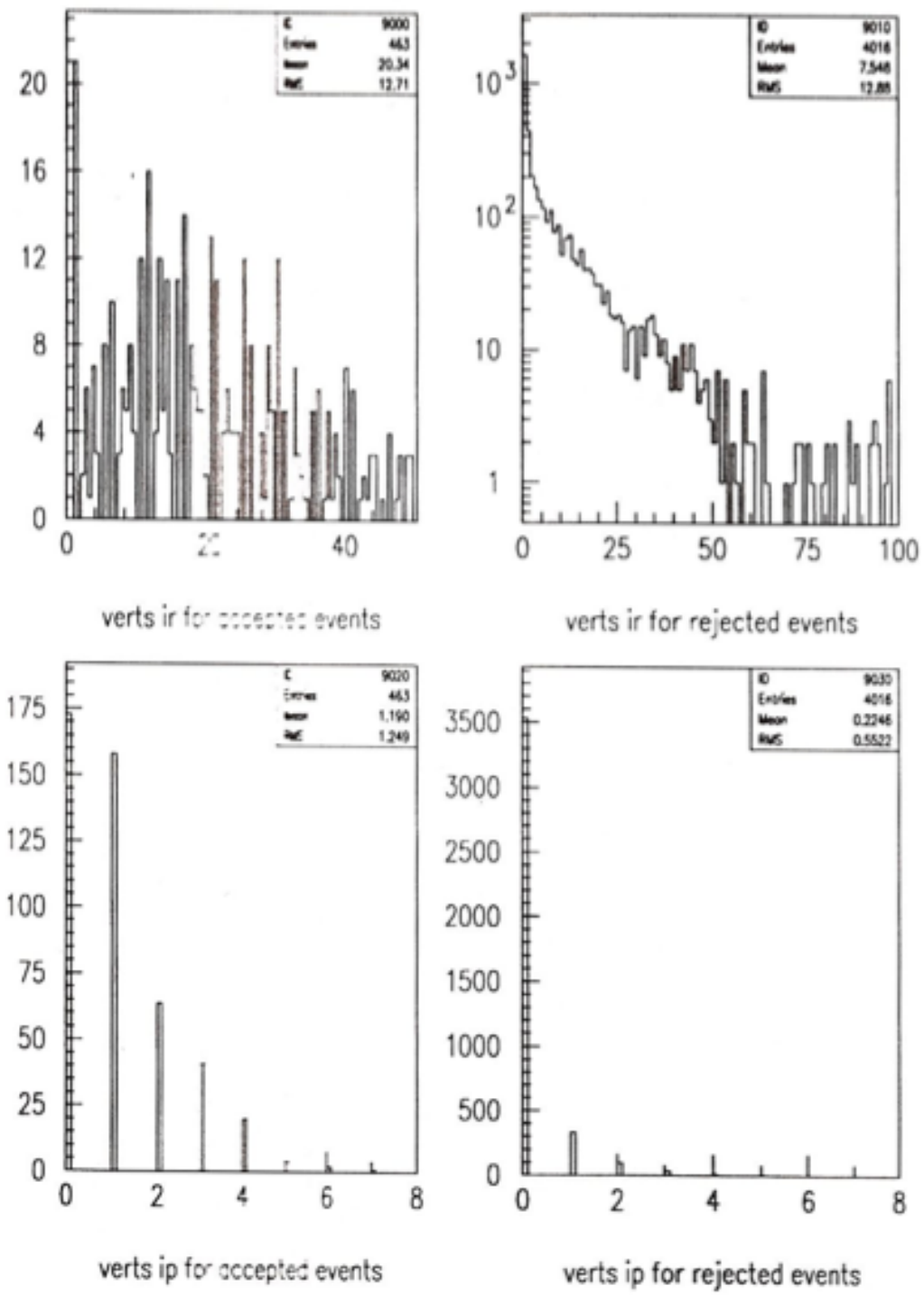

Figure 6.13: Number of track vertices per event for narrow and wide ranges around the interaction point by event classification.

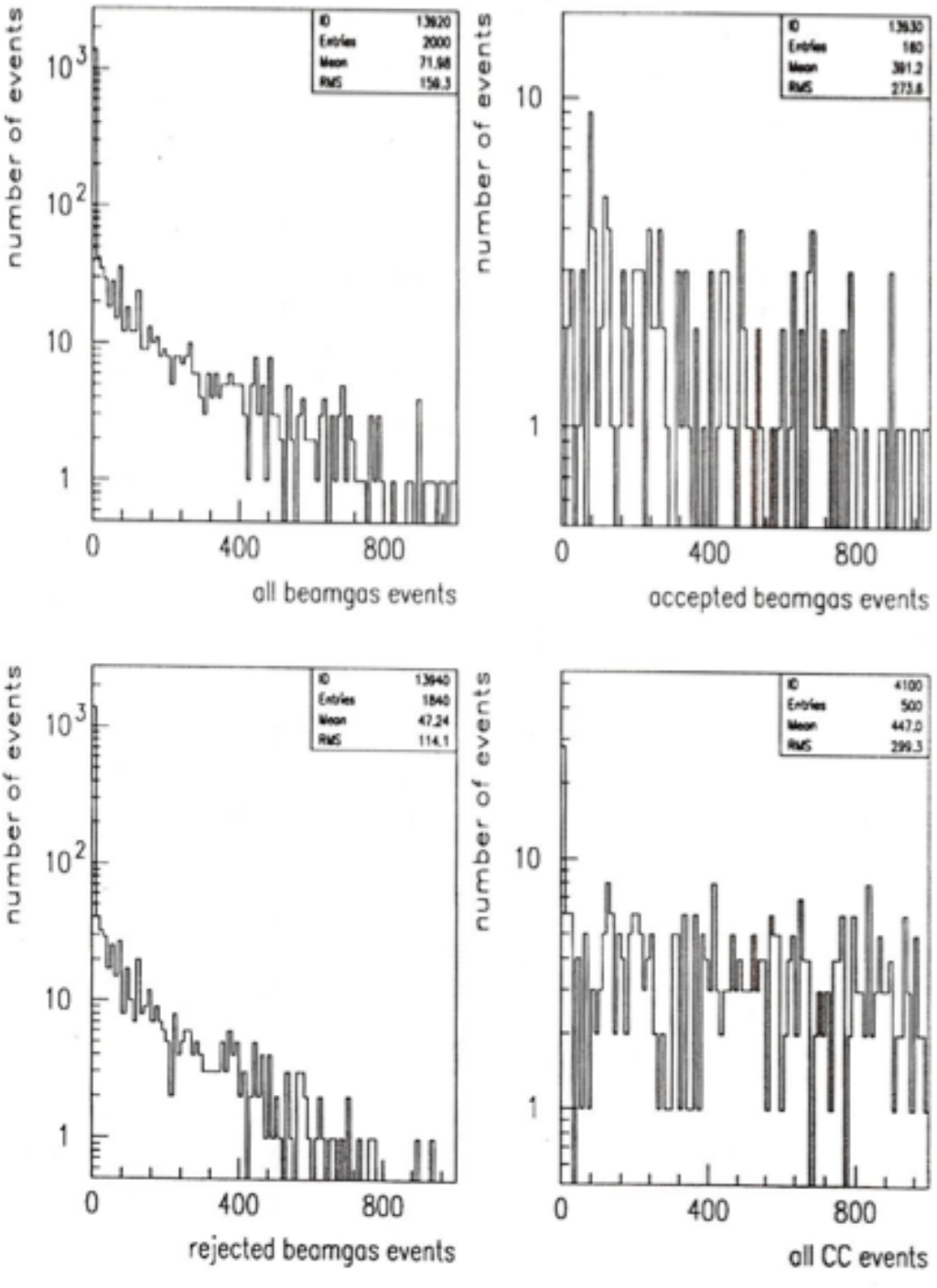

Figure 6.14: Hit multiplicity distributions by event class.

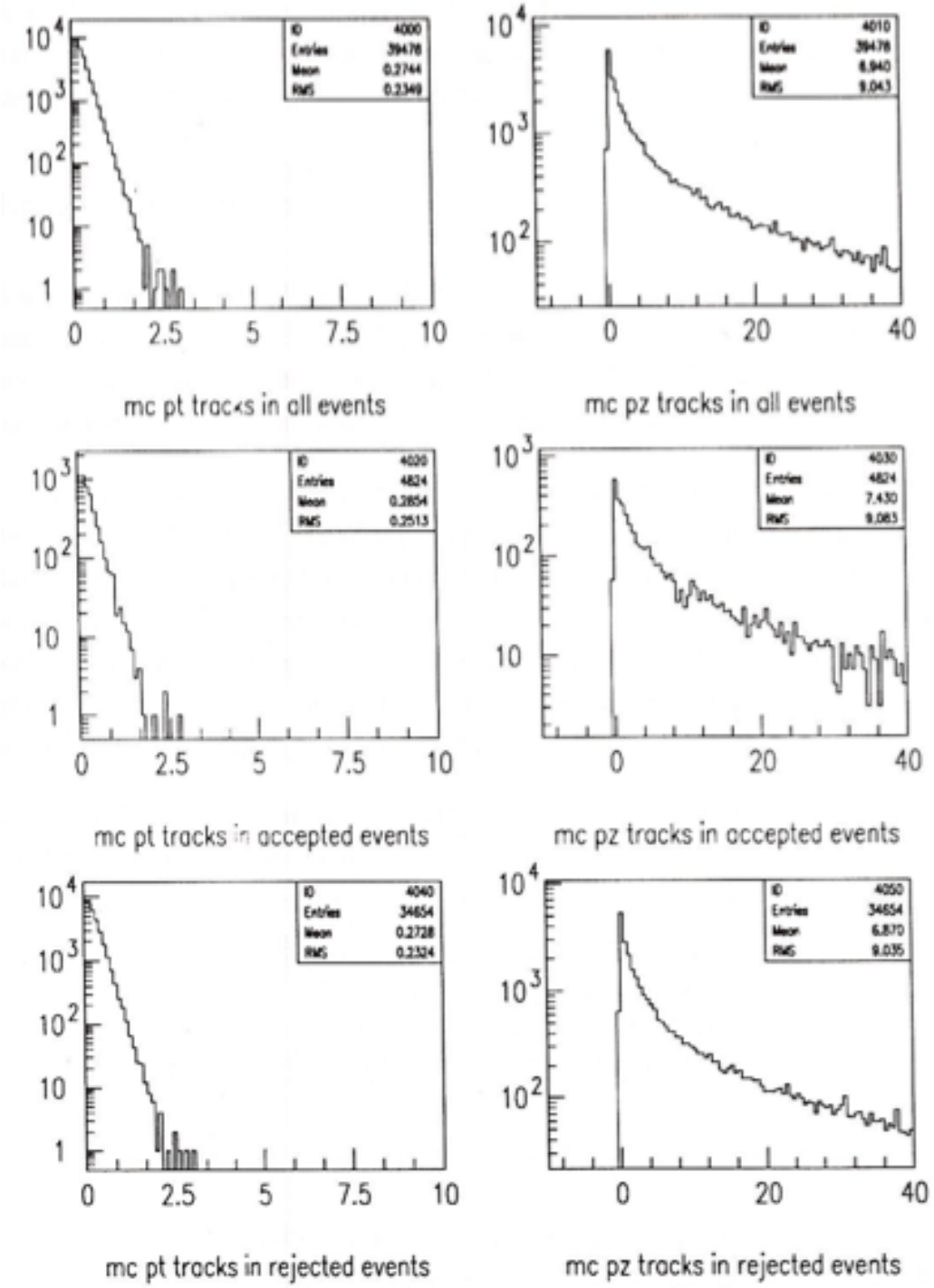

Figure 6.15: Transverse and longitudinal momenta of tracks by event class for beam-gas.

6.4.4 Calorimetry

It was decided to extend this study by looking at the effect of calorimeter information. This is cearly not something that is possible in the RBOX but should give an indication of what might be achieved in the GFLTB which receives data from most components including the RBOX and the calorimeters.

The effect of transverse energy cuts was investigated. The values of the cuts used were different for each class of event processed by the tracking trigger. These were fixed empirically by studying the energy distributions of events in the different classes and adjusting the cuts accordingly. Clearly, there are many more sophisticated methods of using information from the calorimeters but the concern here is only to provide a simple test to ensure that improvements made in the RBOX are not lost or irrelevant after input from the calorimeters.

The values chosen for the travsverse energy cuts are shown in table 6.9 for the CTD and table 6.10 for the RBOX.

Class	**Cut**
3 (weak accept)	E_T >10.5 GeV
2 (accept)	E_T >8.5 GeV
1 (reject)	E_T >22.5 GeV
0 (no decision)	E_T >13.5 GeV

Table 6.9: Transverse energy cuts chosen for the CTD.

Class	**Cut**
2 (accept)	E_T >11 GeV
1 (reject)	E_T >23 GeV
0 (no decision)	E_T>15 GeV

Table 6.10: Transverse energy cuts chosen for the RBOX.

These figures are quite acceptable intuitively as far as their variation with event classes is concerned. For events accepted by the tracking trigger only modest transverse energy deposition is required. This does not harm physics acceptance but provides great discrimination against beamgas. However, as the tracking triggers become more sertain that the event did not come from the vertex, higher deposiiotns are required for the calorimeters to override the tracking triggers.

It was found that using calorimeter data, the RBOX achieved a CC efficiency of 98.5%, while the CTD achieved an efficiency of 99.2%. This means that the leakage figures for both may be compared since the efficiencies are the same within the statistics. figure 6.16 shows that the RBOX has consistently better beamgas rejection than the CTDFLT after the inclusion of calorimeter data. Integrating over the range of the plot, a total of 99 events (of 2000) were accepted by the CTD in combination with the CAL as opposed to only 47 by the RBOX and CAL. For a leakage rate of $1\mathrm{kHzm}^{-1}$ this corresponds to $470\mathrm{Hz}$ and $990\mathrm{Hz}$ respectively at the FLT. The importance of the RBOX may readily be seen bearing in mind the $1\mathrm{kHz}$ maximum rate in the GFLTB.

The fact that the cuts are in each case slightly higher for the RBOX than for the CTD standalone may be explained in the light of these results. Since efficiency is so high in both cases that it cannot practicably be improved upon, attention focusses on improving rejection of background. Since the quality of information available to the RBOX is of higher quality, it is possible to impose stricter transverse energy cuts in the RBOX, thus rejecting more background, without affecting CC efficiency.

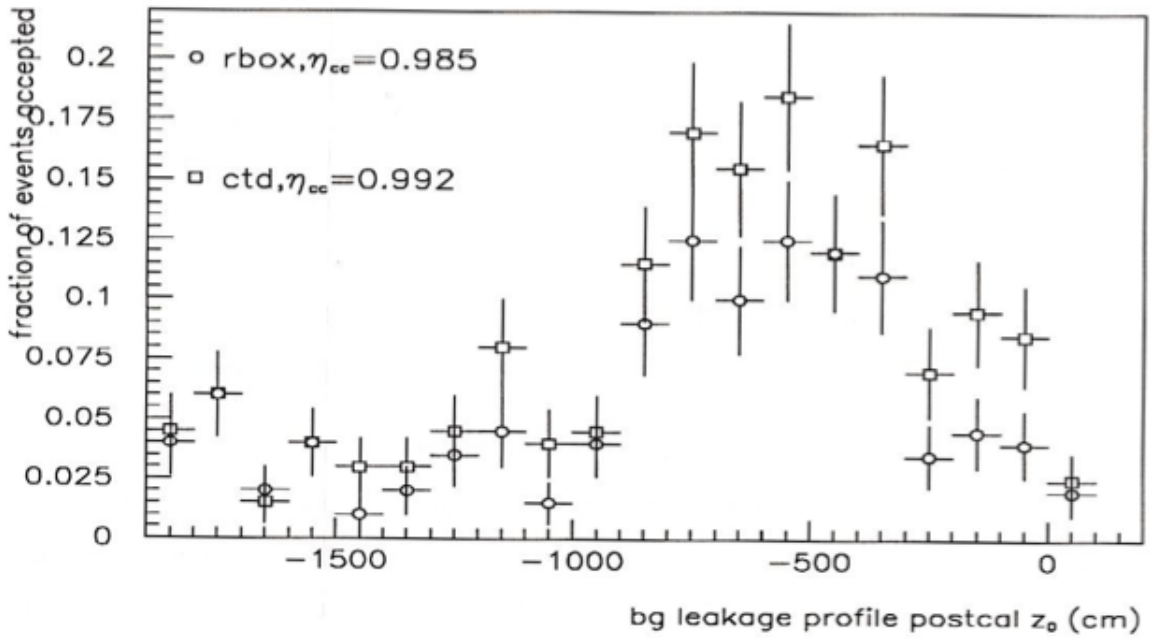

Figure 6.16: Beamgas leakage vertex profile along the beamline after calorimeter transverse energy cuts. CC efficiencies are also noted here, using the symbol η_{cc}

6.5 Hardware Design of the RBOX

The RBOX processing is divided up into modules both functionally and geometrically, as shown in figure 6.17. The RBOX will have two crates. Crate one contains eight hit counting modules (HCM) and one final decision module (FDM). Crate two contains eight overlap track modules (OTM) and a module to count the FTD superdiamonds.

The HCMs receive hit information (flag bits) from up to five ϕ sectors. This data comes from the CTD sector processors and the OTMs which deal with the CTD/FTD overlap. There is a one-to-one correspondence in ϕ between the OTMs and HCMs. The modules and their interconnections are shown in figure 6.18.

The FDM will use internal bitmaps which will have granularity in θ, ϕ of 4×32. This corresponds in ϕ to the sector processors' subdivision. In θ, two regions cover the forward direction, and the remaining two cover the barrel and rear directions. Input to the FDM consists of the total number of sectors with tracks found in each of four θ regions; these regions may be the same as the four listed above or may be combinations of them [81].

The diamond counting module will deliver to the FDM the value of the ratio of matched to unmatched diamonds. The FDM is responsible for determining the values of the ratios for the other three subtriggers described in this chapter. It will then produce a final decision from all of the ratios. The processing to do this will be based on Xilinx chips.

The output from the FDM to the GFLTB is carried by 16-bit cables. One will be sufficient to indicate the event class and the sector hit multiplicity. This corresponds to the processes "Count hit sectors" and "Classify event" of the functional subdivision. Further cables will carry the bitmap of tracks found.

The OTMs use a different angular granularity reflecting the requirement to output track angular distributions for calorimeter matching. The process "Find overlap tracks" is divided into eight ϕ wedges, one wedge per OTM. These modules provide the 8×8

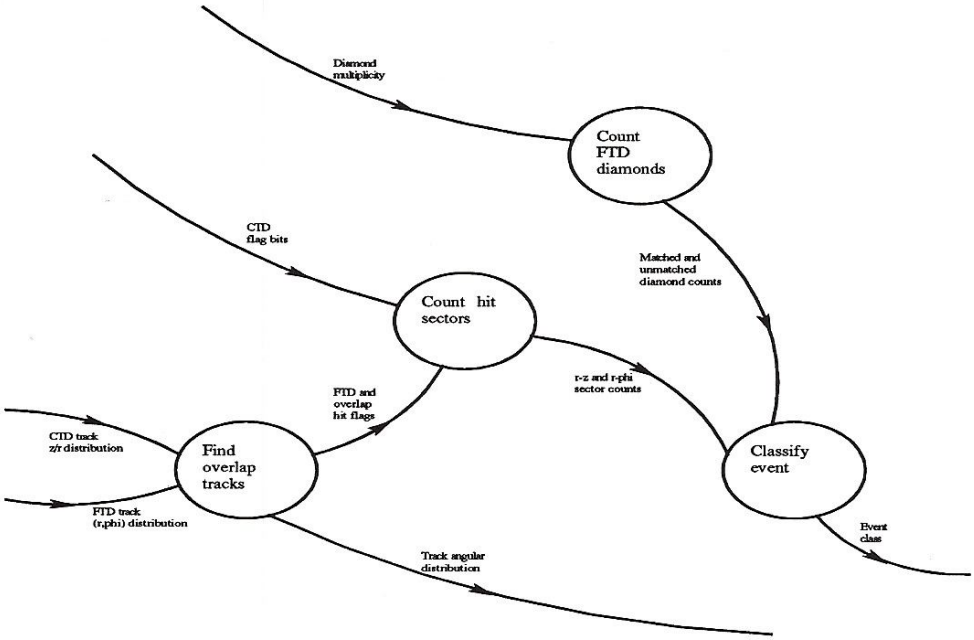

Figure 6.17: Regional box functional subdivision.

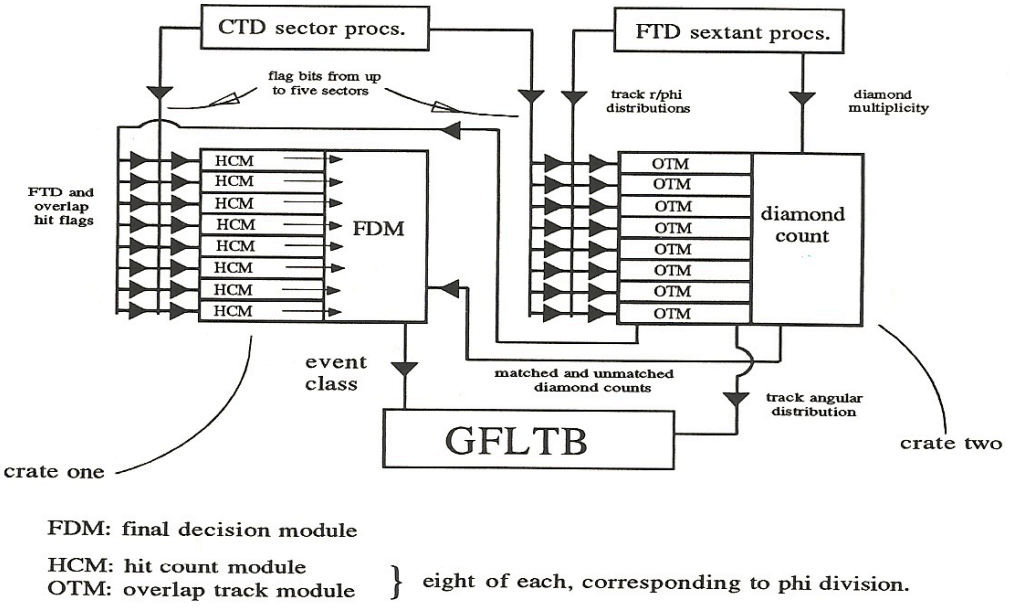

Figure 6.18: Regional box hardware scheme.

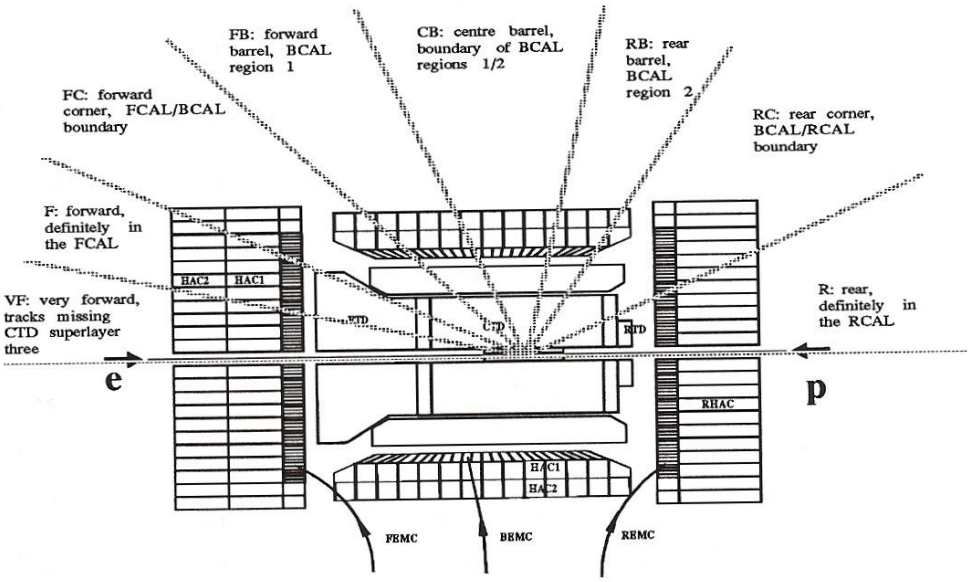

Figure 6.19: Subdivision in θ of RBOX bitmap to GFLTB.

bitmap output to the GFLTB as well as the information to the HCMs. The θ division corresponds to the calorimeter division and is shown in figure 6.19.

Chapter 7
Investigation of Kinematic Dependence of CTDFLT Efficiency

7.1 Introduction

The motivation behind the work described in this chapter was the desire to know to high precision the CTDFLT efficiency across the whole of the accessible phase space. This is important for measurement of cross-sections as mentioned in the previous chapter.

The naïve approach of simply generating large numbers of events in kinematic bins is not a suitable one since the constraints of available computer resources mean that the requisite precision cannot be obtained over all phase-space. For this reason, a method of simplifying the problem was searched for. For CC events, it is inherently plausible that the efficiency of the CTDFLT depends only on the polar angle of the current jet θ_{jet}. This hypothesis was shown to be consistent with the data by generating a large sample of events in small regions of phase space with fixed θ_{jet}.

The results for each angle were combined to produce high-precision efficiency data. These were then used to plot a map in $x - Q^2$ space by assuming the same efficiency for all points in the phase space with the same jet angle.

The method was also investigated with respect to NC events. As would be expected however, it was found to be unsatisfactory due to the scattered electron which plays an important part in triggering these events.

7.1.1 Special Jacquet-Blondel Kinematics

It is possible to manipulate the usual kinematic equations (see equation 1.26 in section 1.2.2.3) so that the θ_{jet} dependency becomes more explicit; in particular using half angle formulae and setting $\mathrm{E_e} = 30\mathrm{GeV}$ gives equation 7.1:

$$Q^2 = \frac{3600\, y^2}{(1-y)\, \tan^2 \frac{\theta_{jet}}{2}}\, GeV^2/c^2 \tag{7.1}$$

So for a fixed jet angle, various different combinations of values of x and Q^2 are available for a given y. Contours of fixed y are shown in the $x - \theta_{jet}$ plane in figure 7.1 and for the $Q^2 - \theta_{jet}$ plane in figure 7.2.

We may define a SL polar angle such that a track from the nominal interaction point at this angle will leave the sensitive volume of the CTD at a position on the endplate midway between where the two central wires are attached. The minimum angles for the instrumental SLs are $11.6°$, $18.9°$, $25.4°$ for SL1, SL3 and SL5 respectively. It is obvious that there will be no information from the CTDFLT concerning tracks with angles smaller than $11.6°$ (or greater than $168.4°$). In fact, there will be some spread of tracks around the nominal jet angle so that some proportion of events have no tracks within the sensitive volume of the CTD. Clearly one expects this proportion to increase as the nominal jet angle is changed such that the tracks are expected to be closer to the beampipe.

7.2 Event Generation

A low-statistics pass across the whole of the angular range was made. Fifty events were generated in angular bins of two degrees. The information needed to produce bins in x and Q^2 corresponding to the required angular range is shown graphically in figure 7.1 and figure 7.2.

The events were generated with $10° < \theta_{jet} < 90°$. It was not necessary to generate

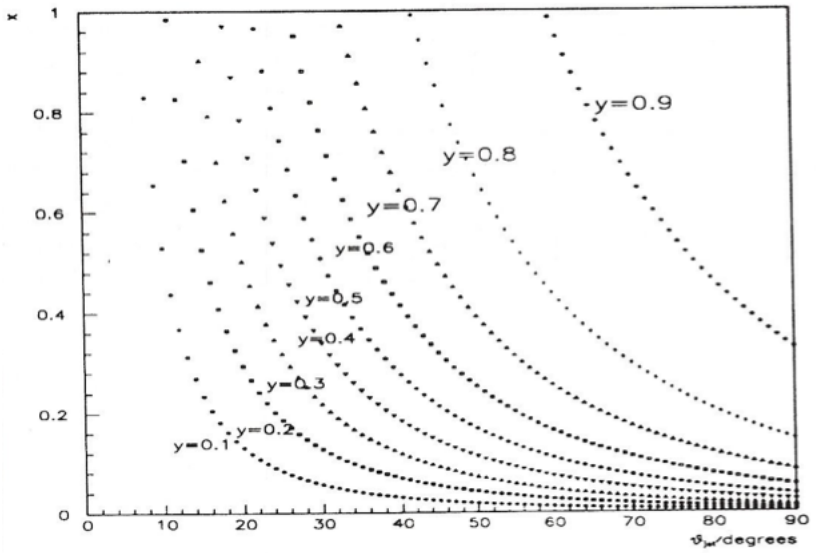

Figure 7.1: Contours of fixed y in the $x - \theta_{jet}$ plane.

any events with jet angles of larger than 90° because symmetry means that $\epsilon(\theta - 90^\circ) \equiv \epsilon(\theta)$. Below 10° there is not expected to be any activity in the detector. A similar sample was generated for NC events.

A selected set of five angles were chosen for high statistics runs. These angles were 13°, 23°, 33°, 43° and 63°. These were chosen with reference to the superlayer polar angles mentioned above. They correspond to the cases in which one expects the jet to pass through the one or two instrumental SLs for the two lowest angles and all three instrumented SLs for the remaining three angles.

Angular bins with a a range of one degree either side of the nominal value were defined for the low-statistics run. To measure the variation with respect to y from 0.1 to 0.9 were defined. Approximately one thousand events were generated in each bin so that in total 36250 events were used in this study. The CTDFLT simulation was run to find the efficiency.

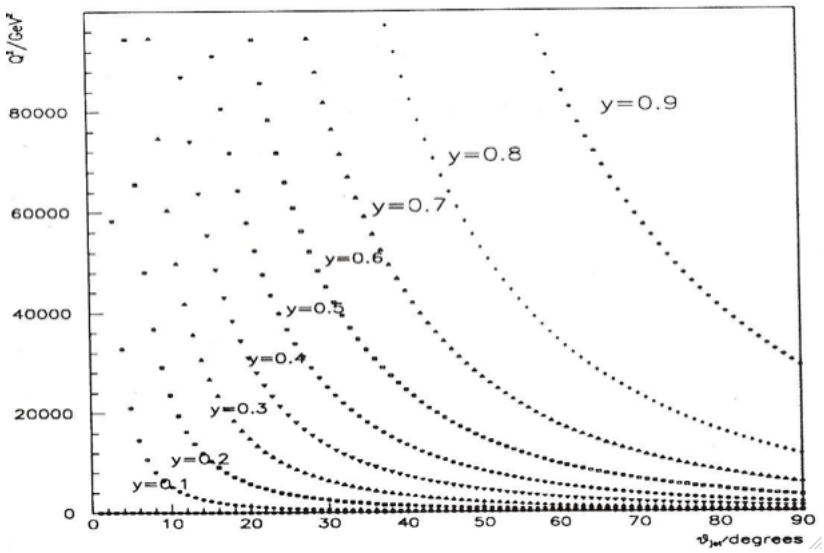

Figure 7.2: Contours of fixed y in the $Q^2 - \theta_{jet}$ plane.

7.3 Results

The results for $\theta_{jet} = 63^\circ$ are shown in table 7.1, for $\theta_{jet} = 43^\circ$ in table 7.2, for $\theta_{jet} = 33^\circ$ in table 7.3, for $\theta_{jet} = 23^\circ$ in table 7.4 and for $\theta_{jet} = 13^\circ$ in table 7.5.

y	x-range	Q^2-range	efficiency	error
0.1	$0.0103 \rightarrow 0.0112$	$102 \rightarrow 111$	0.991	0.003
0.2	$0.0234 \rightarrow 0.0253$	$461 \rightarrow 499$	0.997	0.002
0.3	$0.0401 \rightarrow 0.0433$	$1185 \rightarrow 1282$	0.999	0.001
0.4	$0.0623 \rightarrow 0.0674$	$2459 \rightarrow 2659$	1.000	0.000
0.5	$0.0935 \rightarrow 0.1011$	$4610 \rightarrow 4986$	1.000	0.000
0.6	$0.1403 \rightarrow 0.1517$	$8298 \rightarrow 8974$	1.000	0.000
0.7	$0.2182 \rightarrow 0.2360$	$15059 \rightarrow 16287$	0.999	0.000
0.8	$0.3740 \rightarrow 0.4045$	$29504 \rightarrow 31908$	1.000	0.000
0.9	$0.8416 \rightarrow 0.9102$	$74681 \rightarrow 80768$	1.000	0.000

Table 7.1: CTDFLT efficiencies in the kinematic bins for $\theta_{jet} = 63^\circ \pm 1^\circ$.

y	x-range	Q^2-range	efficiency	error
0.1	$0.0249 \rightarrow 0.0275$	$245 \rightarrow 271$	0.994	0.002
0.2	$0.0560 \rightarrow 0.0619$	$1103 \rightarrow 1222$	0.997	0.001
0.3	$0.0959 \rightarrow 0.1062$	$2835 \rightarrow 3141$	1.000	0.000
0.4	$0.1491 \rightarrow 0.1652$	$5881 \rightarrow 6515$	1.000	0.000
0.5	$0.2237 \rightarrow 0.2478$	$11027 \rightarrow 12216$	0.997	0.002
0.6	$0.3355 \rightarrow 0.3717$	$19848 \rightarrow 21988$	1.000	0.000
0.7	$0.5219 \rightarrow 0.5782$	$36021 \rightarrow 39905$	0.998	0.001
0.8	$0.8947 \rightarrow 0.9912$	$70572 \rightarrow 78180$	0.998	0.001

Table 7.2: CTDFLT efficiencies in the kinematic bins for $\theta_{jet} = 43^\circ \pm 1^\circ$.

y	x-range	Q^2-range	efficiency	error
0.1	$0.0434 \to 0.0493$	$428 \to 486$	0.979	0.005
0.2	$0.0977 \to 0.1110$	$1926 \to 2189$	0.989	0.003
0.3	$0.1674 \to 0.1903$	$4952 \to 5629$	0.986	0.004
0.4	$0.2604 \to 0.2960$	$10271 \to 11676$	0.988	0.003
0.5	$0.3906 \to 0.4441$	$19257 \to 21892$	0.986	0.004
0.6	$0.5859 \to 0.6661$	$34663 \to 39405$	0.993	0.003

Table 7.3: CTDFLT efficiencies in the kinematic bins for $\theta_{jet} = 33^\circ \pm 1^\circ$.

y	x-range	Q^2-range	efficiency	error
0.1	$0.0898 \to 0.1074$	$885 \to 1059$	0.941	0.007
0.2	$0.2020 \to 0.2416$	$3984 \to 4764$	0.940	0.008
0.3	$0.3463 \to 0.4142$	$10245 \to 12250$	0.948	0.007
0.4	$0.5388 \to 0.6442$	$21248 \to 25408$	0.950	0.007
0.5	$0.8082 \to 0.9664$	$39840 \to 47640$	0.952	0.007

Table 7.4: CTDFLT efficiencies in the kinematic bins for $\theta_{jet} = 23^\circ \pm 1^\circ$.

y	x-range	Q^2-range	efficiency	error
0.05	$0.1275 \to 0.1740$	$628 \to 858$	0.804	0.012
0.10	$0.2691 \to 0.3672$	$2653 \to 3621$	0.837	0.012
0.15	$0.4274 \to 0.5833$	$6321 \to 8626$	0.858	0.011
0.20	$0.6055 \to 0.8263$	$11939 \to 16294$	0.840	0.012

Table 7.5: CTDFLT efficiencies in the kinematic bins for $\theta_{jet} = 13^\circ \pm 1^\circ$.

7.4 Discussion

figure 7.3 shows that the results are consistent with the hypothesis that there is a smooth dependence of efficiency on jet angle. From the numbers in the tables it can be seen that efficiency is constant for a given angle independent of all other kinematic variables. Also the expected deterioration in efficiency is seen as the jet angle becomes closer to the beamline.

For NC events however, figure 7.4 shows that the pattern does not show the same simple dependency on jet angle only. This is due to the presence of the scattered electron. It is unsafe therefore to attempt to proceed further with the method for this type of event.

Returning to the CC sample, it is now plausible to combine the various tables of results at the same jet angles to produce high-precision results. Since the results represent statistically independent measurements of the same quantity, they may be combined by taking the mean and dividing the error by $\sqrt{n}$ where n is the number of entries in the relevant table. This yields the figures in table 7.6.

Angle	**CTDFLT efficiency**	**error**
63	0.9984	0.0003
43	0.9980	0.0004
33	0.9865	0.0015
23	0.9461	0.0033
13	0.8347	0.0058

Table 7.6: Final combined figures for CTDFLT efficiency.

These figures may be used to generate contours of constant trigger efficiency in the $x - Q^2$ plane, remembering that symmetry allows the same efficiencies to be plotted for $180^\circ - \theta$ also. This is shown in figure 7.5.

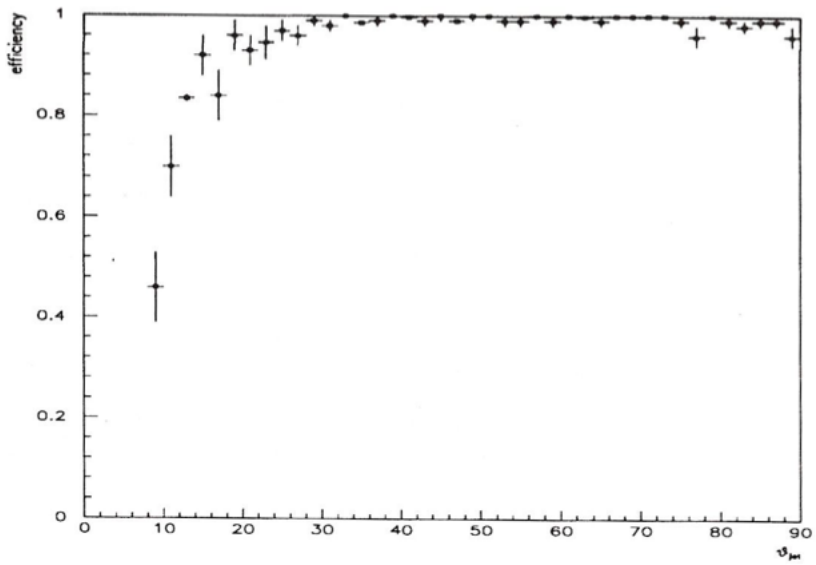

Figure 7.3: Low statistics full angle pass for CC events.

7.5 Conclusions

It has been shown that CTDFLT CC efficiency is dependent on θ_{jet} only. Precise knowledge of the expected efficiency may now be obtained over a large part of the accessible phase space by deducing the jet angle from the kinematics of a given event if that event lies on or near one of the angles studied with high statistics. Otherwise, an interpolation may be made.

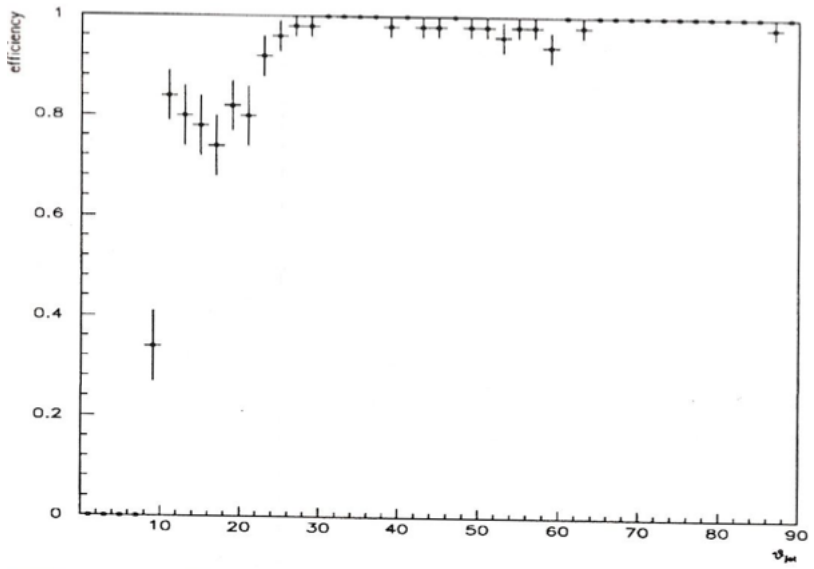

Figure 7.4: Low statistics full angle pass for NC events.

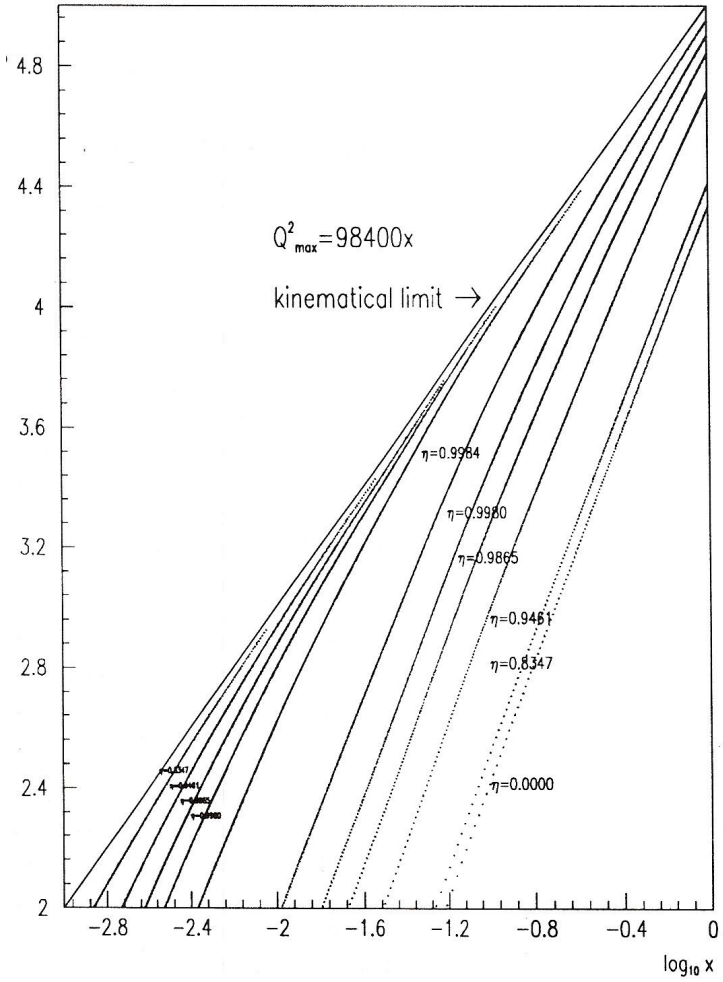

Figure 7.5: Efficiency for CC events.

Chapter 8
Heavy-Flavour Events in the Regional First Level Trigger

8.1 Introduction

Prior to machine turn-on, uncertainties about the details of many types of events exist. The trigger must be able to achieve high acceptances combined with good beamgas rejection independent of the details of the final event shape. To this end, it is useful to use different generators to examine the effects of theoretical uncertainties on the trigger efficiency. An important question also concerns the effect that gluon bremsstrahlung will have on measurements in the detector.

Although DIS events are a major aspect of HERA physics, it is necessary to ensure that other important reactions are not removed at the FLT: such a reaction is the generation of $b\bar{b}$ and $c\bar{c}$ pairs by boson-gluon fusion (BGF) at low Q^2 and low x (see section section 1.2.3.1).

The standard ZEUS Monte Carlo for boson-gluon fusion is HFLGEN 1.3 based on the AROMA generator[82]. Parton showers, string fragmentation and decays are carried out by JETSET[83]. A second generator HARHEA, working within the framework of the HERWIG 5.0 Monte Carlo, also produces BGF events[84–86]. HARHEA differs from HFLGEN in using a cluster hadronization model and including gluon radiation from the initial state quarks.

A HERWIG ASCII interface was written for ZEUSGeant such that the data could be read by ZGANA. This enabled direct comparison of measured parameters in the CTDFLT and the FTDFLT.

8.2 Simulation

One thousand NC $c\bar{c}$ and $b\bar{b}$ events were generated from each of the two heavy flavour generators. Also four thousand beamgas events distributed homogeneously along the beamline from $z = -19\mathrm{m}$ to $z = +1\mathrm{m}$ were produced using the FRITIOF generator (version 1.5).

An initial comparison of the two generators was achieved by using a parameterization of the CTD and calorimeter FLTs. This aims to provide a simple understanding of the likely response of the whole FLT to a set of events. Its philosophy is based on energy deposition and charged tracks. If tracks are found from the vertex, then only loose energy constraints are applied. On the other hand, if no tracks are found then substantial energy deposition (at high angles) is required.

In fact, if no track pointing to the vertex was found in the CTD, an event was accepted if the calorimeter registered more than 5 GeV/c in transverse momentum; if a vertex track was detected, an event was accepted if the transverse momentum was greater than 12 GeV. section 4.3.1.1 explains how these quantities are measured by the CALFLT. Finally, the events were passed through the standalone CTDFLT and FTDFLT simulations and the RBOX simulation to examine the combined tracking response.

8.3 Results

Table 8.1 shows the percentage of events passing the parameterization of the FLT for the four types of events. There is a small difference in the two BGF generators for $c\bar{c}$ events but a major difference is seen for $b\bar{b}$ events. In both cases, it is much easier to trigger on the bottom pair events.

Table 8.2 shows the percentage of $c\bar{c}$ events falling into each of the tracking trigger classes and table 8.3 shows the same figures for $b\bar{b}$ events. These figures may be compared with those for beamgas leakage, shown in table 6.7. As before, for the CTD

standalone mode class 3 events will probably be accepted along with class 2 events so these figures must be summed to produce a final figure.

Event	Efficiency
HFLGEN $c\bar{c}$	0.380 ± 0.015
HERWIG $c\bar{c}$	0.328 ± 0.015
HFLGEN $b\bar{b}$	0.645 ± 0.015
HERWIG $b\bar{b}$	0.825 ± 0.012
Beamgas	0.072 ± 0.006

Table 8.1: Percentage of events accepted by the simple parameterization of the tracking and calorimeter first level trigger.

Event class	HFLGEN	HERWIG
CTD 3 (weak accept)	0.154 ± 0.011	0.140 ± 0.011
CTD 2 (accept)	0.722 ± 0.014	0.730 ± 0.014
CTD 1 (reject)	0.024 ± 0.005	0.025 ± 0.005
CTD 0 (no decision)	0.100 ± 0.009	0.105 ± 0.010
FTD 2 (accept)	0.829 ± 0.012	0.742 ± 0.014
FTD 1 (reject)	0.115 ± 0.010	0.153 ± 0.011
FTD 0 (no decision)	0.056 ± 0.007	0.105 ± 0.010
RBOX 2 (accept)	0.900 ± 0.010	0.900 ± 0.009
RBOX 1 (reject)	0.052 ± 0.007	0.048 ± 0.007
RBOX 0 (no decision)	0.048 ± 0.007	0.052 ± 0.007

Table 8.2: FLT classifications for the full FLT simulations for $c\bar{c}$ events.

Event class	HFLGEN	HERWIG
CTD 3 (weak accept)	0.083 ± 0.009	0.071 ± 0.008
CTD 2 (accept)	0.873 ± 0.011	0.895 ± 0.010
CTD 1 (reject)	0.020 ± 0.004	0.012 ± 0.003
CTD 0 (no decision)	0.024 ± 0.005	0.022 ± 0.005
FTD 2 (accept)	0.880 ± 0.010	0.861 ± 0.011
FTD 1 (reject)	0.110 ± 0.010	0.119 ± 0.010
FTD 0 (no decision)	0.010 ± 0.003	0.020 ± 0.004
RBOX 2 (accept)	0.978 ± 0.005	0.979 ± 0.005
RBOX 1 (reject)	0.018 ± 0.004	0.014 ± 0.004
RBOX 0 (no decision)	0.004 ± 0.002	0.007 ± 0.003

Table 8.3: FLT classifications for the full FLT simulations for $b\bar{b}$ events.

8.4 Discussion

The parameterization of the GFLT is dependent on track multiplicity and transverse energy deposition. The results obtained for GFLT efficiency are thus entirely explained by figure 8.2 and figure 8.3 which show that high acceptance is related to both high mean track multiplicity and high mean transverse energy. This may be clearly illustrated by plotting the means of the figures against the efficiencies. This is done in figure 8.1.

For comparison, figure 8.4 and figure 8.5 show the distribution of transverse energy and charged multiplicity for beamgas events.

In the tracking detectors, a vertex decision is made in the triggers using essentially tracks with a transverse momentum $> 0.5\mathrm{GeV/c}$. The tracking chamber triggers use the ratio of tracks from the vertex to all tracks. This ratio is therefore affected by changes in track multiplicity and transverse momentum.

The distributions in polar angle explain the event classes found. figure 8.6 shows the polar angle of Geant tracks (tracks with energy of less than 1 GeV were omitted).

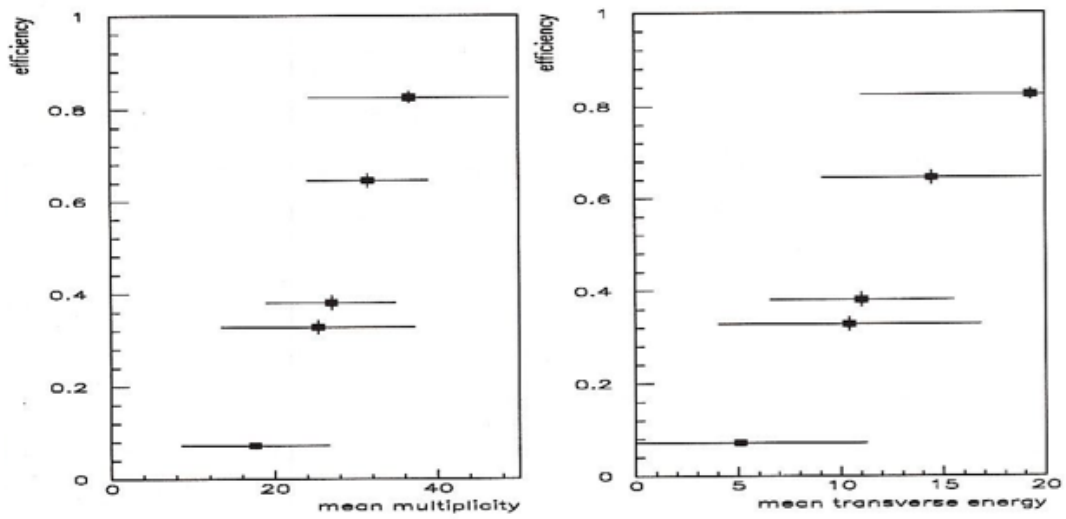

Figure 8.1: Effect of multiplicity and transverse energy on acceptance.

It can be seen that across the broad angular range, both generators are in good agreement with both giving higher multiplicities for $b\bar{b}$ events than for $c\bar{c}$ events. This explains the CTDFLT classes found, which showed both generators giving similar acceptances which were higher in the case of $b\bar{b}$ events. But in the FTDFLT, ir can be seen that there is a significant deterioration in efficiency in HERWIG $c\bar{c}$ events which is not seen in $b\bar{b}$ events. In order to examine this more closely, figure 8.6 also shows the same plots magnified to show only the angular region covered by the FTD, $0.195\,\mathrm{rad} \rightarrow 0.495\,\mathrm{rad}$. It can clearly be seen that the event classes found are reflective of the observed multiplicites.

8.5 Conclusions

It has been shown that the effects of gluon bremsstrahlung may be neglected for $b\bar{b}$ events but become more significant in the case of $c\bar{c}$. The combined FTD and CTD FLT acceptance is excellent for both $b\bar{b}$ and $c\bar{c}$ events with either generator. Higher multiplicities and higher transverse energy for $b\bar{b}$ events mean that they are more likely to pass the tracking trigger. The performance of the tracking triggers would not need

to be optimized further in a dedicated subtrigger. the simple parameterization of the combined calorimeter and tracking trigger indicates that a simple transverse energy cut by the calorimeter reduces $b\bar{b}$ acceptance by at least 10% but eliminates almost 60% of all $c\bar{c}$ events accepted by the tracking trigger alone. A dedicated subtrigger would need to relax the transverse energy cut and restore beamgas efficiency to reasonable levels by using information from other components such as collimators, the vetowall and also timing data.

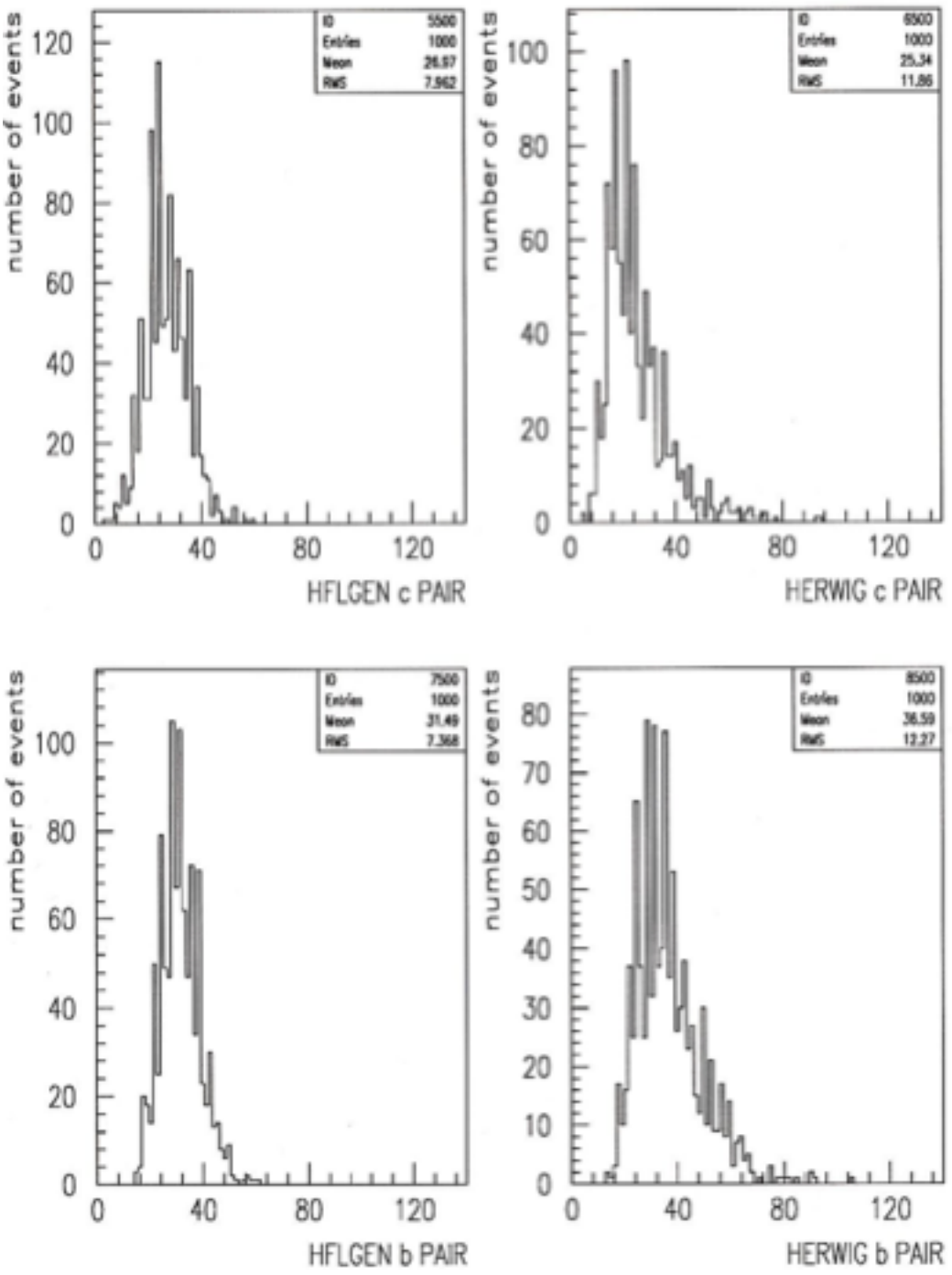

Figure 8.2: Multiplicity of charged tracks per event with a $p_t > 0.5$ GeV/c for heavy flavour events.

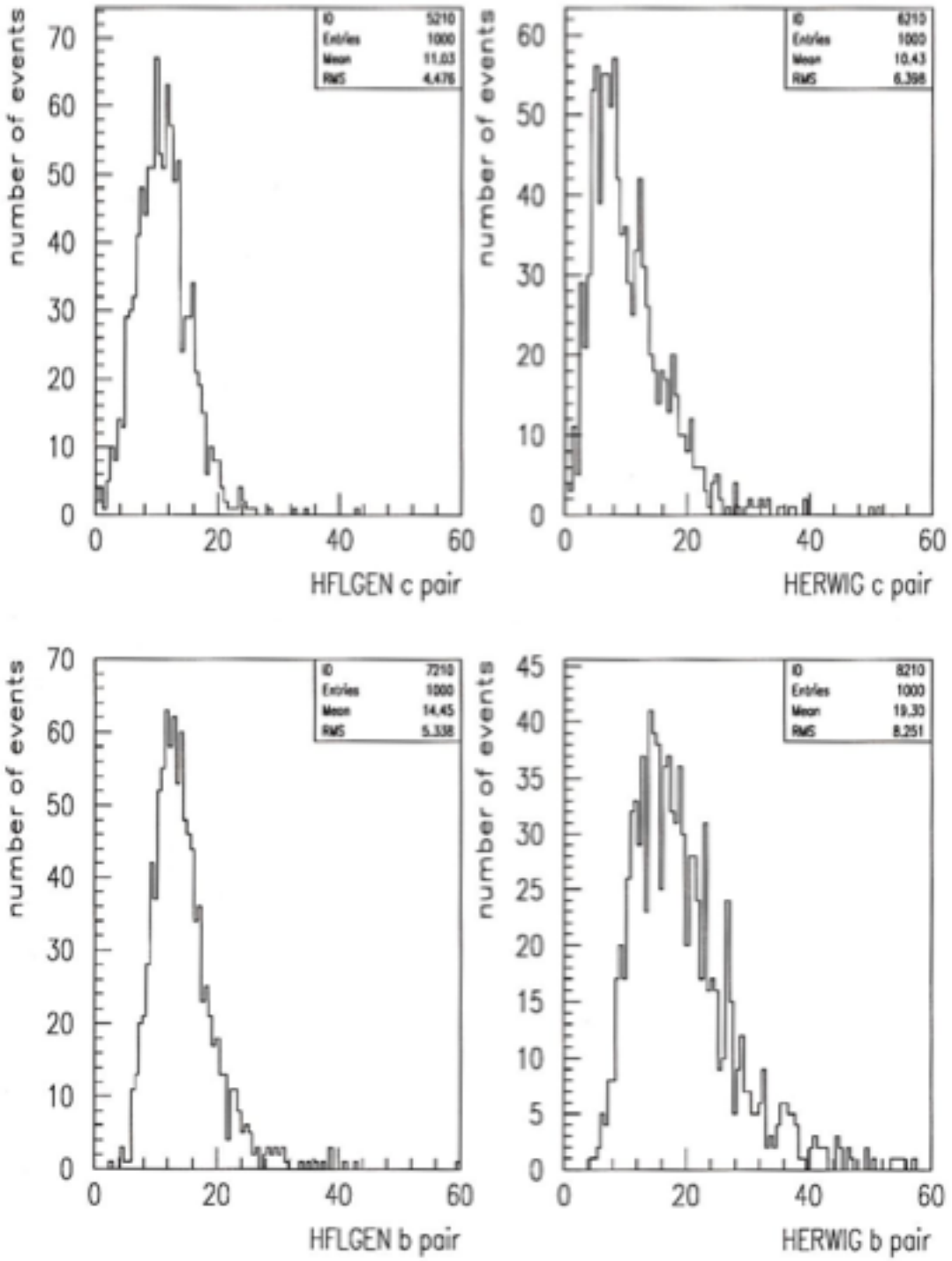

Figure 8.3: Total transverse energy (GeV) per event as measured by the calorimeter for heavy flavour events.

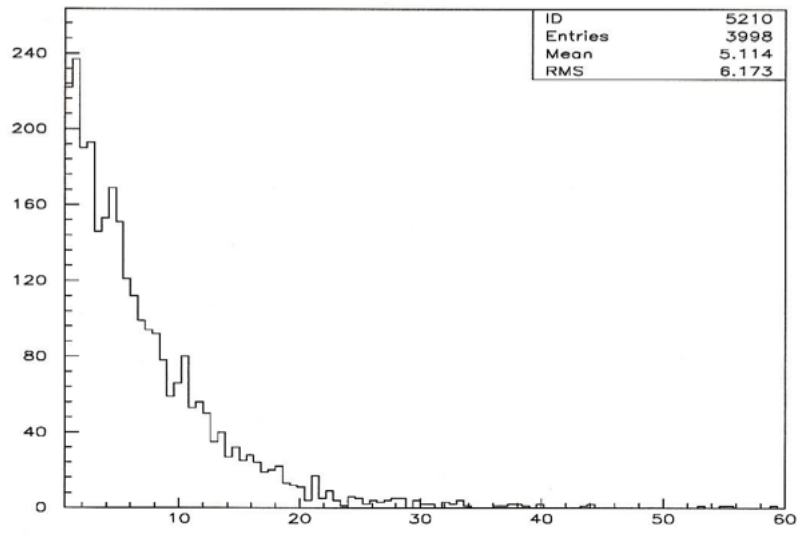

Figure 8.4: Total transverse energy (GeV) per event as measured by the calorimeter for beamgas events.

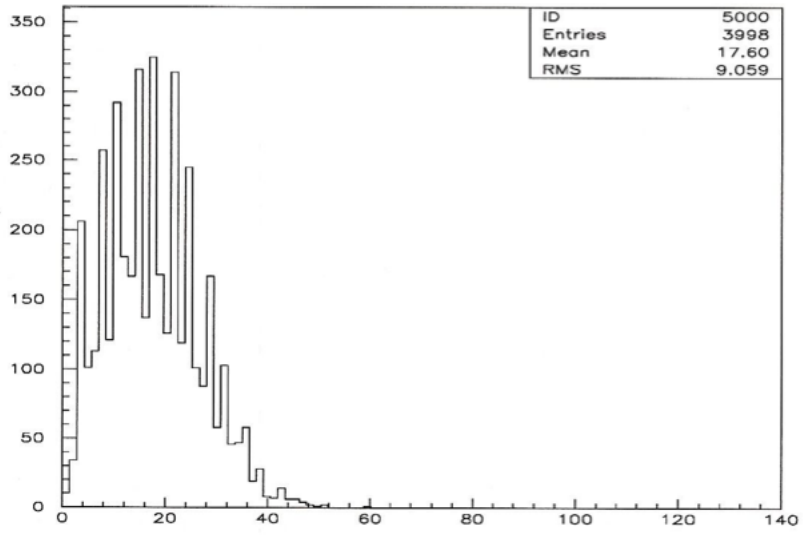

Figure 8.5: Multiplicity of charged tracks per event with a $p_t > 0.5$ GeV/c for beamgas events.

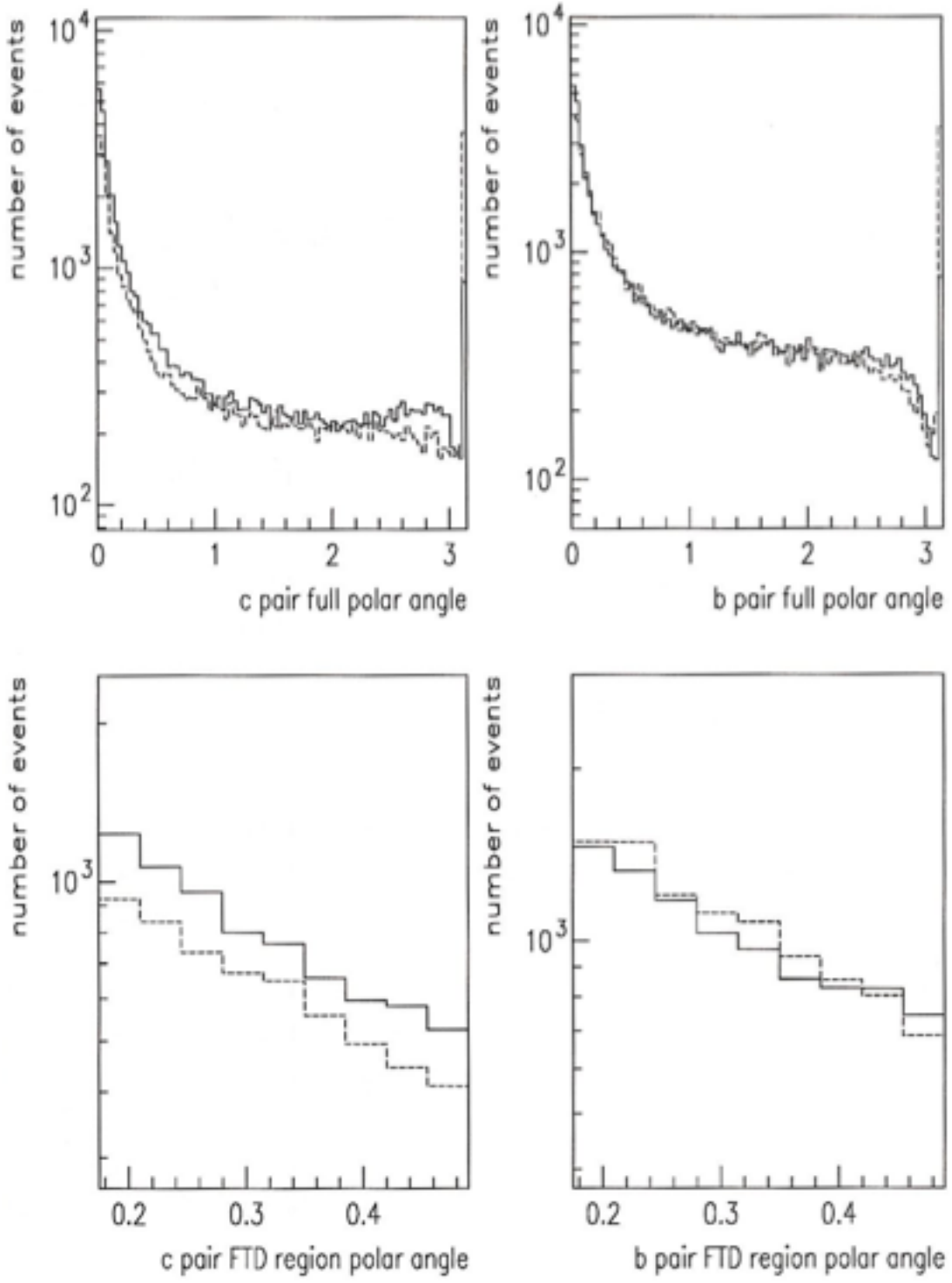

Figure 8.6: Polar angle of Geant tracks for both types of heavy flavour events in full and FTD-only angular ranges. The solid lines are HFLGEN events and the dashed lines are HERWIG events.

Chapter 9

Investigation of J/Ψ Event Acceptance in the FLT

9.1 Introduction

Events containing a J/Ψ can be used at HERA to probe the low-x gluon distribution of the proton[87]. In order to do this it is necessary to know the efficiency of the FLT for these events. In this chapter, trigger efficiencies are measured for the CTDFLT, the FTDFLT and the standard parameterization of the GFLT which was described in section 8.3.

Further, a comparison was made of measured parameters for the J/Ψ sample and a beamgas sample. This enabled a first approximation to a dedicated subtrigger to be suggested.

J/Ψ event tagging methods previously suggested[88] have utilized the luminosity monitor. Here the response of the entire detector is simulated in an effort to identify differences between signal and background.

9.2 Event Generation

The ASCII interface for the HERWIG generator described in section 8.1 was used again here in conjunction with program versions 5.2/5.3. $26,000$ J/Ψ events were generated.

HERWIG allows a choice of five structure functions. These were all investigated and found to produce no discernible differences in the properties of events seen in the detector. For the sake of consistency, option five was used throughout[89].

Investigation then centered on the task of separating the J/Ψ events from the beamgas background.

The beamgas sample produced to allow background studies was generated using the UA5 generator. Forty thousand events were produced with a homogeneous distribution along the beamline from $z = -19\,m$ to $z = +1\,m$.

9.3 Results

9.3.1 Trigger Efficiencies

Table 9.1 shows the proportions of events accepted by the full simulations of the CTDFLT, the FTDFLT and by the parameterization of the GFLT. The results for the RBOX are also shown[1].

The event classes have the meaning used previously in section 5.2.3 so the CTD class two and three must be summed to provide a total acceptance. This means that the CTDFLT accepts 93.1% with beamgas leakage of 7.6%. For a leakage rate of $1\,\mathrm{kHz\,m^{-1}}$ this gives a background of $1528\,\mathrm{Hz}$ from the 20 metre source length.

The beamgas leakage in the FTDFLT corresponds to a rate of $2100\,\mathrm{Hz}$. At the time of the simulation from which results are described here, no FTD class zero was defined in ZGANA: events without diamonds were rejected. In the final system, these events will be described as unclassified. The beamgas leakage in the paramterizations of the GFLT corresponds to a leakage rate of $1138\,\mathrm{Hz}$.

9.3.2 Comparison of Signal and Background

The statistics on the plots relate to the beamgas sample. Where relevant, the mean of the J/Ψ distribution is given on the plot. The figures that are shown relating to

[1] At the time of this work the design of the RBOX was complete. It was felt that using the most modern version of the simulation was important. This was no longer compatible with the RBOX code so only a small event sample was passed through the RBOX code. This is why the statistical errors are larger in this case.

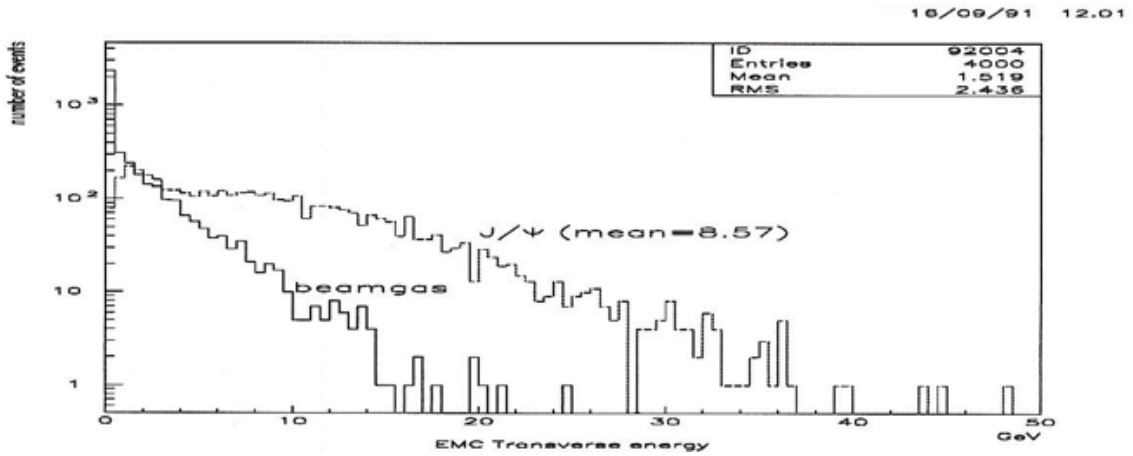

Figure 9.1: Sum of visible transverse energy in the electromagnetic calorimeter.

calorimeter data (figure 9.1 to figure 9.3) show sizable differences between signal and background and therefore are useful in a dedicated subtrigger.

In particular, figure 9.3 explains why the parameterization of the GFLTB rejects some events: there are many signal events with low transverse energy deposition. These will fail the CALFLT cuts.

Figure 9.4 shows that approximately 25% of the beamgas sample has hits in the vetowall. very few signal events register in the vetowall: in a sample of 500 CC events, no hits were observed.

The C5 collimator is located three metres upstream (for the protons) of the interaction region and is designed to reduce the halo of offbeam particles in the beam. It is possible for good events to produce C5 hits by virtue of having tracks in the backward direction but in general hits in the collimator are strongly indicative of a background event. It would clearly be advisable for the trigger to take advantage of this to veto events with C5 hits. Figure 9.5 shows that only a negligible fraction of signal events have C5 collimator hits whereas figure 9.6 shows that substantial discrimination against background is a prospect.

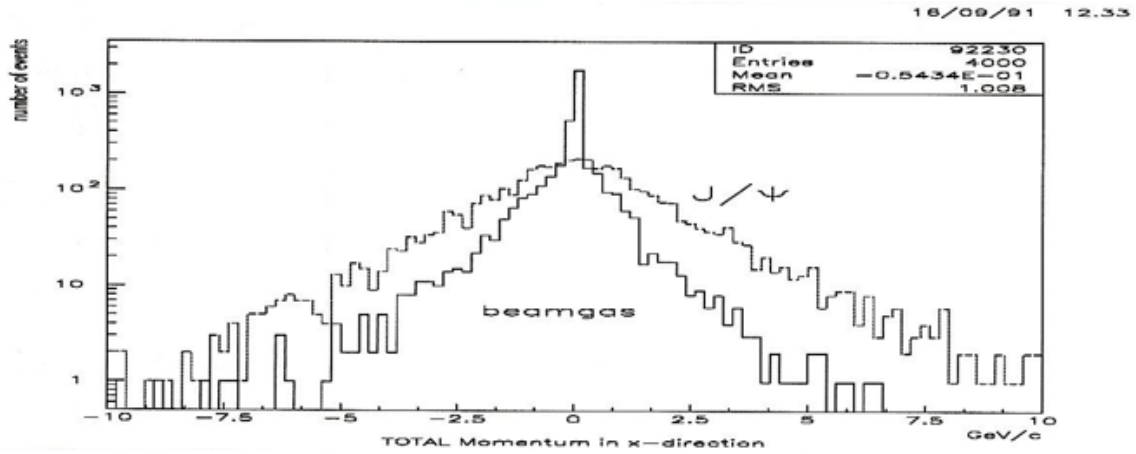

Figure 9.2: Sum of total transverse momentum (x-direction only).

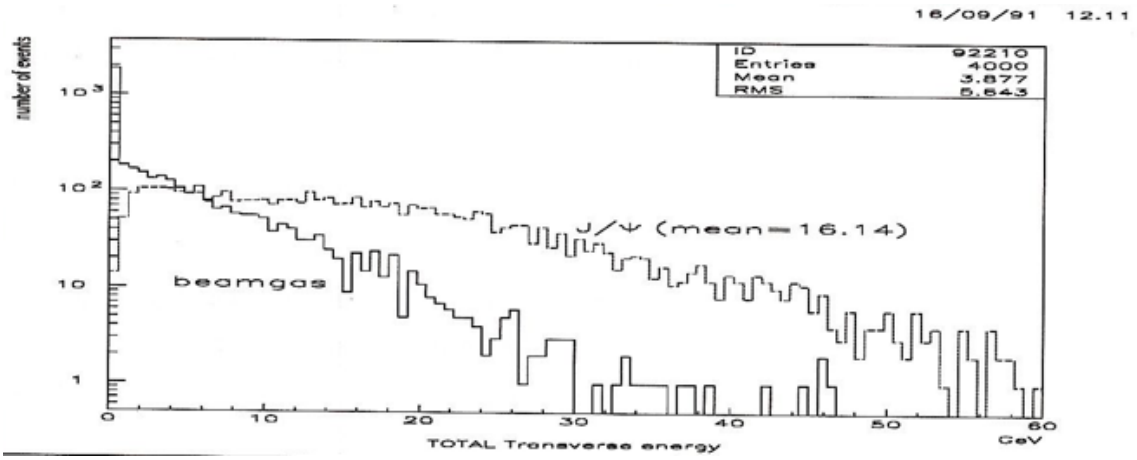

Figure 9.3: Sum of total transverse visible energy.

Event class	HERWIG J/Ψ	Beamgas
RBOX 2 (accept)	0.927 ± 0.008	0.129 ± 0.007
RBOX 1 (reject)	0.063 ± 0.008	0.325 ± 0.010
RBOX 0 (no decision)	0.010 ± 0.003	0.546 ± 0.011
CTD 3 (weak accept)	0.1812 ± 0.0025	0.0310 ± 0.0009
CTD 2 (accept)	0.7495 ± 0.0026	0.0454 ± 0.0011
CTD 1 (reject)	0.0214 ± 0.0010	0.1653 ± 0.0020
CTD 0 (no decision)	0.0480 ± 0.0014	0.7582 ± 0.0023
FTD 2 (accept)	0.5809 ± 0.0036	0.1050 ± 0.0018
FTD 1 (reject)	0.4191 ± 0.0036	0.8950 ± 0.0018
GFLT Parameterization Accept	0.6124 ± 0.0030	0.0569 ± 0.0012

Table 9.1: Event classifications from ZGANA.

9.4 Discussion

Table 9.1 shows that excellent acceptance is obtained by the tracking trigger. In addition, as previously described in section 5.1, the RBOX will combine data from the FTD and the CTD and xo these figures may be expected to improve.

However, the table also shows that further optimization is advisable in the GFLT: some ways to produce a dedicated subtrigger were seen to be plausible from considering the figures, many of which show substantial discrimination between signal and background. To investigate the utility of this as a first approximation to a dedicated subtrigger was devised.It is important to emphasize that no optimization has been done on the trigger parameters: the cut values could be tuned and other subdetectors included.

The subtrigger was developed from a simple philosophy. Calorimeter triggers were set so that they were 'free': *i.e.* plots of measured values were studied to find cut values that would produce no beamgas leakage but still provide some benefit in terms of J/Ψ acceptance.Then if there were clear grounds to reject the event this course

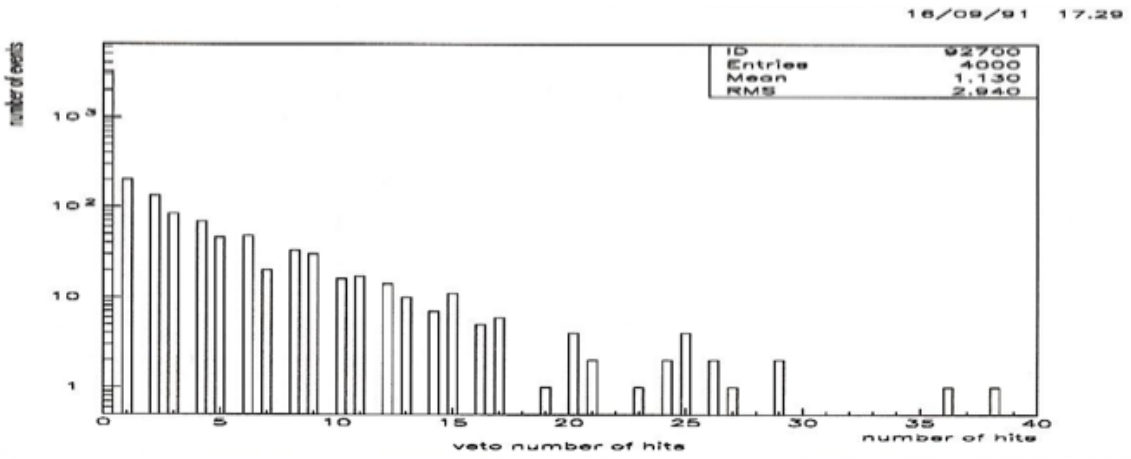

Figure 9.4: Vetowall hits.

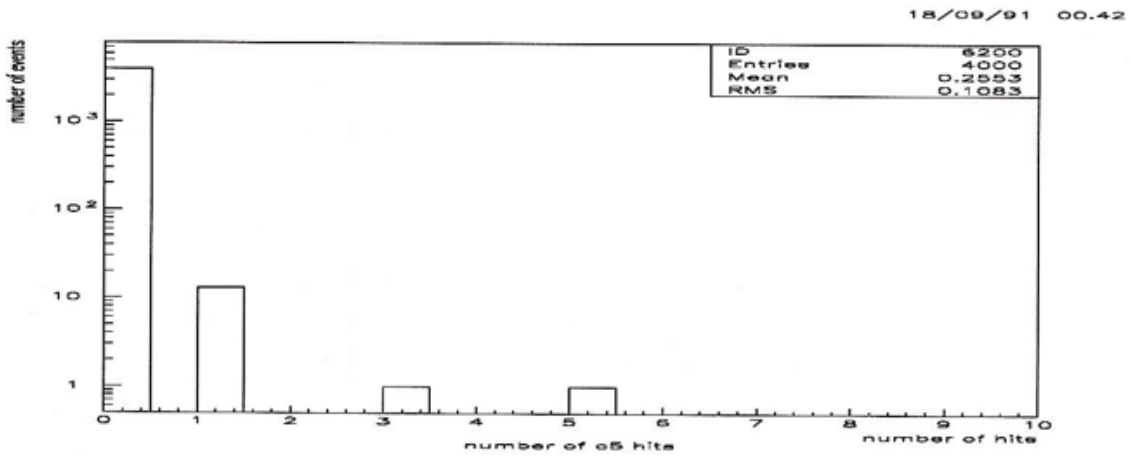

Figure 9.5: Number of hits in C5 collimator for J/Ψ events.

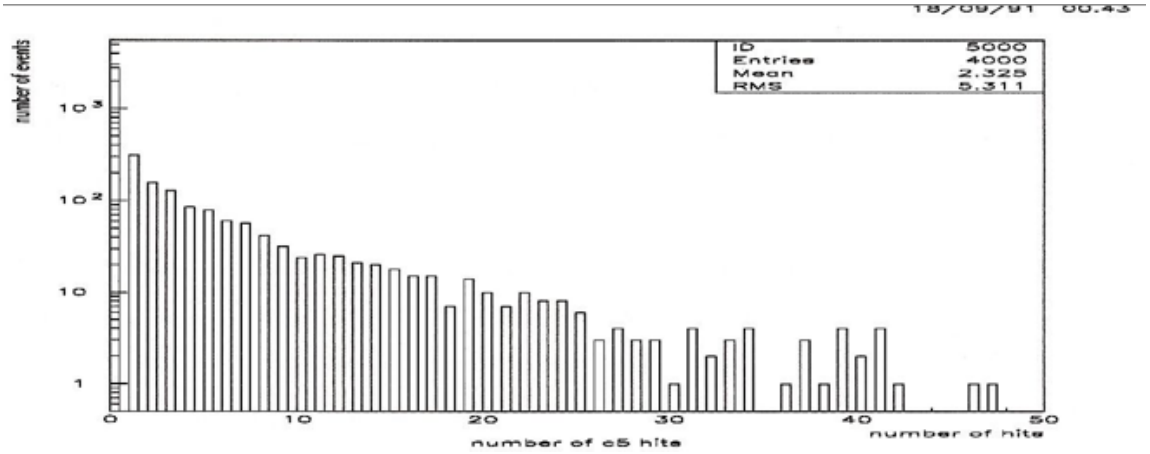

Figure 9.6: Number of hits in C5 collimator for beamgas events.

was taken. Finally the tracking detector triggers were applied to those events still unclassified.

The full details of this trigger are shown in figure 9.7 and the results obtained in table 9.2. It can be seen that the efficiency is comparable to that of the CTDFLT but with improved beamgas leakage figures. The leakage rate implied here is $954\ \mathrm{Hz}$. It should be noted that it is not trivial to improve on the CTDFLT because its performance is already good.

Event class	HERWIG J/Ψ	Beamgas
Subtrigger 2 (accept)	0.9269 ± 0.0025	0.0477 ± 0.0014
Subtrigger 1 (reject)	0.0270 ± 0.0015	0.4889 ± 0.0034
Subtrigger 0 (no decision)	0.0461 ± 0.0020	0.4635 ± 0.0034

Table 9.2: Event classifications for the dedicated subtrigger.

Previous work[90] on J/Ψ events in the FLT achieved an efficiency of 66% with beamgas rates below the acceptable limit. That particular trigger is a complex entity utilizing many subdetector components; moreover, it has been optimized. Operating here would permit cross-checking of efficiencies and result in complementary datasets for J/Ψ physics.

A characteristic of J/Ψ events is the presence of leptons with high transverse momentum in the opposite direction to the quark jet, as described in section 1.2.3.2. It should in general be possible to find these tracks in the CTD or the RTD and a more complex trigger, perhaps at higher levels, could search for these by correlating with the CAL or muon detectors.

9.5 Conclusions

The tracking detector FLT will provide excellent efficiency for J/Ψ events since good performance has been obtained with the CTD and RBOX. reasonable performance may be expected from the GFLT. An optimized subtrigger along the lines suggested here would provide very good efficiency for J/Ψ events.

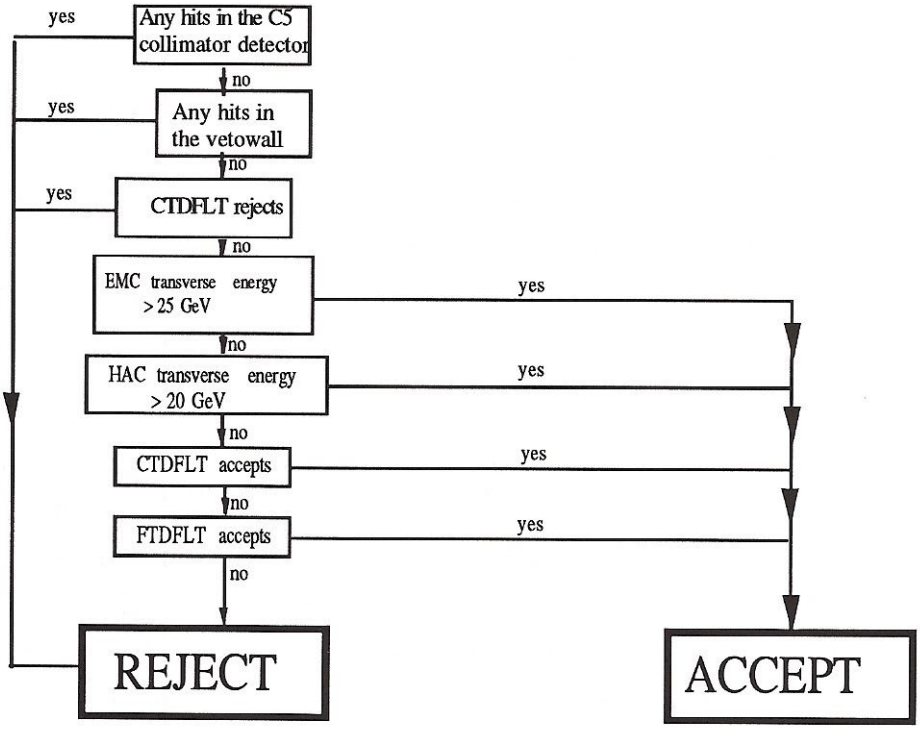

Figure 9.7: Subtrigger decision flowchart.

Chapter 10
Conclusions

The performance of the ZEUS FLT has been investigated for a range of physics of interest, with special regard to the use of data from the tracking detectors.The motivation throughout this work has been to investigate the means by which signal events may be efficiently be selected by the trigger while at the same time holding leakage of beamgas events through the trigger to a minimum. It has been shown that the RBOX will be able to successfully combine data from the FTD and the CTD in such a way as to further this aim despite the differing geometries of these two detectors.

The most important area of physics at HERA is the study of the proton structure function via the analysis of DIS NC and CC processes. An efficient trigger performance for these events is therefore essential. For this reason, the performance of the RBOX has been optimized with respect to them. The performance of the CTD alone for these events has been shown to be good which meant that it was difficult to further improve the situation. Nevertheless, it has been shown that the RBOX will be able to reduce the loss of CC events by a factor of two within the same beamgas leakage constraints as placed on the CTD. This should greatly enhance the quality of measurements made.

While the performance of the RBOX has been shown to be good for DIS events, it is important not to lose sight of other areas of physics interest. With this in mind, other processes have been simulated with a view to examining performance in more broad terms.

In particular, an investigation of heavy flavour pairs both with and without the influence of initial state gluon bremsstrahlung has been made. this has shown that transverse energy and charged multiplicity are the deciding factors which control the efficiency with which a type of event will be accepted. Also it has been shown that the effects of gluon bremmstrahlung may lead to significant changes in event characteristics for charmed pair events. Most importantly, it is now known that the

RBOX will provide a good efficiency for heavy flavour events without the necessity to reoptimize the trigger parameters as designed for DIS.

Further, the efficiency of the RBOX for J/Ψ events has been shown to be good. As was mentioned in the introductory chapter, these events will have a scattered electron at a very low angle. These two facts raise the prospect of using the electron calorimeter of the luminosity monitor to make precise measurements of the scattered electron which in turn will permit ZEUS to probe the gluon distribution in a kinematic domain which is completely inaccessible to other machines.

Accurate knowledge of a trigger efficiency is as important as boosting that efficiency. It has been shown here that the full kinematics of a CC event need not be considered when measuring the kinematic dependence of CTDFLT efficiency. This has allowed a picture to be constructed of the likely variation of efficiency which is comprehensive in terms of range. Also, much greater precision has been obtained than would be possible within available computer resources using another method.

References

[1] A J G Hey I J R Aitchison. Gauge theories in particle physics. *IOP publishing ISBN 0-85274-328-9*, 1989. 1

[2] S L Glashow. Towards a unified theory: threads in a tapestry. *Rev. Mod. Phys. 52 539*, 1980. 5

[3] A Salam. Gauge unification of fundamental forces. *Rev. Mod. Phys. 52 525*, 1980. 5

[4] S Weinberg. Conceptual foundations of the unified theory of weak and electromagnetic interactions. *Rev. Mod. Phys. 52 515*, 1980. 5

[5] P W Higgs. Broken symmetries and the amsses of gauge bosons. *Phys. Rev. Lett. 13 508*, 1964. 6

[6] I S Hughes. Elementary particles. *Cambridge University Press ISBN 0-521-27835-x*, 1985.

[7] G Ingleman $et\ al.$. Deep inelastic physics and simulation. *Proc. HERA workshop Vol. 1, p3*, 1987. 9

[8] G Wolf. Hera: Physics, machine and experiments. *Lectures given at Advanced Study Inst. on Techniques and Concepts of High Energy Physics, St. Croix Inst. (1986) 375*, 1986. 12, 14

[9] D Jones E L Berger. Inelastic photoproduction of j/ψ and γ by gluons. *Phys. Rev. D 23 1521*, 1981. 16

[10] J J Aubert. Measurement of j/ψ production in 280 gev/c μ^+ iron interactions. *Phys. Lett. B 89 267*, 1980. 16

[11] R Baldini Celio *et al.* Observation of the reactions $e^+e^- \rightarrow \pi^+\pi^-\gamma$, $\mu^+\mu^-\gamma$. a test of weizsacker-williams approximation for virtual electrons. *Lett. Nuovo Cim. 27 283-288*, 1980. 16

[12] W J Stirling A D Martin, C-K Ng. Inelastic leptoproduction of j/ψ as a probe of the small-x behaviour of the gluon structure function. *Phys. Lett. B 191 200-204*, 1987. 17

[13] E Reya M Gluck, E Hoffmann. Scaling violations and the gluon distribtuion of the nucleon. 17

[14] R J Cashmore *et al.* Exotic phenomena in high energy ep collisions. *Phys. Rept. 122 C 275*, 1986. 17

[15] N Harnew *et al.* Experimental signatures for leptoquark and leptogluon production at hera. *Proc. of the HERA Workshop Vol. 2, p829*, 1987. 17

[16] ZEUS Collaboration. The zeus detector: Status report. 1989. 26

[17] K Long *et al*. Zeus ctd parameters issue five. *Revised ZEUS Note 89-023*, 1989. 30

[18] F F Wilson. The design and optimisation of the zeus central tracking detector. *Ph.D. Thesis, University of Bristol*, 1989. 32

[19] Motorola Ltd. Dsp56000/56001 digital signal processor user's manual. 32

[20] N Harnew *et al.* Vertex triggering using time difference methods in the zeus central tracking detector. *Nucl. Instrum. Methods A289 290-296*, 1989. 33

[21] C B Brookes *et al.* Development of the zeus central tracking detector. *Nucl. Instrum. Methods A283 477*, 1989. 33

[22] V Commichau *et al.* A transition radiation detector for pion identification in the $100\mathrm{GeV/c}$ region. *Nucl. Instrum. Methods 176 325-331*, 1980. 36

[23] T Kinnel *et al.* Simulation of the zeus calorimeter first level trigger. *ZEUS Note 90-056*, 1990. 39

[24] A Dake *et al.* Pictures of events surviving the first level trigger. *ZEUS Note 90-033*, 1990. 41

[25] G Anzivino *et al.* First level trigger for elastically scattered protons. *ZEUS Note 90-029*, 1990. 41

[26] H Uijterwaal S de Jong. Zeus first level trigger rate estimates for beamga using canonical discriminant analysis. *ZEUS Note 89-070*, 1989. 41

[27] W H Smith *et al.* Global first level trigger timing. *ZEUS Note 90-011*, 1990. 41

[28] T Hasegawa *et al.* Re-estimation of flt rate with calorimeter and ctd information. *ZEUS Note 90-046*, 1990. 41

[29] K Tokushuku. Lists of compound trigge-1 data. *ZEUS Note 89-029*, 1989. 41

[30] K Tokushuku. Gflt design document i. *ZEUS Note 88-098*, 1988. 41

[31] B Foster G P Heath. A proposal for zeus first level trigger timings. *ZEUS Note 87-051*, 1987. 41

[32] G P Heath. Dead time due to trigger procesing in a daq system with multiple event buffering. *Nucl. Istrum. Methods A278 431-435*, 1989. 41

[33] W H Smith *et al.* Zeus calorimeter first level trigger. *ZEUS Note 89-085*, 1989. 41

[34] W H Smith W Sippach. Status of the calorimeter trigger for zeus. *ZEUS Note 87-021*, 1987. 41

[35] S K Park R Seidlein C J Rush, B Bylsma. The fast clear system for zeus trigger. *ZEUS Note 89-072*, 1989. 46

[36] B Bylsma *et al.* Monte carlo studeis of the level 2 fast calorimeter trigger. *ZEUS Note 89-087*, 1989. 46

[37] W H Smith *et al.* The zeus trigger system. *ZEUS Note 89-084*, 1989. 47

[38] Lecce Bologna, Frascati. Triggering on forward muons in zeus. *ZEUS Note 87-060*, 1987. 47

[39] M Adamus *et al.* Veto wall readout and trigger system. *ZEUS Note 87-060*. 48

[40] B Machowski A Dwurazny. Luminosity monitor and small angle electron trigger daq system. *ZEUS Note 88-014*, 1988. 48

[41] H Uijterwaal V O'Dell. Status of the gsltb. *ZEUS Note 90-045*. 51

[42] H Uijterwaal *et al.* Layout of the gsltb. *ZEUS Note 89-073*. 51

[43] H Uijterwaal *et al.* Gslt- the zeus global second level trigger. *ZEUS Note 89-062*, 1989. 51

[44] R C E Devenish *et al.* The zeus central tracking chamber second level trigger. *14th Int. Symp. on Lepton and Photon Interactions, Stanford, CA (OUNP-89-19)*, 1989. 51

[45] R C E Devenish *et al.* Geometry and resolution of the ctd slt. *ZEUS Note 90-078, 90-078c*, 1990. 51

[46] J M Butterworth *et al.* Simulation of the ctd second level trigger. *ZEUS Note 91-072*, 1991. 51

[47] B Foster G P Heath. Ctd second level trigger architecture. *ZEUS Note 87-076*, 1987. 51

[48] D M Gingrich. Ctd second level trigger software design. *ZEUS Note*, 91. 51

[49] J B Lane D M Gingrich, D Shaw. Segment finding in the ctd second level trigger. *ZEUS Oxford 89-001*, 1989. 51

[50] S J P Smith. Tracki finding in the ctd second level trigger. *ZEUS Note 90-060*, 1990. 51

[51] C A R Hoare (ed.). Occam 2 reference manual. *Prentic Hall International Ltd ISBN 0-13-629312-3*, 1988. 51

[52] R C E Devenish *et al.* Zeus central tracking detector second level trigger and readout architectures. *ZEUS Note 90-048*, 1990. 51

[53] H V D Lugt *et al.* Transputer network for calorimeter readout and calorimeter second level trigger. *ZEUS Note 90-014*, 1990. 53

[54] H Uijterwaal S Bentvelsen, I Siccama. First and second level trigger cuts for beamgas suppression. *ZEUS Note 90-116*, 1990. 53

[55] J M Pawlak J Milewski. The design of the bac slt/evb transputer network. *ZEUS Note 90-123*, 1990. 54

[56] F Benard *et al.* Zeus third level trigger monte carlo studies. *ZEUS Note 91-050*, 1991. 55

[57] M Crombie *et al.* Thrid level trigger interfacing. *ZEUS Note 90-116*, 1990. 55

[58] D Bandyopadhyay. Control software for zeus third level trigger system. *ZEUS Note 90-037*, 1990. 55

[59] S Bhadra *et al.* The zeus third level trigger system. *ZEUS Note 89-051*, 1989. 55

[60] R Halsall *et al.* Teh zeus centrsal tracking detector first level trigger processor. *IEEE Transactions on Nuclear Science 37 No. 6*, 1990. 57

[61] G P Heath *et al.* Design of the ctd first level trigger trackfinding processors. *ZEUS Note 89-118*, 1989. 57

[62] Inc Xilinx. The programmable gate array data book. 1988. 58

[63] B Foster G P Heath. Private communication. 66

[64] A Mass J Biltzinger, B Diekmann. The forward tracking detector in the first level trigger of the zeus experiment. *ZEUS Note 91-035*, 1991. 66

[65] A J Martin. Private communication. 69

[66] A Mass. Customer requirements for the ftdflt electronics. *Private communciation*. 69

[67] Y Iga G F Hartner. Zeus trigger monte carlo program status. *ZEUS Note 90-084*, 1990. 74

[68] H Uijterwaal (ed.). Zgana1.x, analysis tool for zeus trigger monte carlo events. *Private Communication*. 74

[69] M Maire A C McPherson P Zanarini R Brun, F Bruyant. Geant 3 user manual. *CERN Data handling division*. 74

[70] T Sjostrand H U Bengtsson, G Ingelman. The lund monte carlo programmes. *Comp. Phys. Comm. 34: 251*, 1985. 74

[71] P Palazzi R Brun, I Ivanchenko. Hbook histogramming, fitting and data presentation package. *CERN Data handling division*. 75

[72] C Vandoni P Zanarini R Brun, O Couet. Paw physics analysis workstation. *CERN Program Libaray Q121*, 1989. 75

[73] J Zoll H J Klein. Patchy reference manual. *CERN Program Library*, 1983. 75

[74] J Zoll. Zebra user guide. *CERN Data handling division Q100*. 75

[75] D Johnson. The ua5 high energy anti-p p simulation program. *Nucl. Phys. B291: 445*, 1987. 77

[76] E Stenlud B Nilsson-Almqvist. Fritiof version 1.6. *Comp. Phys. Comm. 43:387*, 1986. 77

[77] P Palazzi S M Fisher. Using a data model from software design to data analysis. *Proc. Conf. Computing in High Energy Physics*, 19899. 77

[78] Digital Equipment Corporation. Guide to dec/vax module manageent system. 1990. 77

[79] Tofte Frodesen, Skjeggstad. Probability and statistsics in particle physics. *ISBN: 82-00-01906-3*, 1979. 94

[80] H Uijterwaal S de Jong. First level trigger cuts based on the analysis of teh zg311t6 monte carlo data. *ZEUS Note 90-003*, 1990. 97

[81] F F Wilson. Optimisation of the tracking detectors' first level trigger using functional discriminant analysis. *ZEUS Note 91-077*, 1991. 106

[82] G A Schuler. Heavy flavour production at hera. *Nucl. Phys. B 299 21*, 1988. 119

[83] T Sjostrand M Bengtsson. *Comp. Phys. Comm 43 367*, 1987. 119

[84] L Stanco G Abebiendi. A new heavy flavour generator in e-p collisions. *DESY 90-103*, 1990. 119

[85] L Stanco G Abbiendi. Heavy flavour production at hera. simulation with a new monte carlo event generator. *DESY 90-112*, 1990.

[86] B R Webber G Marchesini. Simulation of qcd coherence in heavy quark production and decay. *Nucl. Phys. B330 261*, 1990. 119

[87] 129

[88] S M Tkacyzk *et al.* Inclusive j/ψ production and measurement of teh low-x gluon distribution of the proton. *Proc. of the HERA Workshop VOl. 1 p265*, 1987. 129

[89] J F Owens. An updated set of parton distribution parameterizations. *Phys. Lett. B 266: 126-130*, 1991. 129

[90] J Biltzinger *et al.* First level trigger concept including low-et physics at zeus. *ZEUS Note 91-051*, 1991. 135